Solid Source Metal-Organic Molecular Beam Epitaxy Toward All-Epitaxial Ferroelectric Capacitors

A DISSERTATION

SUBMITTED TO THE FACULTY OF THE GRADUATE SCHOOL

THE UNIVERSITY OF MINNESOTA

BY

William Nunn

IN PARTIAL FULFILLMENT OF THE REQUIREMENTS

FOR THE DEGREE OF

DOCOTR OF PHILOSOPHY

Advisor: Bharat Jalan

July 2021

Acknowledgements

My journey throughout my PhD studies and all the work done within this thesis would not have been made possible without the help and support of many individuals. I joined the Chemical Engineering & Materials Science department at the University of Minnesota in 2015 and was fortunate enough to join Professor Bharat Jalan's research group, even considering my background in chemical engineering with little experience in materials science. It goes without saying that I owe much of my success to Prof. Bharat Jalan and his patience with me as I followed my interests into material science and thin film deposition. He always made himself available and helped guide me throughout the PhD process.

I would like to give special thanks to two older students, Tianqi Wang and Abhinav Prakash, and their considerable efforts in training and helping me learn the research process within our group. Also, a big thank you to Sara Sandlass, a former undergraduate student, who helped with many aspects of this work during her time in the department. Along with them, I would like to thank the rest of the Jalan group members, past and present: Peng Xu, Koustav Ganguly, Jin Yue, Tristan Truttmann, Fengdeng Liu, Shutong Li, Anusha Kamath Manjeshwar, Rashmi Choudhary, Zhifei Yang, Sreejith Nair, John Dewey, Dooyong Lee, Anil Kumar Rajapitamahuni, Hyojin Yoon, Ryan Haislmaier, Laxman R. Thoutam, and Malleswararao Tangi. It has been a pleasure working with all of you and I greatly appreciate the help that was given.

I would also like to express my gratitude to all of my collaborators from other groups, departments, universities, and research institutions whose expertise greatly advanced the merit of this work. A special thanks to Prof. Richard D. James and his students Hanlin Gu, Ashley Bucsek, and Ananya Balakrishna whose close collaboration was a constant source of help throughout my entire PhD. Likewise, I would like to acknowledge all of the staff members at the Characterization Facility and the Minnesota Nano Center for their aid in training and understanding measurements, with a special thanks to Javier Garcia-Barriocanal for all the time spent with X-ray diffraction. I would also like to thank Prof. Juan Maria Garcia Lastra and Arghya Bhowmik for their theoretical calculations on defect complexes. Prof. Eckhard Quandt, Maike Wegner, and Monika Løberg for their help characterizing materials and for their invaluable insights. Prof. Daniel Frisbie and Prof. Steven Koester for allowing me to use their lab facilities. Prof. Venkatraman Gopalan, Shukai Yu, and Bailey Nebgen for the second harmonic generation measurements and discussion of results. And, finally, Prof. James LeBeau and Abinash Kumar as well as Prof. Andre Mkhoyan and Hwanhui Yun, all for their expertise in characterizing materials with transmission electron microscopy.

In the end, I must acknowledge and give my extraordinary thanks to all of my friends and family, especially my father William Nunn and mother Julie Nunn, without whom I would not have made it to where I am today.

Abstract

Great strides have been made in the area of thin film synthesis of complex materials and have led to numerous technological advancements in the various fields related to nanotechnology. Among these materials, perovskite oxides have been identified as an immensely important multi-functional class due to exhibiting a large variety of materials properties, including ferroelectricity. Much progress has been made in the development of ferroelectric perovskite oxides but an important and often overlooked aspect of ferroelectric applications, besides the growth of the ferroelectric itself, is the impact of the contacting metallic electrodes needed for most devices. The choice of electrode material and the control over the quality of the ferroelectric-metal interface can be instrumental in the resulting material and device properties. Unfortunately, model electrode materials mostly contain difficult to work with or "stubborn" elements due to their ultra-low vapor pressures, in evaporation techniques, or low oxidation potentials, in general. Despite the construction of ferroelectric-metal heterostructures having a large impact on device fabrication, deposition of these desirable electrode materials with atomic precision remains challenging.

Molecular beam epitaxy (MBE) has come to the forefront as a leading thin film deposition technique for the growth of these ferroelectric perovskite oxide materials and capacitor heterostructures in a high-quality manner and with some of the best figures of merit. However, deposition involving these stubborn elements has not progressed much

past using conventional electron-beam evaporation approaches to overcome low vapor pressures and highly oxidizing agents like ozone to overcome low oxidation potentials.

To deposit metals and metal oxides in a simpler, more cost-effective, and safer manner, a modification of MBE was developed for the first time here in this work and henceforth referred to as *solid source metal-organic MBE*. The growth of the simple metal Pt, binary oxide RuO_2, and complex perovskite oxide $SrRuO_3$ are shown using metal-organic source temperatures less than 100°C, compared to the greater than 2000°C needed in conventional electron-beam techniques. Furthermore, the metals in these solid metal-organic precursors are in a pre-oxidized state, come bonded with an additional source of oxygen, are air stable, non-toxic, and can be used directly in-vacuum instead of requiring complicated external gas inlets. The growth results from this novel technique introduce it as another advancement in the long history of MBE.

Additionally, with regards to the ferroelectric material, control over complex oxide stoichiometry has remained one of the largest issues within oxide MBE synthesis. Here, a different but rapidly expanding metal-organic-based MBE approach, hybrid MBE, was employed for the growth of ferroelectric and dielectric perovskite oxides with great control over the cation stoichiometry and, therefore, the structure and properties. The prototypical ferroelectric $BaTiO_3$ was studied as well as the consequence of substituting Sn for Ti in the growth of the complete $BaTiO_3 – BaSnO_3$ alloy system for the first time in MBE. Together, these two approaches were utilized and developed for the goal of creating all-epitaxial *in-situ*-grown ferroelectric capacitors.

Table of Contents

List of Figures

List of Tables

Chapter 1

1. Introduction

Devices and heterostructures involving ferroelectric materials have found use in a variety of applications including non-volatile memories,[1] energy storing capacitors,[2-4] and heat to electricity energy conversion devices.[5,6] Much work has been done on the thin growth of these materials, with goals in enhancing piezoelectric and ferroelectric responses, identifying lead-free materials to compete with leading toxic lead-based ones, and understanding the complex role of boundary conditions when creating ferroelectric heterostructures.[2,7-12] In particular, from this last goal, it has become clear that certain materials behave well as metallic electrodes in a conventional ferroelectric metal-insulator-metal structure, while others do not.[13,14] Unfortunately, many of the most widely sought after metallic materials are difficult to work with in deposition techniques, for example Pt and $SrRuO_3$. These materials contain difficult to work with, or "stubborn", elements which have ultra-low vapor pressures and/or low oxidation potentials. While deposition of a variety of materials have advanced in recent years, simple but yet atomically-controlled deposition involving these stubborn elements has been lacking.

In this thesis work, a new atomically precise thin film deposition technique will be introduced for the synthesis of some of these challenging materials. Additionally, existing techniques will be built upon for the growth of the prototypical ferroelectric perovskite oxide $BaTiO_3$ (BTO) as well as to study the enhanced properties achieved when modifying with Sn, all with the goal of fabricating high-quality capacitor structures for applications like energy conversion and storage.

1.1 Perovskite Oxides

Perovskite oxides are a class of material which have been widely studied due to possessing a variety of interesting properties and multiple functionalities, including ferroelectricity, and in many cases within the same material.[15-21] These materials ideally crystallize into a cubic structure of the space group $Pm\bar{3}m$ with the chemical formula ABO_3, where the A-site cation sits at the corner of the cubic lattice and the B-site cation in the body center, surrounded by an oxygen anion octahedron, as can be seen in Figure 1.1.

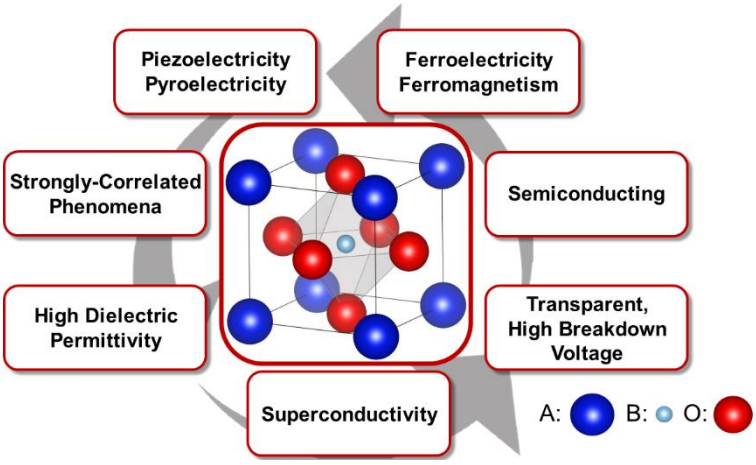

Figure 1.1. Circle of select properties that can arise in the perovskite oxide class of materials. The center shows the prototypical perovskite oxide crystal structure.

Part of the reason so many different properties can be found within this class of materials is their ability to substitute a large majority of the elements in the periodic table at the A- and/or B-site, as shown in Figure 1.2. Through the choice of these A- and B-site cations, properties and materials such as high temperature superconductivity,[22] colossal magnetoresistance,[23] ferroelectricity,[7,24,25] multiferroics,[26] or transparent conducting materials[21] can be achieved. A large focus of this work will be on the structure-property relations that arise through choice of the A- and B-site as well as from other material synthesis conditions.

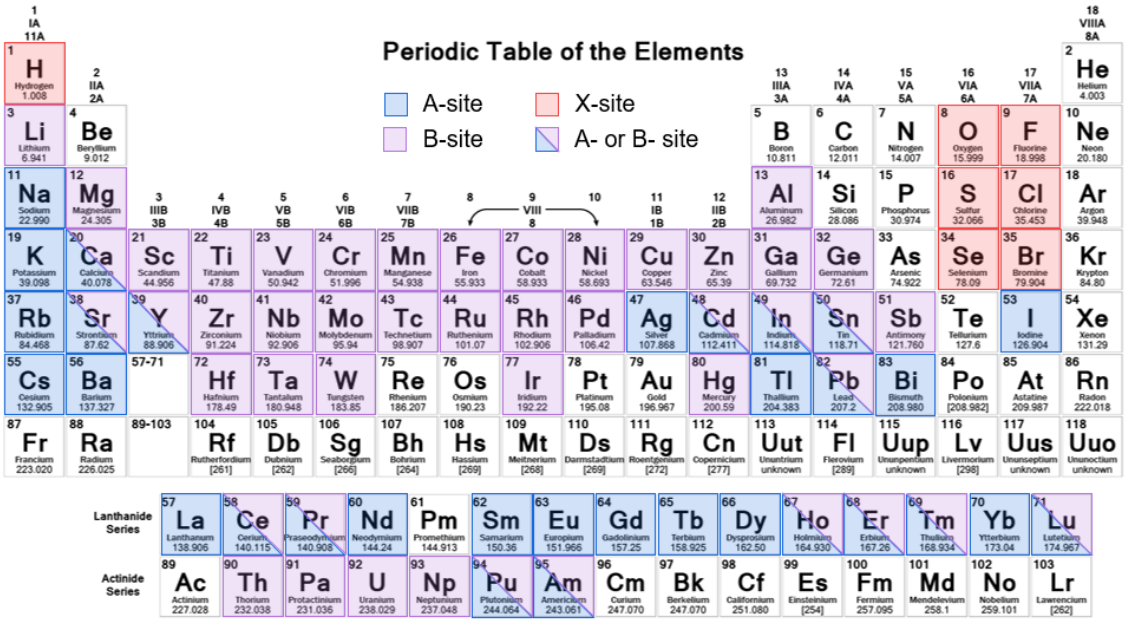

Figure 1.2. Periodic table of elements showing which possible elements have been shown to fit into the perovskite (ABX_3) crystal structure. For perovskite oxides, X = oxygen.

Although the prototypical crystal structure for perovskite oxides is cubic, many do not stabilize into the ideal cubic structure and instead are distorted due to the relative size of the ions as different elements are substituted into the structure. These distortions can

also lead to interesting functionalities and can be described by the Goldschmidt tolerance factor (t),[27] defined as

$$t = \frac{r_A + r_O}{\sqrt{2}(r_B + r_O)} \quad (1.1)$$

where r_A, r_B, and r_O are the ionic radius of the A-site element, B-site element, and oxygen, respectively. The tolerance factor typically will range from 0.8 to 1.1, with the further from t = 1, the further distorted the structure becomes and loss of crystal symmetry and stability can occur.[15] These changes in structure are typically stabilized through oxygen octahedral tilts and/or distortions and can lead to drastic changes in properties.[28]

1.2 Defects

Defects also play a large role in the properties of perovskite oxides and are a commonly overlooked aspect in the structure-property relationship. Material defects come in many different forms: bulk defects like pores, cracks, or flakes, planar defects like grain boundaries, twin boundaries, or domain walls, line defects like dislocations, and point defects like interstitials, vacancies, or substitutional defects. While all are important for device applications, when it comes to thin films, especially single crystalline thin films which will be the focus of this work, point and line defects play the largest role.

For point defects, non-stoichiometric-related defects are most common when synthesizing perovskite oxides. These can be related to the A-site to B-site cation ratio not being one-to-one or the material being off-stoichiometry in terms of the oxygen content. For the former, any of the point defects mentioned can occur when one of the metallic elements is in excess of the other, for example anti-site defects. For the latter, oxygen

vacancy formation is a common occurrence in perovskite oxides if the oxidation conditions are not suitable. Point defects can also occur as defect complexes, where the energy of formation is lower for two or more-point defects to form together, rather than just one. For example, a cation and oxygen vacancy tied together rather than just a cation vacancy. Other point defects such as from extrinsic impurities are also possible and based on the cleanliness of the synthesis approach.

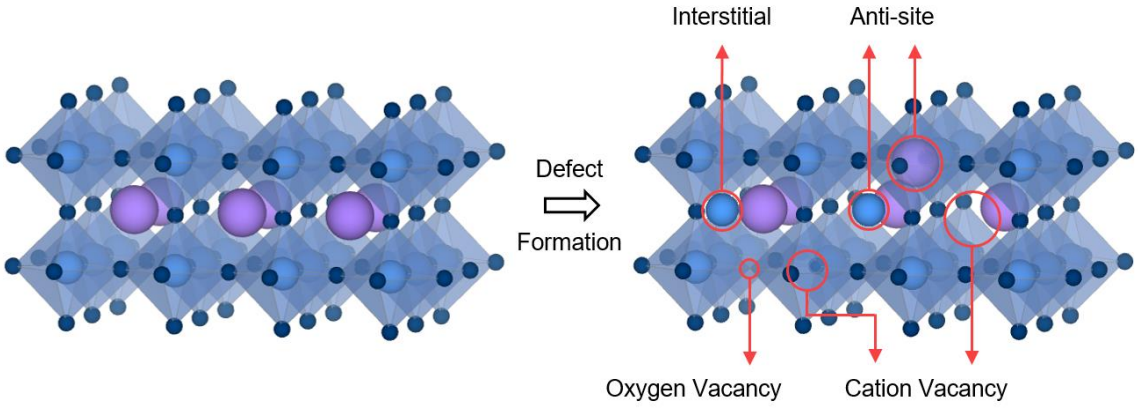

Figure 1.3. Examples of point defects that can form in perovskite oxides. Perfect crystal on the left, defect-incorporated crystal on the right. The crystal will usually incorporate defects through distortions and tilts of the oxygen octahedral, not pictured here.

Dislocations are the most frequent of the line defects, especially in the thin film growth of perovskite oxides. Here, the focus will be on the epitaxial growth of perovskite oxides, where crystal growth occurs and is heavily influenced by the lattice spacing, symmetry, and orientation of the crystalline substrate on which the film is grown. Lattice mismatch is the difference in the lattice parameters of the film and substrate and when present will cause strain, compressive or tensile, to build in the film. Eventually, as the film thickness is increased, it will become more energetically favorable for this strain to “relax”

by forming dislocations. Usually, these are seen as misfit dislocations, where one atom is missing periodically along the film-substrate interface, and threading dislocations, a line defect that extends from the interface into the film.

Defects generally negatively impact material properties. As examples, most defects act as additional scattering centers, decreasing the electron mobility of semiconductors,[21] or, in the case of oxygen vacancies in oxide ferroelectrics, introduce additional carriers causing considerable and undesirable leakage currents.[29,30] However, defects are not always unwanted. Many good examples are present for one of the most well-known perovskite oxides, $SrTiO_3$ (STO). Oxygen vacancies can change the normally insulating STO metallic[31] and even a superconductor,[32] oxygen deficient secondary phases can cause ferromagnetism,[33] and Sr vacancies[34] and anti-site defects can lead to ferroelectricity.[35] The intentional creation of defects like these have led to new fields of study within defect engineering.[36]

1.3 Ferroelectricity

Ferroelectricity and the growth of ferroelectric materials and heterostructures will be the large focus of this thesis work. Ferroelectricity is the property of spontaneous electric polarization in the absence of an electric field. Materials with this property can remain polarized, having a dipole moment in zero electric field, and switch between positive and negative polarization with a large enough applied field. When most materials are polarized, there is a linear relationship between polarization (P) and electric field (E), known as dielectric polarization. This relationship is given by

$$P = \varepsilon_0 \chi_e E, \tag{1.2}$$

where ε_0 is the electric permittivity of free space and χ_e is the electric susceptibility. χ_e can further be defined as $\chi_e = \varepsilon_r - 1$ where ε_r is the relative permittivity or dielectric constant of a material, a commonly reported value for dielectrics. Another class of materials undergo paraelectric polarization and have a nonlinear response to electric field due the relative permittivity having a dependence on the field. Finally, ferroelectric polarization shows a hysteresis in the relationship between polarization and electric field, allowing for switchable spontaneous polarization.

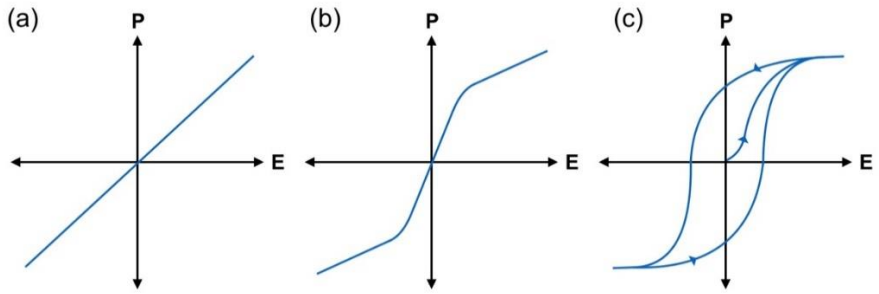

Figure 1.4. Polarization vs electric field for (a) dielectric, (b) paraelectric, and (c) ferroelectric material.

Ferroelectricity is most prevalent in oxides with the perovskite structure.[25] The ideal cubic perovskite structure is centrosymmetric, meaning it has an inversion center as a symmetry element. For perovskites, the property of ferroelectricity can only occur in those with lower-ordered structures, those that are not centrosymmetric, due to displacements of the cations relative to the anions causing a lack of inversion center.

Many perovskite oxides exhibit ferroelectricity, e.g., $PbTiO_3$, $BiFeO_3$, $LiNbO_3$, $KNbO_3$, but the one which will be studied here is perhaps the most well-known and prototypical ferroelectric perovskite oxide, BTO. BTO has room-temperature

ferroelectricity with a Curie temperature (T_c) of about 120°C.[37] At T_c, BTO undergoes a first-order phase transition to a cubic structure accompanied by a large change in polarization. With a tetragonal unit cell at room temperature, bulk BTO has lattice parameters of 3.992 Å and 4.036 Å along what is commonly denoted as the *a*-axis and *c*-axis, respectively.[38]

Some of the applications BTO has been extensively studied for include dielectrics,[39] ferroelectric random-access memory,[1,24] lead-free capacitors,[2] photonic devices,[40] and energy conversion devices.[5,6] In particular, this last application of energy conversion has gained significant recent interest due to the capability of transforming abundant, yet often discarded, low-temperature waste heat into a useful form of electricity. By taking advantage of cycling through the ferroelectric first-order phase transition, and the accompanied large changes in polarization, energy conversion has been achieved.[5,6] However, first, this process has yet to be accomplished in thin films, only shown in bulk ferroelectric crystals. Second, this device is preferred to be constructed using a lead-free ferroelectric, even though lead-based ferroelectrics show the largest ferroelectric responses. Finally, third, although already demonstrated using BTO, modifications of the crystal structure and properties are desired to increase ferroelectric responses close to these lead-based ferroelectrics and to decrease material fatigue created by the thermal cycling.

1.4 Opportunities for Ferroelectric Tuning

Of the leading ferroelectrics, unfortunately, most contain the toxic element lead, as they are based on tuning the $PbTiO_3$ structure,[41] for example as lead zirconate titanate

(PZT)[42,43] and magnesium niobate lead titanate (PMN–PT).[44] Perhaps the most popular ferroelectric material is PZT which has some of the best ferroelectric and piezoelectric properties due, in part, to the presence of morphotropic phase boundaries.[45] Finding lead-free materials which exhibit similar properties to PZT, such as containing these property enhancing morphotropic phase boundaries, has been given considerable attention.[10-12] Materials like, and modified based on, $BaTiO_3$, $BiFeO_3$, $Na_{0.5}Bi_{0.5}TiO_3$, and (K, Na)NbO_3 have been the focus of many studies and have shown promising results.[46-51]

With the flexibility of the perovskite crystal structure, there are many opportunities to tune the structure, and therefore properties, by substituting in different elements at the A- and B-site. While discovered earlier than $PbTiO_3$, BTO, and modified systems based on it, have continued to be looked as replacements to lead-based ferroelectrics. The properties of BTO itself are not as promising, but with substitutions at the A- and B-site, much progress has been made. One of the most studied is the substitution of Sr^{2+} for Ba^{2+} at the A-site. Although showing an increase in the dielectric constant, a decrease in leakage currents, less dielectric loss, and lack of fatigue problems,[52-55] these properties still have not matched the lead-based ferroelectrics in most cases.

At the B-site, new work is being done on the substitution of elements like Sn,[56-58] Zr,[59-61] and Hf,[62-64] for Ti. Of these, the $BaTiO_3$-$BaSnO_3$ alloy system, or $BaTi_{1-x}Sn_xO_3$ (BTSO), has seen considerable interest due to the discovery in ceramics that the dielectric constant can increase by orders of magnitude to ~ 9000 and the longitudinal piezoelectric coefficient (d_{33}) to ~ 425 pC/N around $x = 0.11$.[58,63,65] Further, at this composition, when the temperature is increased to 40°C, these properties are increased even further to ~ 75,000

and 697 pC/N, respectively, due to the presence of a quasi-quadruple point, a state of four-phase coexistence.[58] The phase coexistence at the quasi-quadruple point creates a double morphotropic phase boundary and is thought to enhance these dielectric and piezoelectric properties by allowing for increased polarization rotation and extension.[58] Although much work on this system has been done in ceramics, relatively less has been done in films, which adds even more synthesis challenges.

1.5 Challenges with Ferroelectric Heterostructures

Besides minimizing unwanted defects and trying to tune structures with elemental substitutions, ferroelectrics have other challenges when grown as thin films that are not applicable in many other material systems. These challenges are related to the boundary conditions, the properties of the top and bottom interfaces of the ferroelectric film. Generally, the boundary conditions are split into two categories: mechanical and electrical. As has been discussed, the most common mechanical boundary condition for all epitaxial growth, not just with ferroelectrics, is the lattice mismatch between the film and substrate. Lattice mismatch can create undesirable defects such as misfit and threading dislocations which have been shown to degrade ferroelectric properties by creating depolarization fields around the defects themselves.[66] On the other hand, lattice mismatch can be used as an advantage. For example, the strain imposed on the film resulting from this mismatch, when compressive, has been shown to significantly enhance the polarization and increase the Curie temperature.[67] Compressive strain has even been shown to cause ferroelectricity in materials which are otherwise not ferroelectric.[68] Other mechanical boundary conditions

of concern include crystallographic orientation[69] and surface morphology[70] of the substrate which can greatly affect properties like domain formation.[70-72]

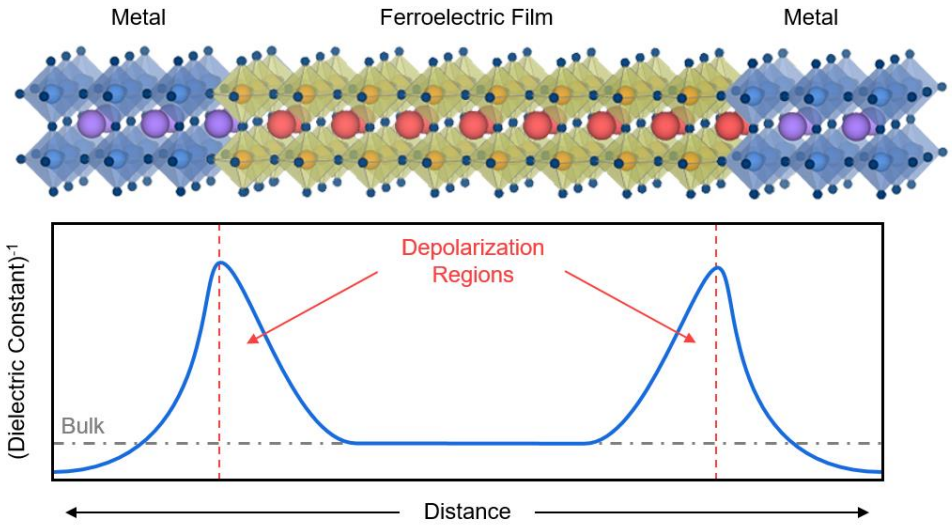

Figure 1.5. Schematic representation of the depolarization regions occurring when a ferroelectric film is grown between two metallic electrodes.[13] Plotted as the inverse of the dielectric constant against the distance across the metal-ferroelectric-metal heterostructure.

Electrical boundary conditions, or the electrostatic properties of the interface, are equally as important and perhaps much more important for ferroelectric materials compared to others. The most common consequence of the electrostatic interfacial characteristics is what is known as a "dead layer", or a region at the interface between a ferroelectric and metal where a loss of polarization or dielectric permittivity occurs.[14] These depolarization regions develop due to an incomplete screening of the electrostatic charge at the interface by the metallic material.[13] The dead layer is an intrinsic property of the interface but can be expanded by defects as a result of the film deposition process. Many efforts have been made to reduce the size of the dead layer such as improved film

synthesis and choice of metal. When creating ferroelectric devices, choosing metallic electrodes which decrease the dead layer effect, like $SrRuO_3$ which has good lattice polarizability or Pt which has a superior electronic screening length, is key. In this work, careful attention will be given to film synthesis and new approaches will be developed for metal electrode deposition to, in part, minimize the effect of these boundary conditions.

Chapter 2

2. Oxide Molecular Beam Epitaxy

Molecular beam epitaxy is an ultra-high vacuum thin film deposition technique which uses the co-deposition of molecular beams of desired elements to form epitaxial films on a substrate surface. After developing a reputation for being able to grow some of the highest quality films with atomic layer control, MBE has been used for the growth of a variety of material systems with a large amount of success.[16,17,20,21,73] As an introduction to the oxide MBE techniques that will be used and developed further here, in this chapter the recent progress made on complex oxides by MBE will be discussed. After reviewing the history of physical vapor deposition and the development of oxide MBE, the inherent advantages of MBE and its various challenges for the growth of high-quality complex oxides will be discussed, many of which will be a focus throughout the rest of this work.

This chapter was adapted from an invited *Journal of Materials Research* review article yet to be published: William Nunn, Tristan K. Truttmann, and Bharat Jalan. Progress in MBE for the growth of complex oxide wide bandgap semiconductors. (2021)

2.1 History of Physical Vapor Deposition

Tracing the history of thin film deposition can give us context of where the field stands to today and where it is postured to go in the near future. Thin film deposition is typically divided into two categories: chemical vapor deposition (CVD), which involves chemical reactions occurring between volatile precursors, and physical vapor deposition (PVD), which involves the physical process of transporting sources between phases for film growth on a substrate. Here, PVD techniques are the focus which, through their progression (Figure 2.1), have cemented themselves as instrumental in the development of complex oxide wide bandgap thin films.

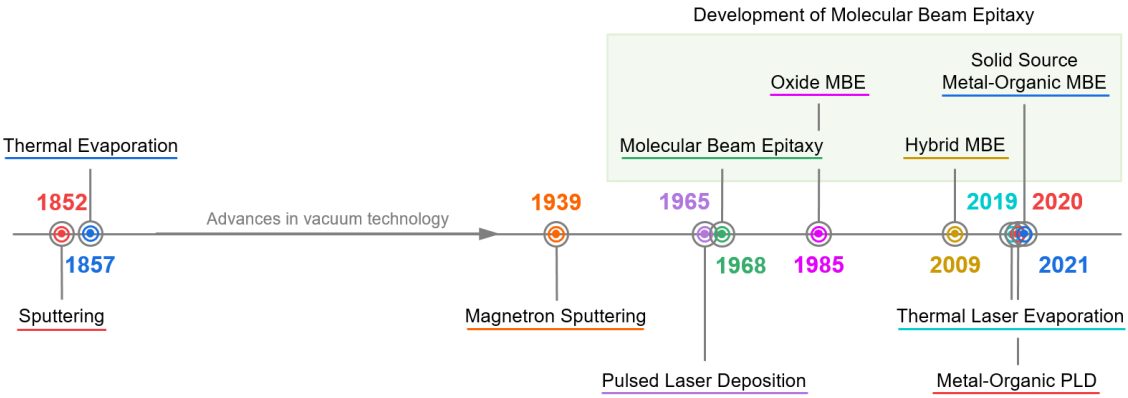

Figure 2.1. Timeline of the introduction of PVD techniques, including some of the modifications that have arisen with a focus on the development of MBE specifically.

Of the main PVD techniques, sputtering, thermal evaporation, MBE, and pulsed laser deposition (PLD), the first two found their inception over a century earlier than the latter two, in the 1850's.[74] The first published report of sputter deposition can be traced back to 1852 by Grove who observed the deposition of a film, primarily iron oxide, on a

silver plated substrate after creating an electrical potential between the substrate and a steel needle in low vacuum.[75] Although the term sputtering would not be coined until years later, these experiments are the first observations of the phenomenon. The process of thermal evaporation would be demonstrated a few years later by Faraday in 1857 who first "exploded" metal wires in a low vacuum, thereby thermally evaporating the sources to form a film.[76] What would follow these early experiments is years of technological advancements, especially related to improving vacuum, that would eventually lead to the more modern approaches that exist today.

Following these advancements, more than one hundred years later in the 1960's, the development of PLD and MBE began. PLD was first shown by Smith and Turner in a report published in 1965 in which they demonstrated, using a pulsed ruby laser, the deposition of a variety of materials, including semiconductors, chalcogenides, and dielectrics.[77] Their early work, although showing some mixed results, laid the foundation for the much more refined technique widely used today. In fact, it would play a key role in the development of high-T_c superconductors in the late 1980s which exploded into a new ground-breaking field of study.[78-81] Finally, MBE, derived from thermal evaporation, found its conception at Bell Labs by a group of scientists including John R. Arthur Jr who would first publish on the use of separate "molecular beams" of gallium and arsenic to form epitaxial GaAs films.[82] Alfred Y. Cho and others would then join him to develop the technique into what is called MBE today.[83,84]

Many advancements within these techniques have since been made including, importantly, magnetron sputtering[85] which has become the most common configuration of

sputtering today. Within MBE[86,87] and PLD[88], modifications have included in many cases metal-organic-based approaches which substitute some metal-organic compounds for conventional metal sources, which is the inspiration for the novel solid source metal-organic MBE approach introduced for the first time in this thesis work.

2.2 Development of Molecular Beam Epitaxy

MBE has played a large role in many materials science and physics discoveries as a result of both the conventional approach and these modifications that have arisen. As shown in Figure 2.2, MBE itself has rich history of scientific advancements since its inception in the late 1960's for the growth of III-V semiconductors like GaAs, as mentioned previously, with adsorption-controlled stoichiometric growth.[82] This control over the stoichiometry and consequently the structure of the films was enough to lead to the first demonstration of modulation doping in 1978,[89] which was previously unattainable due to the lower quality of films and heterostructures produced by other PVD techniques at the time. Within the following three years the discovery of the integer and fractional quantum Hall effect was made as a result of these modulation doping heterostructures, which would be the subjects of the Physics Nobel Prizes in 1985 and 1998.[90] The 1970's and 1980's were then filled with rapid advancement of the MBE technique including for growth of II-VI semiconductors,[91] III-V nitrides,[92] van der Waals epitaxy for 2D materials,[93] and eventually the first report of MBE complex oxide growth, deposition of $LiNbO_3$ in 1985.[94]

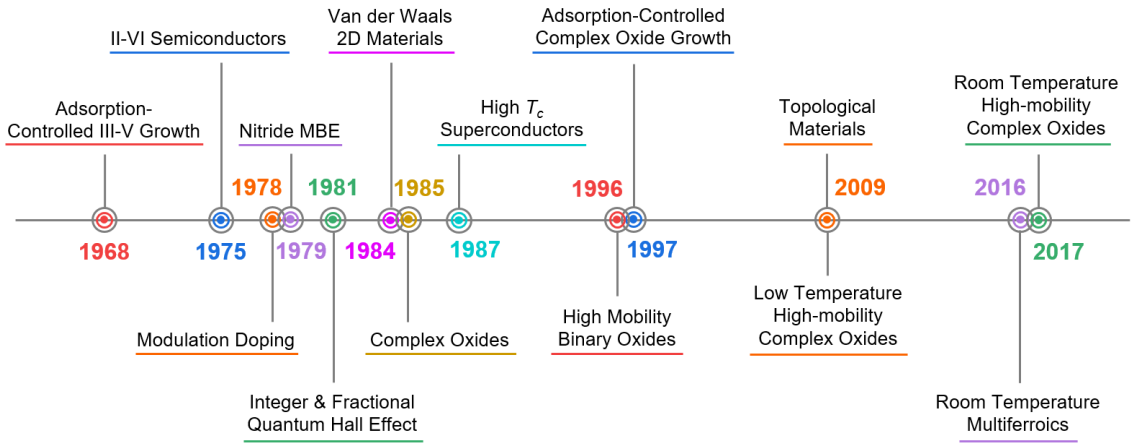

Figure 2.2. Timeline of the development of MBE for a variety of impactful classes of materials and discoveries.

Although the first report of oxide MBE was for $LiNbO_3$, the field really took off following the 1986 discovery of high-T_c superconductivity in cuprates.[79] Many researchers rushed to produce these materials as thin films and achieved incredibly rapid success. Following the first thin film cuprates grown by PLD,[80] the first films were grown by MBE later the same year in 1987.[95,96] However, all these films required annealing in oxygen to show superconductivity. Indeed, the difficult oxidation of Cu to 2+ served as an early test of the limits of oxide MBE. But this challenge was overcome only one year later in 1988 with the development of pure ozone MBE which could produce superconducting films without post annealing,[97] and which was improved in 1990 with silica gel to prevent ozone explosions.[98] In this incredible span of 5 years, the field of oxide MBE went from conception to an accomplished technique attesting to the adaptability of the MBE approach.

Even as more reports of oxide MBE appeared, including the first demonstration of the high mobility binary oxide ZnO,[99-101] the problem of achieving cation stoichiometry in

complex oxides still eluded researchers until the late 1990's when adsorption-controlled growth was first shown in oxide MBE.[102-104] Finally, in recent years, MBE has become prominent in the growth of topological materials like Bi_2Se_3,[105,106] room temperature multiferroics,[107] and low-[86] and room-temperature[108,109] high-mobility oxide semiconductors which have included growth by the metal-organic-based modifications, like hybrid MBE.

2.3 Technique Comparison

Choosing a PVD technique is an exercise in comparing the advantages and disadvantages of each technique to the applications requirements and resources. These advantages and disadvantages are summarized in Table 2.1, including solid source metal-organic MBE. CVD and sputtering have found a lot of success in larger-scale industrial processes due to their simplicity, lower costs, and, especially with sputtering, high scalability. However, it is a different story when it comes to developing new materials on a research level, especially with complex oxides. In this environment where sample quality and material flexibility are valued over scalability, PLD and MBE have become the predominant thin film growth techniques.

Table 2.1. Advantages and disadvantages of conventional PVD techniques as well as two of the metal-organic-based MBE modifications.

Technique	Advantages	Disadvantages
Magnetron Sputtering	High deposition rate and scalability. Able to supply many metals and dielectrics. Ease of use for ultra-low vapor pressure metals compared to evaporation techniques.	Stoichiometry of target is not necessarily transferred to film. High-energy can lead to defect nucleation. Backsputtering of deposited films if not using off-axis.
Pulsed Laser Deposition	Flexibility in laser wavelength and power. Precise growth rate control. Target stoichiometry transfer is capable in many cases. Ease of use. *In-situ* characterization available, e.g., RHEED.	Stoichiometry of target is not necessarily transferred to film. High-energy can lead to defect nucleation.
Conventional Oxide MBE	Excels at limiting defects due to low-energy deposition. Adsorption-controlled stoichiometric growth is possible. Monolayer growth control. *In-situ* characterization available, e.g., RHEED.	Stoichiometry limited by degree of flux control if no growth window. Oxygen stoichiometry and metal oxidation limited by low oxygen background pressure. Oxidation of sources. Low growth rates.
Hybrid MBE	Great control over stoichiometry due to growth windows. No source oxidation of metal-organics. Can supply oxygen and pre-oxidized metal via metal-organic precursors.	High vapor pressure, thermally stable metal-organics required. Need external gas inlet system.
Solid Source Metal-Organic MBE	Able to supply elements having ultra-low vapor pressures with source temperatures < 100°C. Possible to supply “pre-oxidized” elements. No gas inlet needed. No source oxidation of metal-organics. Cheap and safe.	Must use solid, thermally stable metal-organics with intermediate vapor pressures. Cannot fully bake system due to metal-organic source.

A key factor for developing new materials and studying the underlying physics present within them is the defect concentration of the material. While defects can prove useful and have led to numerous studies on defect engineering,[36] unintentional defects tend to impede the ability to study the intrinsic properties, in particular with wide-band gap semiconductors. Here, two deposition parameters that are crucial to understanding defect formation in PVD techniques will be explored: particle kinetic energies and mean free path.

Of all the different deposition parameters, perhaps none is more important to understand defect formation than kinetic energy of the vapor phase atoms or molecules as they interact with the growth front. Although high incident particle energy can be exploited, such as for orientation-selective resputtering for the growth of fully oriented films on amorphous substrates,[110] high-energy particles are usually regarded as a nuisance. Under high fluences, high particle energies can lead to resputtering of film constituents resulting in the non-stoichiometry defects discussed below.[111] The particles can also impact and sputter components in the vacuum chamber leading to the incorporation of unintentional impurities. However, even at low fluences, high particle energies can lead to nonequilibrium intrinsic point defects such as oxygen and cation vacancies, interstitials, and anti-site defects which can all negatively impact material properties, even in small concentrations. High-energy techniques such as sputtering and PLD tend to form larger concentrations of point defects in films whereas low-energy thermal techniques like MBE produce fewer defects. In principle, the use of oxygen plasmas could introduce high-energy particles into the growth chamber, but simple measures like thermalizers and deflection plates minimize their detrimental effects on growth.

The mean free path of the deposition process also plays a role in defect formation. The mean free path (λ) is calculated as:

$$\lambda = \frac{kT}{\sqrt{2}\pi d^2 P} \tag{2.1}$$

where k is Boltzmann constant, T is temperature, d is the kinetic diameter of atom or molecule, and P is the pressure. As shown, the mean free path is inversely proportional to pressure. In MBE, the mean free path exceeds the source-substrate distance by an order of magnitude or more. Thus, source species do not interact during transport from the source to the substrate. This eliminates the possibility of parasitic chemical reactions that can cause unintentional aerosol formation in low-vacuum techniques such as low-pressure chemical vapor deposition (LP-CVD). The high mean free path of MBE also limits deposition species to only those that originate from the surfaces in direct line of sight to the substrate. By using high-purity source material, high-temperature system bakeouts, and cryogenic cooling shrouds to limit surface outgassing, MBE can achieve extremely low impurity levels even when one reactor is shared among multiple material systems. These two advantages make MBE highly advantageous for the fundamental study of new materials. Finally, whereas low-vacuum methods like LP-CVD require the chamber's residence time to stop depositing one material and begin depositing another by pumping out one precursor and replacing it with another,[112] the high mean free path of MBE allows the use of shutters to make this switch nearly instantaneous, limited only by the speed of the shutter. This makes MBE the method of choice to deposit heterostructures that demand highly abrupt interfaces, even in commercial devices such as Hall effect sensors and high-electron mobility transistors. This ability to rapidly switch between two materials has also

been exploited to grow non-equilibrium structures such as high-index Ruddlesden-Popper phases.[113-119]

In PVD techniques with high particle energies, however, lower mean free paths can offer the advantage of lowering the particle energies through collisions with ambient gas molecules. This is the main motivation behind development of high-pressure oxygen sputtering which has been applied to cuprate superconductors,[120,121] $La_{1-x}Sr_xMnO_3$,[122] $PbZr_xTi_{1-x}O_3$,[123] amorphous $GdScO_3$ on Si,[124] $BaTiO_3$,[125] $SrTiO_3$,[126] and $BaSnO_3$,[127-129]

The high vacuum pressures of oxide MBE also offer the advantage of a high mean free path for electrons and ions required for *in-situ* materials characterization. Most research MBE systems use concurrent reflection high-energy electron diffraction (RHEED) to monitor the growth in real time, but *in-situ* characterization of MBE films has also been done with low-energy electron diffraction (LEED), low-energy electron microscopy (LEEM),[130] X-ray photoelectron spectroscopy (XPS), Auger electron spectroscopy (AES), Rutherford backscattering spectrometry (RBS), and scanning electron microscopy (SEM). The use of vacuum suitcases also allow samples grown by MBE to be transferred to distant characterization equipment—such as synchrotron facilities—without exposure to gases.[131]

2.4 Challenges with Oxide Molecular Beam Epitaxy

2.4.1 Cation Stoichiometry Control

The advantages outlined for MBE show great inherent potential for the technique; however, the method is not without challenges. Perhaps the most significant challenge for

MBE is control over stoichiometry. Because MBE relies on the co-deposition of individual elements, achieving cation stoichiometry is a major challenge, especially in semiconductors where small levels of nonstoichiometry can render a device useless. For example, in the semiconductor $SrTiO_3$, where Sr vacancies serve as acceptors, even a 0.1% drop in Sr flux would result in an acceptor concentration of 1.7×10^{19} cm^{-3}, enough to fully compensate even moderate doping concentrations. Although progress has been made using beam flux monitors (BFM), quartz crystal microbalances (QCM), atomic absorption spectroscopy (AAS) [132], electron-impact-emission spectroscopy (EIES) [133-135], or RHEED [136,137] to find-tune fluxes—many of them in real time—these techniques all involve errors around 0.1 – 1% [132,136,138].

The obstacle of stoichiometry was first overcome for the growth of III-V semiconductors by exploiting thermodynamics to self-regulate the stoichiometry. Figure 2.3a shows the thermodynamic equilibrium curves for the two reactions that can regulate the stoichiometry of GaAs [103]. As shown, at relatively low growth temperatures there exists a large range of As vapor pressures within which the stoichiometry is self-regulated. This range of pressure is referred to as a "growth window".

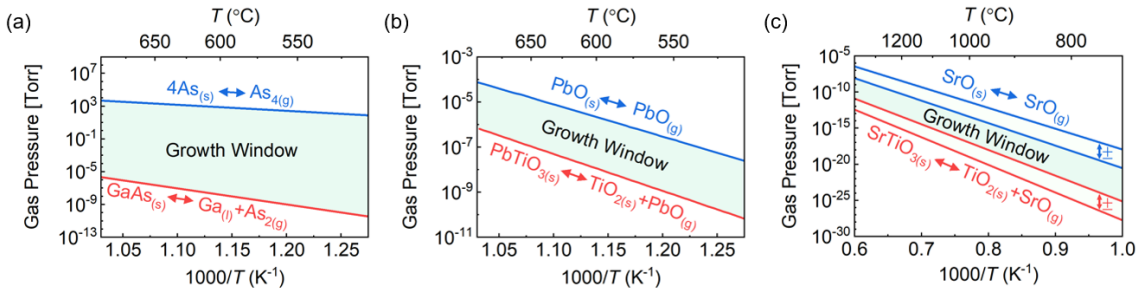

Figure 2.3: Adsorption-controlled MBE growth windows governed by the thermodynamic equilibrium curves if solid metal sources are used for (a) GaAs, (b) $PbTiO_3$, and (c) $SrTiO_3$.

Two sets of lines for both reactions are shown in the case of $SrTiO_3$ due to uncertainty in the thermodynamic data. Reproduced with permission.[103,139]

However, the concept of a MBE growth window was not demonstrated in oxides until decades later in the late 1990's.[102-104,140] Figure 2.3b shows the growth window of one of these early systems, $PbTiO_3$ and how the range of vapor pressures—spanning about 2 orders of magnitude—is considerably smaller than that of GaAs which spans about ten orders of magnitude.[103] In practice, this made the stoichiometric growth of $PbTiO_3$ feasible but challenging. Adsorption-controlled growth of other complex oxides using oxide MBE have since been found for a variety of materials,[17] but these windows are usually smaller than in GaAs and occur at higher temperatures.

Still, many complex oxides lack the volatile species necessary to support a growth window at realistic growth conditions. For example, $SrTiO_3$ lacks a sufficiently volatile constituent which makes the calculated growth window occur at very high growth temperatures or unreasonably low SrO vapor pressures, as shown in Figure 2.3c.[139] Thus, without a growth window, the stoichiometry of $SrTiO_3$ could only be as good as the control over the Sr and Ti fluxes. Given the difficulty of evaporating Ti, due to its low vapor pressure and the tendency of both Sr and Ti to oxidize at the source,[141,142] this control was quite poor. Growing $SrTiO_3$ low enough in defect concentrations to be a suitable oxide semiconductor was not feasible. Efforts have been made to combat the low vapor pressure and source oxidation by supplying Ti with a Ti-sublimation pump known as Ti-Ball.[141] Although $SrTiO_3$ films have been grown with high structural quality, stoichiometry control with traditional MBE is not sufficient to support robust semiconductor-like doping.

It was not until the hybrid MBE approach was developed that $SrTiO_3$ films could be grown with MBE having a sufficient degree of stoichiometry control to support chemical doping. Using titanium(IV) tetraisopropoxide (TTIP), a metal-organic precursor to supply Ti, it was first shown that a MBE growth window can exist for $SrTiO_3$ due to the high volatility of this compound.[139] A large growth window in terms of the Sr:TTIP flux ratio was shown, and stoichiometric materials could be obtained in a highly reproducible manner. Due to this control of the stoichiometry and the low-energy aspect of MBE growth, record low-temperature electron mobility has been achieved, even surpassing those of bulk single crystals. Electron mobility from MBE-grown films are now almost an order of magnitude larger than other techniques, with values of around 53,000 $cm^2V^{-1}s^{-1}$at 2 K[143] compared to 6,600 $cm^2V^{-1}s^{-1}$ by PLD.[144]

Since the first report of hybrid MBE, the use of metal-organic precursors for the adsorption-controlled growth of other perovskite oxides have been shown for other titanates,[145-147] vanadates,[148] and wide bandgap systems in the stannates.[149,150] Figure 2.4a shows the out-of-plane lattice parameters for one of these systems, $BaSnO_3$, as a function of the A- to B-site flux ratios.[151] Typically, what is seen, as shown here, is a constant out-of-plane lattice parameter within the growth window signifying stoichiometric growth. This is further evidenced in Figure 2.4b by enhanced electron concentration and mobility inside the growth window due to a decrease in compensating non-stoichiometric-related defects.

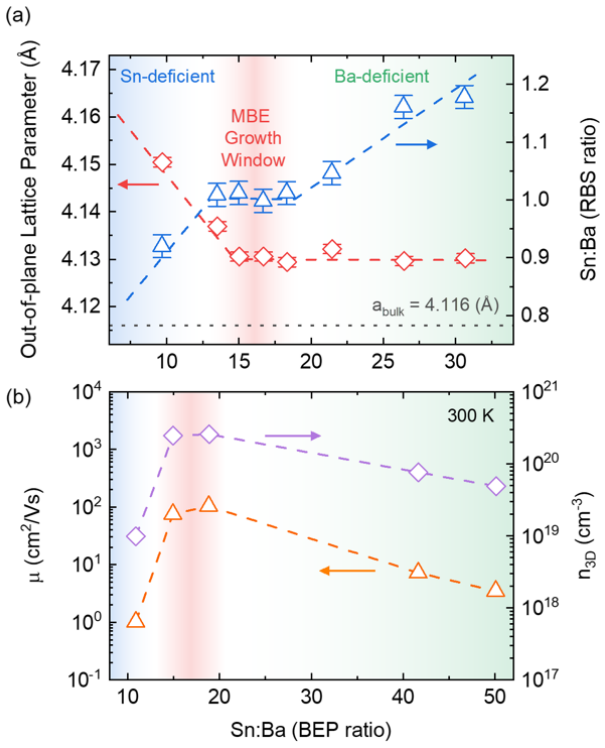

Figure 2.4: (a) Out-of-plane lattice parameter (left axis) and Sn:Ba atomic ratio from Rutherford backscattering spectrometry (RBS) (right axis) in hybrid MBE-grown $BaSnO_3$ films. (b) Room-temperature electron mobility (left axis) and carrier concentration (right axis) showing the enhanced electronic properties within the adsorption-controlled MBE growth window. Reproduced with permission.[151]

As a final note, it may also be possible to use thermal laser substrate heating to open up growth windows in some of these oxides systems by heating substrates up to incredibly high temperatures for growth. Looking at Figure 2.3c again, as the growth temperature is increased, the SrO vapor pressure needed will eventually reach feasible levels. By using a laser, for example a CO_2 laser, for substrate heating, substrate temperatures greater than 1500°C have been shown.[152]

2.4.2 Anion Stoichiometry and Oxidation

Another challenge with oxide MBE is fully oxidizing the cations to achieve oxygen stoichiometry. Figure 2.5 shows the standard oxidation potentials (E_0^{ox}) of select elements which are commonly used or sought after in complex oxide growth.[153] In some materials, especially transition metal-based perovskites like $SrTiO_3$, insufficient oxidation of one cation (in this case Ti^{3+} rather than Ti^{4+}) will lead to films with good structural quality, but high carrier concentrations due to oxygen vacancies serving as shallow donors.[154,155] Although this can be exploited for donors in the absence of chemical dopants, it is usually preferably to achieve full oxygen stoichiometry. For example, in dielectric and ferroelectric oxide systems, oxygen vacancies can cause considerable leakage currents and, therefore, negatively impact material and device properties.[156] In other materials, especially main-group metal-based perovskites like $BaSnO_3$, insufficient oxidation of one cation (Sn^0 or Sn^{2+} rather than Sn^{4+}) can be so severe as to ravage film quality altogether. For example, attempts to grow $BaSnO_3$ in inadequate oxidizing environments have resulted in formation of ostensible liquid tin metal droplets on the substrate during deposition.[157] In less severe cases of incomplete oxidation, $BaSnO_3$ also forms oxygen vacancies that act as shallow donors.[127,158] This diverse range of oxidation-related phenomena in $BaSnO_3$ make it an excellent case study of oxidation in MBE.

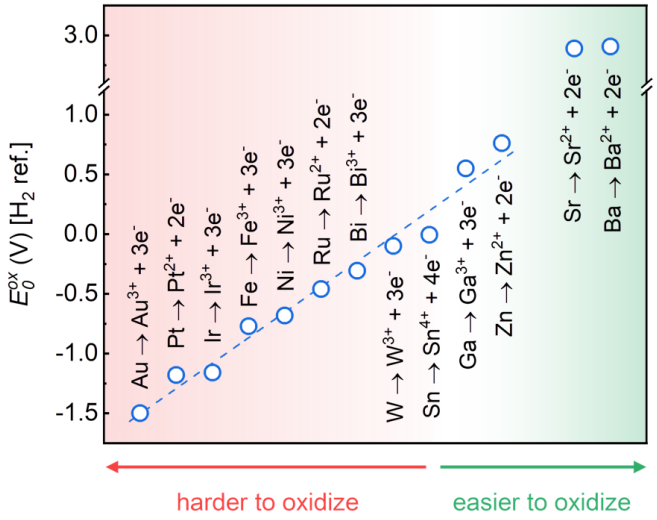

Figure 2.5: Standard oxidation potentials using a H_2 reference electrode for select metals[153] which are commonly used or sought after in MBE growth. Metals are ordered from harder to oxidize to easier to oxidize, left to right. The dashed line is a guide for the eye.

Two crucial factors which impact the oxygen stoichiometry in oxide MBE are the choice of oxidant and the oxidant background pressure. However the background pressure is usually limited to below 10^{-4} Torr by the mean free path constraints of MBE,[159] so only the choice of oxidant will be discussed. While molecular oxygen (O_2) has been used in early oxide MBE, its oxidizing power is not sufficient in many cases, notably requiring post-annealing to grow high-*Tc* superconductors.[96] A common solution to achieve a more aggressive oxidizing environment at the same background pressure is to activate the oxygen using inductively coupled plasma (ICP) which creates up to a few percent of highly reactive dissociated oxygen atoms.[86,160,161] For an even more aggressive oxidizing environment, electron cyclotron resonance (ECR) plasma can be used,[162-164] which can achieve a dissociation fraction exceeding twenty percent.[165] Another option is to generate ozone (O_3) and then, optionally, distill it to generate up to 100% ozone before it enters the

vacuum chamber.[97] Distilling ozone presents the potential hazard of explosions from its rapid decomposition, but this risk can be mitigated by distilling it over the high surface area offered by silica gel to prevent percolation of the liquid.[98]

Other oxidants have also been experimented with. Both nitrogen dioxide (NO_2) and hydrogen peroxide (H_2O_2) are noteworthy for being aggressive oxidants with relatively low vapor pressure; being easily absorbed onto cryo-shrouds they can achieve low background pressures even with high beam equivalent pressures.[166,167]

Even with these aggressive oxidizing species, the limited background pressures available in MBE may be insufficient to achieve full cation oxidation. One route to overcome this limitation is to supply oxygen bonded to one of the metal sources. This can be simply done by supplying the oxide of the metal, for example SnO_2 for the growth of $BaSnO_3$[108,157] and $SrSnO_3$,[168] or supplying the oxygen via the organic ligands in metal-organics as is done in hybrid MBE.[86] Using this second approach, it has been shown that $SrTiO_3$ films can be grown using only TTIP and no separate oxygen source, albeit with oxygen vacancies.[169] Alternatively, the ligand can be designed with reactivity toward oxygen sources. In a technique variation called "radical-based" hybrid MBE, Sn is supplied via the chemical precursor hexamethylditin (HMDT). At the growth front's elevated temperatures, the weak Sn-Sn bond at the center of the molecule undergoes homolytic cleavage affording trimethyltin radicals. These molecules react aggressively with oxidizing species, allowing the full oxidation of Sn even when unactivated molecular oxygen is used as the oxidant.[149] The organometallic HMDT has been used to grow stoichiometric films

of both $BaSnO_3$[109,149,151] and $SrSnO_3$[150,170-172] with growth windows present, shown in Figure 2.4 for $BaSnO_3$.

2.4.3 Source Oxidation

While a major challenge for early oxide MBE was to fully oxidize low-oxidation-potential metals such as Cu, there was a seemingly conflicting goal to prevent oxidation of high-oxidation-potential metals such as Y before they leave their crucible. This problem, coined "source oxidation" can alter the fluxes of these metals during growth, worsening the flux instabilities and nonstoichiometry discussed above,[141,173] One early strategy to combat source oxidation is to produce an oxidant pressure gradient across the chamber.[97] Baffles are added to separate the substrate and source regions of the chamber, with holes only large enough for the metal fluxes to reach the substrate. The oxidant is supplied centimeters away from the substrate while the two regions of the chamber are differentially pumped. This strategy provides a high oxidant pressure immediately surrounding the substrate where it is needed and a much lower pressure near the sources where it is unwelcome. Less extreme chamber design choices can also be implemented to lessen source oxidation. For example, extending the effusion cell port length will cause deposition of metal on the port walls between the effusion cell and the main chamber. These deposits can getter oxidizing species, minimizing the quantity that reaches the crucible;[142] narrowing the effusion cell port will enhance this effect.[174] Choosing a crucible with a small orifice or adding an aperture to the crucible can also slow the ingress of oxygen and improve flux stability.[175,176]

However these strategies all only lessen the effects of source oxidation; they do not solve it entirely. There are two strategies that thoroughly eliminate the problem of source oxidation by delivering the metal in a different chemical form. One way is to inject the element into the chamber in the form of a gaseous precursor, as done in hybrid MBE.[86] Regardless of the reactivity between the precursor and oxidizing species, the two do not interact until they are absorbed on the growth front. The second way is to evaporate the metal from an effusion cell in a form that does not react with oxygen. This can be a simple metal oxide, such as SnO_2,[157] or an air-stable precursor such as $Ru(acac)_3$ discussed below.[87]

2.4.4 Stubborn Metals: Ultra-Low Vapor Pressures and Oxidation Potentials

MBE often uses refractory metal filaments and crucibles to heat and contain transition metals during their high-temperature sublimation. This begs the question: how can one supply a refractory metal itself for MBE growth? Rather than uniformly heating an entire source load and crucible, a well-developed strategy is to use a focused energy beam that locally heats the source material to extremely high temperatures without drastically increasing the temperature of the crucible. The high-energy beam has historically been one of electrons, and is referred to as "electron-beam" evaporation,[162] but the new and exciting "thermal laser evaporation" techniques use a continuous laser mounted outside the vacuum chamber.[177] Focusing on the conventional method, electron-beam systems can be much more expensive than effusion cells, the required high voltage presents safety risks, the instrument operation can produce RF noise that interferes with other equipment,[178] the flux stability is poor, and some metals are prone to spitting. Finally,

electron-beam evaporation can be operationally complex, requiring monitoring and periodic electron beam alignment to avoid accidental crucible evaporation after source depletion.

Related to refractory metals, the Pt group is a set of metals which are not only extremely low in vapor pressure but also among the hardest metals to oxidize. Complex oxides containing Pt-group and refractory metals include ruthenates, iridates, tungstates, and Pt-group delafossites. A few of these materials have been grown using MBE with electron-beam evaporation and strong oxidants.[179-181] However, the above-mentioned challenges with electron-beam evaporation merit a search for an easier way to grow these materials with potentially higher quality. The lack of recent progress on the atomically-controlled deposition of these elements directly motivates one of the main focuses of this work. Addressing these issues through the development of solid source metal-organic MBE will be described further in Chapter 8 and 9.

2.4.5 Growth Rate

Another commonly cited problem with MBE is the extremely slow growth rates compared to other PVD techniques. While growth rates exceeding 1000 nm/hr have been shown in the MBE growth of III-V and III-nitride semiconductors,[182,183] as well as very recently in the growth of Ga_2O_3,[184] growth rates within complex oxide MBE are typically between 10 – 100 nm/hr. Such slow rates are a major deterrent for the use of conventional oxide MBE in commercial production. Attempts have been made to overcome this issue with various degrees of success. The main challenge associated with high growth rates in conventional oxide MBE has been non-stoichiometry-related defects forming after

increasing the fluxes of the individual species. $SrTiO_3$ is a good example of this, where the high level of oxygen background pressure needed to increase the growth rate has caused source oxidation and consequently non-stoichiometry.

It was not until the development of hybrid MBE that growth rates of several hundreds of nanometers per hour were achieved for complex oxides. By avoiding Ti source oxidation and supporting a growth window by supplying Ti as a gaseous precursor (TTIP), stochiometric $SrTiO_3$ films have been grown with rates exceeding 600 nm/hr.[185] With TTIP contributing to the oxygen supply, large oxygen background pressures were not required to increase the growth rate. In fact, the reported growth rates were limited by the size of Sr source and are predicted to approach 9 μm/hr if industrial sized Sr sources are used.[185]

2.5 Outlook for Oxide Molecular Beam Epitaxy

The evolution of the MBE growth technique has been discussed from the growth of III-V semiconductors to complex oxides. As new challenges have arisen, modifications have been made to the conventional approach to overcome them. Figure 2.6 summarizes the large amount of source and oxidant possibilities that have been developed. Due to MBE being a co-deposition technique, the ability to mix and match these sources has made this technique extremely flexible and one of the top tools of choice for addressing these challenges faced today.

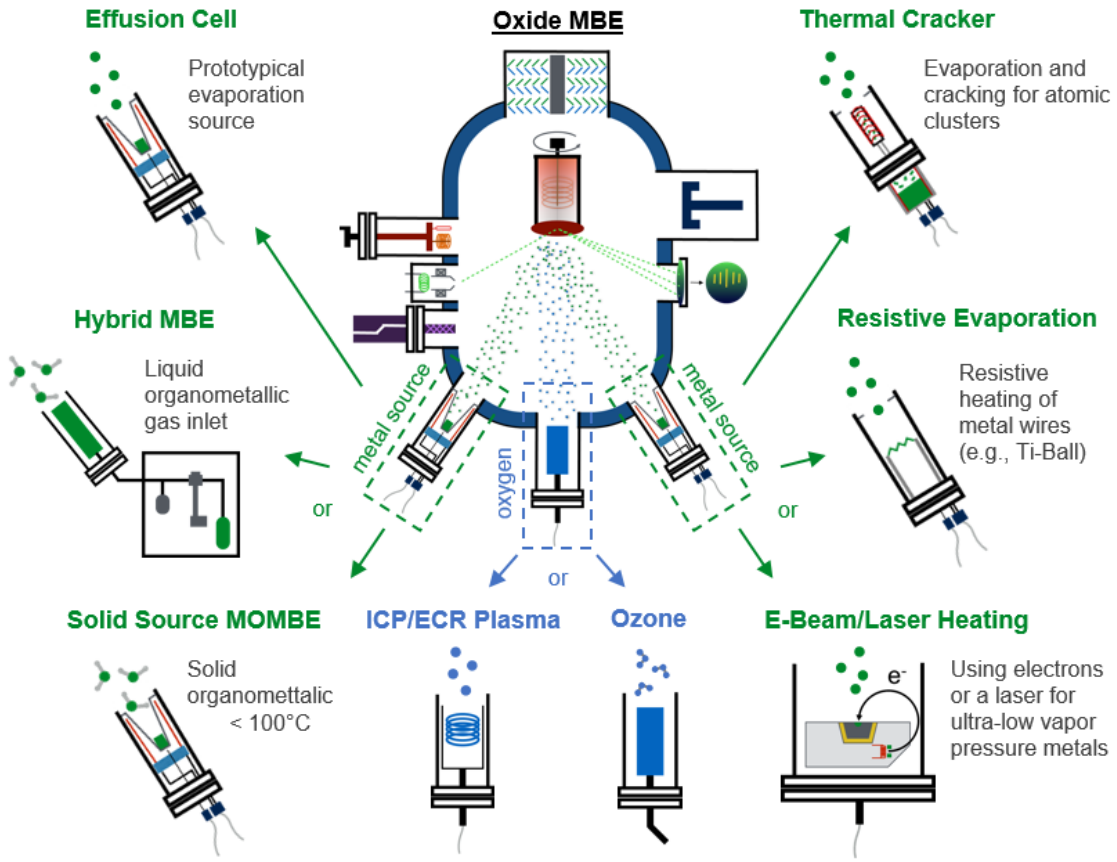

Figure 2.6: Schematic of the various common methods of delivering metal sources and oxidants in oxide MBE. Interchanging between sources has led MBE to become a very flexible technique.

MBE has drastically evolved to allow for the high-quality growth of a large range of materials. Prime examples are the perovskite oxide titanates and stannates which all have record electron mobilities achieved in oxide MBE-grown films, as seen in Figure 2.7. However, demonstrating similar results in the growth of all other complex oxide materials by MBE will require overcoming many of the challenges overviewed here: source oxidation, low oxidation potentials, ultra-low vapor pressures, and stoichiometry control. By employing the multitude of MBE modifications which now exist, it is only a matter of

time before more complex oxides are reproducibly grown and applied in next generation devices.

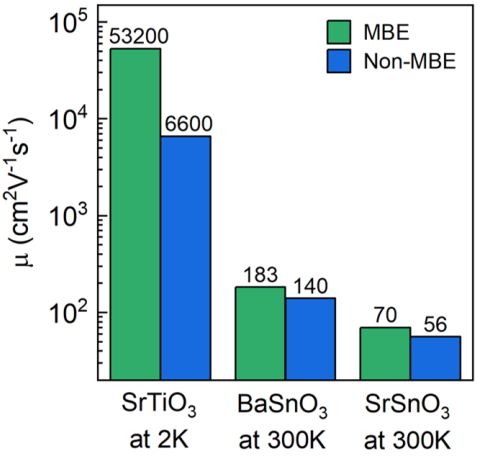

Figure 2.7. Record electron mobility for MBE and non-MBE films of $SrTiO_3$ at 2 K,[143,144] $BaSnO_3$ at 300 K,[108,186] and $SrSnO_3$ at 300 K.[170,187]

Chapter 3

3. Growth, Characterization, and Device Fabrication

3.1 Hybrid Molecular Beam Epitaxy Growth

All films in this work, outside of those in Chapter 8 and 9, were grown using the hybrid MBE technique. Those in Chapter 8 and 9, instead, were grown using the solid source metal-organic MBE approach, which was developed for this first time here. Because of the novelty of this approach, the details of those growths can be found separately in those relevant chapters. However, both film synthesis approaches used the same oxide MBE chamber (EVO 50, Omicron NanoTechnology, Germany) and equipment, which will be described here in more detail for the hybrid MBE technique. Any differences from this growth description will be mentioned explicitly in the following chapters.

The metal-organic precursors used, which are the key factor and modification in hybrid MBE, were TTIP for Ti and HMDT for Sn. These precursors were supplied through in-lab fabricated external gas inlet systems, see Figure 3.1. These inlets begin with a heated bubbler containing the precursor, heating to a temperature suitable for achieving ~ 10 Torr of vapor pressure, about 80°C and 60°C for TTIP and HMDT, respectively. No carrier gas

is used. The vapors then travel through heated lines and through a linear leak valve, which controls the pressure supplied by feedback control from a controller and a pressure read by a Baratron capacitance manometer further down the line (MKS Instruments, US). Finally, the vapor is introduced into the system by a gas injector (E-Science, Inc., US) which allows for an interface between the higher-pressure line and the ultra-high vacuum chamber.

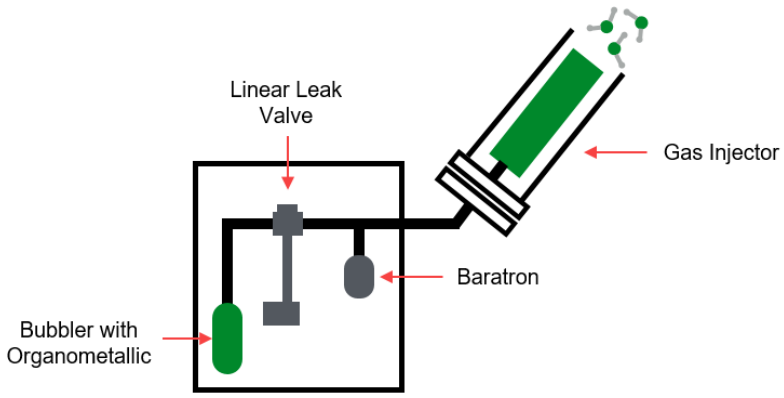

Figure 3.1. Schematic of the external gas inlet systems used in the hybrid MBE process.

Effusion cells (E-Science, Inc., US and MBE-Komponenten GmbH, Germany) were used for the sublimation of metallic elements Ba and Sr as well as La when used as a dopant. Fluxes of the metals and metal-organics were measured as a beam equivalent pressure (BEP) using a beam flux monitor inserted below the substrate before growth. Oxygen was supplied using a radio frequency inductively coupled plasma source (Mantis, UK) with a power of 250 W and with charge deflection plates. Oxygen background pressure was ~ 10^{-6} – 10^{-5} Torr.

Films were grown on a variety of single crystal substrates with growth temperatures typically of ~ 900°C – 950°C for the perovskite oxide growths. Before growth, but at growth temperature, the substrates were cleaned with the oxygen plasma source for 20 – 30 minutes. Following growth, films were also cooled down in the oxygen plasma environment until about 300°C. Keeping the sample in oxygen is key for decreasing oxygen vacancy concentrations in the film and the substrate which is important for decreasing leakage in materials like BTO and remaining insulating in materials like STO.

3.2 X-Ray Diffraction

X-ray diffraction (XRD) is a powerful technique that gives valuable information on the atomic crystalline structure of materials. XRD works on the wave nature of X-rays and the interference of diffracted, or elastically scattered, waves when interacting with periodic crystalline solids. Diffraction occurs when the interplanar spacing of a material is similar in size to the wavelength (λ) of the X-ray. Typically, X-rays emitted from copper are used because their wavelengths are close to the spacing in many solids (Cu K_α = 1.5406 Å and Cu K_β = 1.3922 Å). However, a monochromator is commonly employed to separate the various wavelengths and only allow one to interact with the sample, thereby simplifying analysis.

After interacting with a crystalline material, X-rays can either destructively or constructively interfere with one another. Constructive interference occurs when the path distance between scattered X-rays ($2d_{hkl}\sin\theta$) is an integer multiple of their wavelength ($n\lambda$). This is represented by Bragg's law

$$n\lambda = 2d_{hkl} \sin\theta \quad (3.1)$$

where n is any positive integer, d_{hkl} is an interplanar spacing, and θ is the angle between the incident X-rays and the sample surface. Constructive interference then leads to increased collected intensity of the scattered X-rays only at specific angles, known as Bragg angles, which can be directly related to the interplanar spacing. Also, depending on the crystal symmetry, only certain planes can cause constructive interference and can be predicted by the structure factor, which is a mathematical description of how a crystal scatters incident X-rays. Therefore, the collected diffraction pattern can give information on both crystal lattice parameters and symmetry.

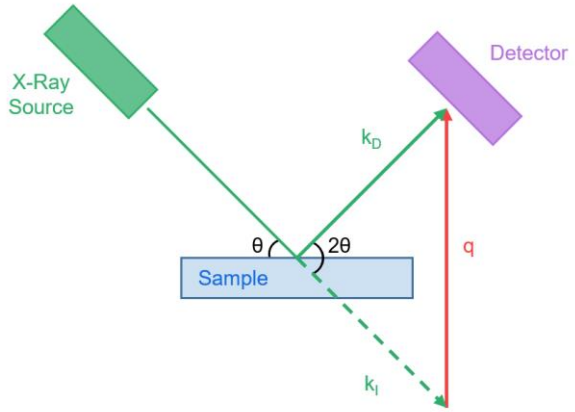

Figure 3.2. Schematic view of XRD set-up and the incident, diffracted, and scattering vector.

When it comes to single crystalline epitaxial films, as will be the focus in this work, high-resolution X-ray diffraction (HRXRD) coupled scans are typically used to determine the out-of-plane structural parameters of the film. Because a family of film crystalline planes should be oriented parallel to substrate surface, the scattering vector (q), which is

the incident wave vector (k_I) minus the diffracted wave vector (k_D), of the scattered X-rays points directly up from this crystalline surface. By coupling the source and the detector such that the scattering vector has no in-plane component, the d_{hkl} spacings parallel to the surface can be determined. To maintain this vertical scattering vector, the angle of the incoming X-rays will be changed while simultaneously rotating the detector, hence being referred to as a coupled scan.

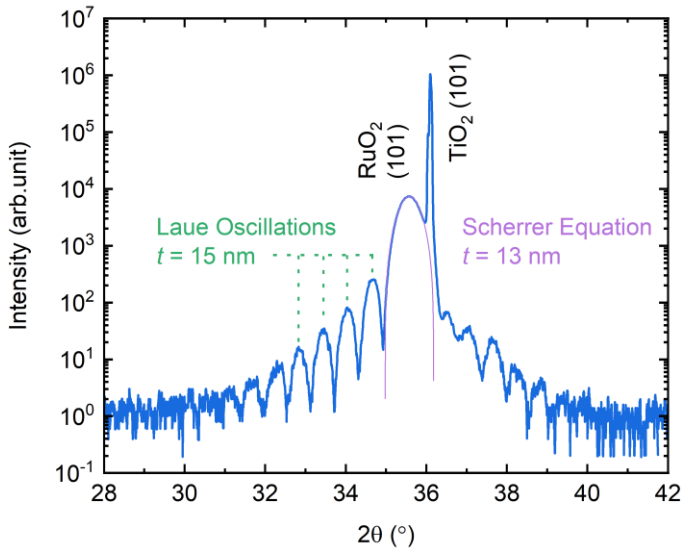

Figure 3.3. HRXRD coupled scan of a RuO_2 film grown on TiO_2 (101) substrate. Laue oscillations are present and give a film thickness of 15 nm. Estimation of the thickness from the Scherrer equation is 13 nm, in pretty good agreement with the thickness fringes, indicated the lack of considerable microstrain.

Another consequence of HRXRD coupled scans, when films are of very high quality on a short lateral length scale, is the appearance of finite-size thickness fringes, or Laue oscillations, as can be seen in Figure 3.3. The spacing between these fringes in 2θ, as

diffraction intensities are usually plotted against, can be used to determine the thickness of the film (t) by the following equation

$$2t \sin \theta_L = n_L \lambda \tag{3.2}$$

where θ_L is the angle of a Laue oscillation and n_L is the assigned integer number of the fringe. Therefore, plotting $\sin\theta_L$ vs n_L should give a linear line with a slope of $\lambda/2t$.

The film thickness can alternatively be estimated by the line or peak broadening of the scattered X-rays in a diffraction pattern by the Scherrer formula

$$t = \frac{0.9\lambda}{\beta \cos \theta} \tag{3.3}$$

where β is the full width at half maximum (FWHM). This relation is typically used to estimate grain sizes in polycrystalline materials but for single crystal films that are free from microstrain, which also affects peak broadening, the thickness from this relation can be used. Many coupled HRXRD diffraction patterns will be shown throughout this work and will be used to determine lattice parameters, epitaxial orientation of the film to the substrate, and film thicknesses.

Additionally, information on the crystalline disorder through the mosaicity, or the spread of the slight differences in orientations of a plane, can be measured using HRXRD rocking curve scans. No crystal is perfect so there are always these slight differences in the orientations of a plane, even when oriented parallel to a substrate surface. Here, the source and detector are aligned to the Bragg condition of the film peak for the plane to be measured, and the sample is "rocked" in ω to measure the degree of misalignment of the

plane. The FWHM of the rocking curve is commonly reported and used, for example, as a measure of the imperfections or defects such as dislocations arising from strain relaxation.

Finally, reciprocal space mapping (RSM) is an XRD technique that allows for gathering of information about not only the out-of-plane lattice parameters (a_{op}), but also the in-plane ones (a_{ip}). Here, unlike a coupled scan, scattering vectors which are not completely vertical to the surface are studied and, from their out-of-plane and in-plane components, lattice parameters or plane spacings in both the out-of-plane and in-plane directions can be determined. These scattering vectors can be viewed on a reciprocal lattice, which can be made from any real lattice of a crystal. The distance from the origin of the reciprocal lattice to the reciprocal lattice point ($|q|$) for the plane in question gives the interplanar spacing in the real lattice by

$$\frac{1}{d_{hkl}} = \frac{|q|}{2\pi} \tag{3.4}$$

From this equation, relations for the in-plane spacing (d_{ip}) and out-of-plane spacing (d_{op}) can be derived as follows

$$q_x = \frac{2\pi}{d_{ip}} = \frac{2\pi}{\lambda}[\cos\omega - \cos(2\theta - \omega)] \tag{3.5}$$

$$q_z = \frac{2\pi}{d_{op}} = \frac{2\pi}{\lambda}[\sin\omega + \sin(2\theta - \omega)] \tag{3.6}$$

where q_x and q_z are the in-plane and out-of-plane components of the scattering vector.

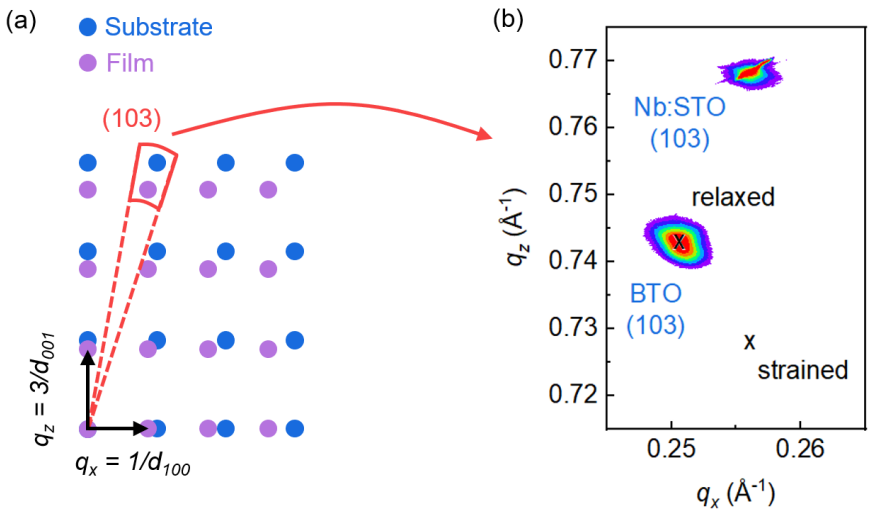

Figure 3.4. (a) Reciprocal lattice points for both a substrate (blue) and film (purple). Red line outlines a scan around the (103) peaks. Scanning in the radial direction is 2θ while the tangential direction is ω. (b) (103) RSM of a completely relaxed 400 nm BTO film grown on a Nb-doped STO (001) substrate. Expected relaxed and completely strained positions are marked.

For epitaxy, knowing the a_{ip} is important for determining the strain state of the film and RSMs will be used in this work for mostly this reason. For a completely coherent film, a_{ip} will be equal to that of the substrate, for a completely relaxed film, a_{ip} will be equal to the bulk, and for a partially relaxed film, a_{ip} will be somewhere in between.

3.3 Reflection High-Energy Electron Diffraction

One of the advantages of MBE being an ultra-high vacuum deposition technique is the capability of RHEED (Staib Instruments, Germany). This diffraction technique allows for *in-situ* surface analyzation during growth and works on the same principle as other diffraction techniques such as X-ray diffraction. The key difference here is the angle of the incident electron beam, typically between 1 and 5 degrees, which allows for only the first

few atomic planes of the surface to be probed. The information taken from RHEED is related to crystal symmetry, periodicity, surface reconstructions, and the growth mode of the depositing film. RHEED is similar to another technique, low-energy electron diffraction (LEED), but the collected diffraction in RHEED usually consists of streaks instead of spots and the energy of the electron beam is much higher, 5 – 100 keV compared to about 100 eV. The higher energy electrons give a larger mean free path and allow for the operation at the more grazing incidence.

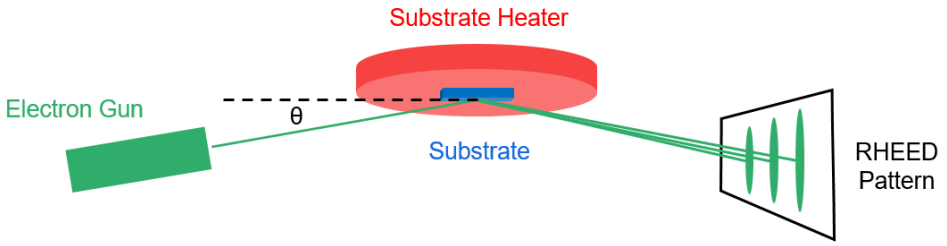

Figure 3.5. Schematic view of RHEED which involves an electron gun, crystalline substrate/film, and the collected RHEED pattern.

In contrast to most diffraction techniques, the collected pattern in RHHED typically consists of streaks instead of spots. As diffraction only occurs from the surface, in the ideal case of a 2D layer of periodically spaced atoms, the reciprocal lattice is then comprised of 1D rods normal to the film surface. The diffraction condition is achieved when these rods intersect the Ewald sphere, a sphere whose radius is inverse of the incident wave's wavelength. For a perfect crystalline surface made of one single plane of atoms, this would appear as spots. However, due to deviations from this perfect surface and the presence of domains in real cases, streaks form instead. The spacing of these streaks give information

on the atomic spacing and their shape on the surface construction. Additionally, extra diffracted streaks can occur between the fundamental reflections and are based on surface reconstructions, giving valuable information on the structure of the surface compared to the bulk. Figure 3.6 shows typical RHEED patterns viewed from different surfaces.

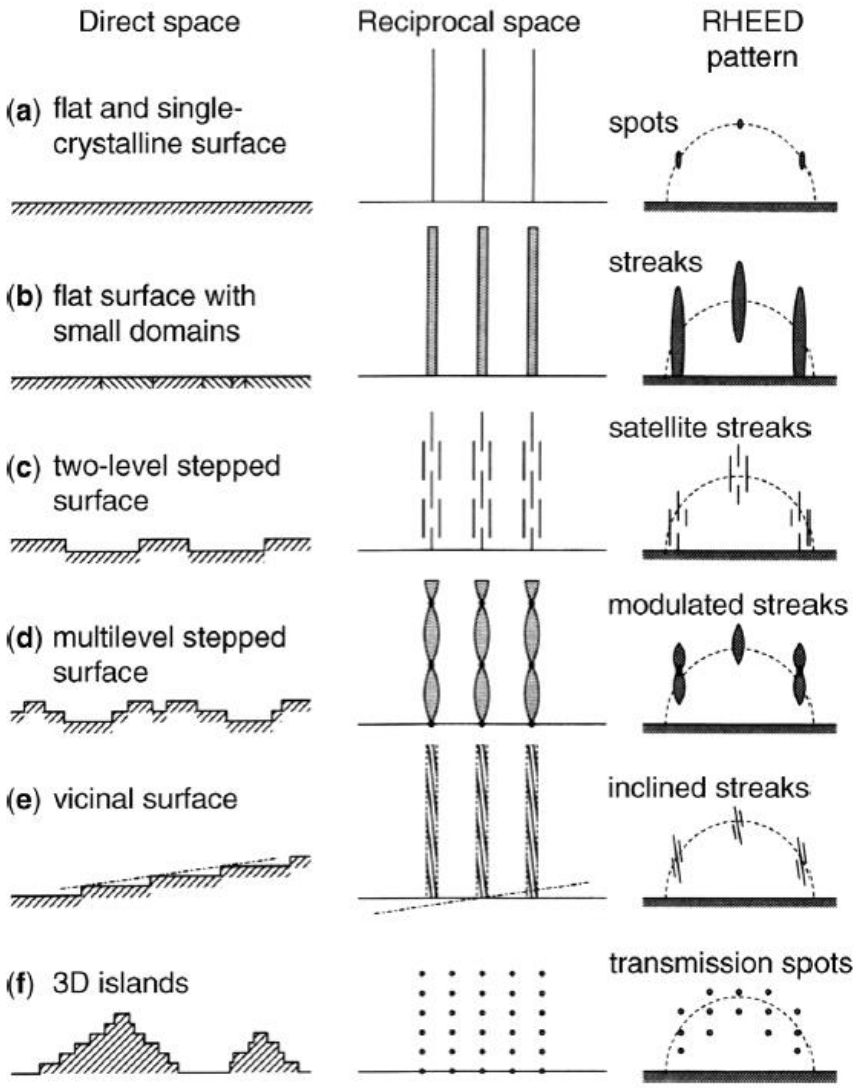

Figure 3.6. Typical surface morphologies and the corresponding reciprocal and RHEED patterns. Reproduced with permission.[188]

A large advantage of RHEED vs LEED is the additional information gained about and from the growth mode. For example, by monitoring the intensity of a reflection in RHEED, one can determine the growth rate if the growth is in a layer-by-layer Frank-van der Merwe growth mode. The roughening and then smoothing of the surface as each layer is formed causes the intensity to decrease and then increase, respectively. The time between each oscillation is the time it takes to grow one complete layer, or unit cell. These "RHEED oscillations" give a materials scientist great control over the film growth, monolayer growth control, and allow for precise termination of layers which is very useful for growth of heterostructures and superlattices.

Another growth mode, step-flow growth, is usually indicated by an initial roughening or decrease in intensity, followed by an increase in intensity as the first layer forms, and then a constant intensity as the step-flow growth proceeds. Volmer-Weber island growth can be viewed by the loss of streaks and the appearance of spots, as the electrons are transmitted through the formed islands instead of reflecting from the planar surface. Finally, Stranski-Krastanov, which involves a layer-by-layer growth followed by island growth, can be viewed as RHEED oscillations occurring with an overall decrease in the reflected intensity as film growth proceeds.

3.4 X-Ray Reflectivity

Instead of X-ray interference between periodic crystalline planes, X-ray reflectivity relies on interference between interfaces, commonly the film-air interface and the substrate-film interface. Should these two interfaces be present with minimal roughness,

oscillations known as Kiessig fringes will occur. The frequency of the oscillations depends on the distance between these two interfaces, e.g., the thickness of the film. Kiessig developed a formula based on the complex refractive index of a material's interaction with X-rays and Snell-Descartes' law. The formula is

$$\sin^2\theta = \left[\left(\frac{n\lambda}{2t}\right)\right]^2 + 2\delta \tag{3.7}$$

where n is the order of the reflection and δ is twice the critical angle of reflection.

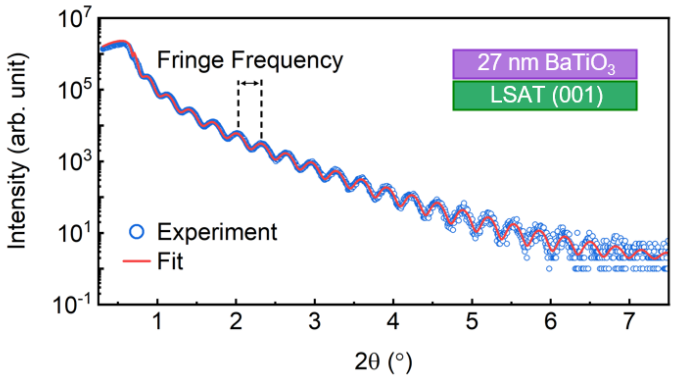

Figure 3.7. GIXR experimental data and simulated fit to the Kiessig formula for a BTO film grown on a $(LaAlO_3)_{0.3}(Sr_2TaAlO_6)_{0.7}$ (LSAT) (001) substrate. The fit gives a film thickness of 27 nm.

In this work, the reflectivity measurements performed are known as grazing-incidence X-ray reflectivity (GIXR) due to the small angle of the incident X-rays. GIXR can be used for more in-depth analysis of the properties of interfaces, since the reflection depends on the material's electron density and surface roughness, but here it will mostly be used to determine film thickness. Figure 3.7 shows a representative GIXR measurement for a BTO film and fitting using the GenX software.

3.5 Atomic Force Microscopy

Atomic force microscopy (AFM) is a form of scanning probe microscopy (SPM) that allows for characterization of sample surfaces with resolution better than the optical-diffraction limit including topography imaging and electrical, magnetic, and mechanical force measurement. In the simplest configuration, AFM consists of a laser diode which shines a small spot on a spring-like cantilever and is then collected by a photodiode, as can be seen in Figure 3.8a. The cantilever is either dragged (contact mode), tapped (tapping mode), or oscillated (peak-force mode) across the surface of the sample in a raster motion and any changes in the deflection of the laser is collected and analyzed. Deflection in the vertical direction is a consequence of the bending of the cantilever from, for example, from the topography or Van der Waals forces while deflection in horizontal direction is from any twisting of the cantilever, usually related to forces like friction.

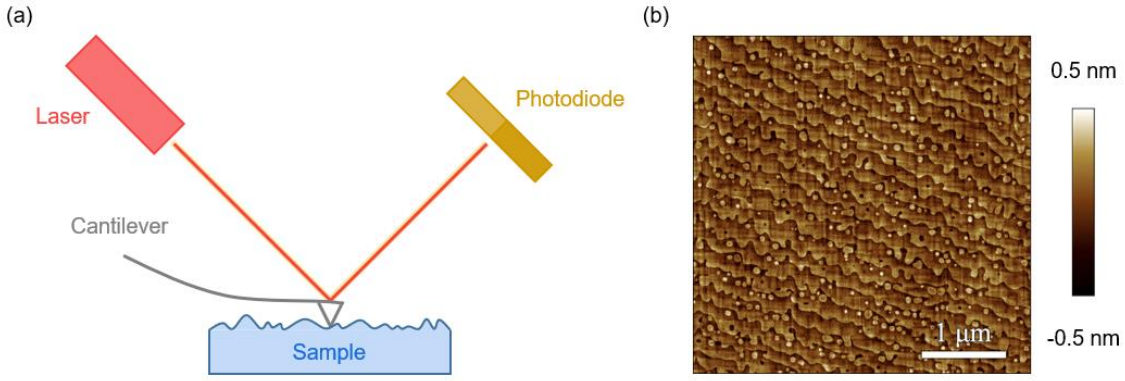

Figure 3.8. (a) Simple schematic of an AFM set-up. (b) AFM image of a 20 nm BTO film grown on a Nb-doped STO (001) substrate. Atomic steps can be seen on the surface with the height on unit cell of BTO.

AFM will mostly be used for in this work to measure the surface topography and to characterize features on the surface such as domains or morphologies arising from differences in growth conditions or growth modes. An example is given in Figure 3.8b for a BTO film grown on Nb-doped STO (001) substrate. Measurements were done on a Bruker Nanoscope V Multimode 8.

3.6 X-Ray Photoelectron Spectroscopy

X-ray photoelectron spectroscopy (XPS) is a characterization technique which can give information on composition, electronic structure, oxidation state, and the chemical environment of atomic species. XPS works, in principle, based on the photoelectric effect. X-rays with a known wavelength or energy, usually Al K_α X-rays (photon energy = 1486.7 eV), are supplied by an X-ray source and then interact with the sample of interest. The X-ray photons are absorbed by the atoms in the sample and a photoelectron is ejected, if the energy of the X-ray is larger than that of the binding energy of the electron. The kinetic energy of this electron (E_K) is measured and, because the energy of the incident X-ray is known ($h\nu$), the binding energy (E_B) of the emitted electron can be determined by the following relationship, where φ is the work function of the material.

$$E_B = h\nu - E_K - \varphi \tag{3.8}$$

By measuring E_K, one can then determine, from E_B, the element from which the electron was emitted, which orbital it was emitted from, and the immediate chemical surroundings.

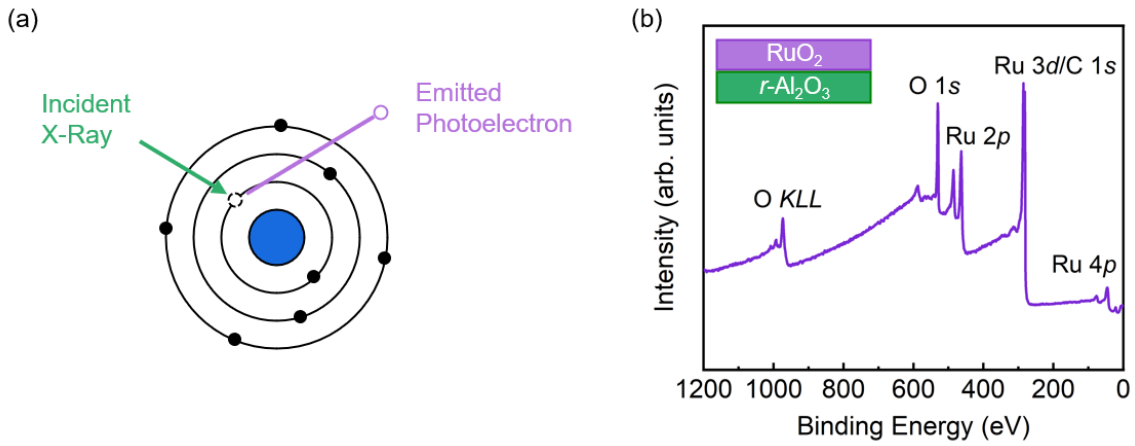

Figure 3.9. (a) Schematic view of a photoelectron emitted from a core level of an atom due to an incident X-ray. (b) Representative XPS survey spectrum of RuO_2 grown on R-plane sapphire (r-Al_2O_3).

Although XPS is a powerful technique, it does have its limitations. For the work done here, these limitations are mainly based around XPS being restricted to measuring the first few nanometers of the surface of a material and the inherent error in determining the atomic compositions, generally 1 – 2%. Determining the overall composition of a film can be difficult for these two reasons as changes in the chemical makeup can occur just at the surface of a film and the level of error here can miss slight but important changes in stoichiometry. Nevertheless, XPS will be used (PHI 5000 VersaProbe III Photoelectron Spectrometer) to give an estimation of film stoichiometry and atomic ratios as well as for determining oxidation states.

3.7 Impedance Spectroscopy

Impedance spectroscopy, sometimes call dielectric spectroscopy, is a technique used to study the response of a material to an applied alternating current (AC) electric field,

usually as a function of the frequency of the field oscillations. The interaction of dipoles within a dielectric material with the AC field gives information on properties such as dielectric constant and dielectric loss.

An ideal resistor follows Ohm's law, $R = V/I$ where R is the resistance, V is the voltage, and I is the current. Ideal resistors not only follow this law, but they also have a resistance value independent of frequency and do not change the phase of an applied alternating current. In reality, however, many materials are more complicated than an ideal resistor and this forces the use a more complex parameter, impedance. Impedance (Z) describes the effective resistance of a material to an alternating current, or the resistance to an alternating current in terms of both magnitude and phase. Ohm's law can be re-written for impedance as function of time (t) as

$$Z = \frac{V_t}{I_t} = |Z| \frac{\sin(\omega t)}{\sin(\omega t + \phi)} \tag{3.9}$$

where $|Z|$ is the magnitude of the impedance, ω is the frequency, and ϕ is the phase shift. Impedance can alternatively be represented as a complex number

$$Z = |Z|(\cos\phi + j\sin\phi) = R + jX \tag{3.10}$$

where R is the resistance and X is the reactance.

Impedance is commonly used for fitting an equivalent circuit model for a measured system. Circuits are typically made of resistors, capacitors, and inductors whose respective impedances are given by

$$Z = R \tag{3.11}$$

$$Z = \frac{1}{j\omega C} \tag{3.12}$$

$$Z = j\omega L \tag{3.13}$$

where C is the capacitance and L is the inductance. For capacitors, sometimes individual capacitive elements do not behave ideally and are instead described by a constant phase element (CPE) whose impedance is given by

$$Z_{CPE} = \frac{1}{Q(j\omega)^{\alpha}} \tag{3.14}$$

where α describes how far from an ideal capacitor the element is (α = 1 for an ideal capacitor) and Q is a frequency independent constant that equals the capacitance when α = 1. In total, adding these elements in parallel or in series makes up an equivalent circuit.

As mentioned, impedance spectroscopy is also commonly used to determine the dielectric properties of a material. By applying an alternating current to a metal-insulator-metal capacitor structure with the dielectric material of interest as the insulator, one can measure the real and imaginary part of the impedance, or R and X, respectively. The following relations are then used to determine the real part of the dielectric constant (ε'), the imaginary part of the dielectric constant (ε''), and the dielectric loss tangent ($\tan\delta$)

$$\varepsilon' = \frac{-X}{\omega C_0(R^2 + X^2)} \tag{3.15}$$

$$\varepsilon'' = \frac{R}{\omega C_0(R^2 + X^2)} \tag{3.16}$$

$$\tan\delta = \frac{R}{X} \tag{3.17}$$

where $C_0 = \varepsilon_0 A/d$, ε_0 being the permittivity of free space, A the electrode area, and d the insulating dielectric layer thickness.

Impedance spectroscopy will be used here (E4990a Impedance Analyzer, Keysight Technologies, USA) to determine the dielectric properties of grown dielectric and ferroelectric films as well as to perform equivalent circuit fitting to determine effects from intrinsic and extrinsic effects, like resistances from contacts and leakage across the film.

3.8 Metal-Insulator-Metal Device Fabrication

To perform dielectric, ferroelectric, and leakage current measurements, films need to be grown on a conducting bottom electrode and then fabricated into a complete metal-insulator-metal (MIM) device. The simplest way to achieve this is to grow the film on a conducting bottom substrate which can then act as the bottom electrode in the device. For perovskite oxides, conducting Nb-doped $SrTiO_3$ substrates make a good bottom electrode and will be used for the majority of the devices in this work. Alternatively, a conducting film can be grown *in-situ* and act as a bottom electrode as well. For the top electrode, metals which form a Schottky contact are desirable because this will inhibit the flow of current, or leakage, through the device. Also, materials which can efficiently screen the electrostatic charge at the electrode-film interface are beneficial as this will help with decreasing the "dead layer" in large dielectric constant materials like BTO. Platinum was the metal of choice here because its large work function should create this Schottky contact and it can effectively screen electrostatic charge with most materials.

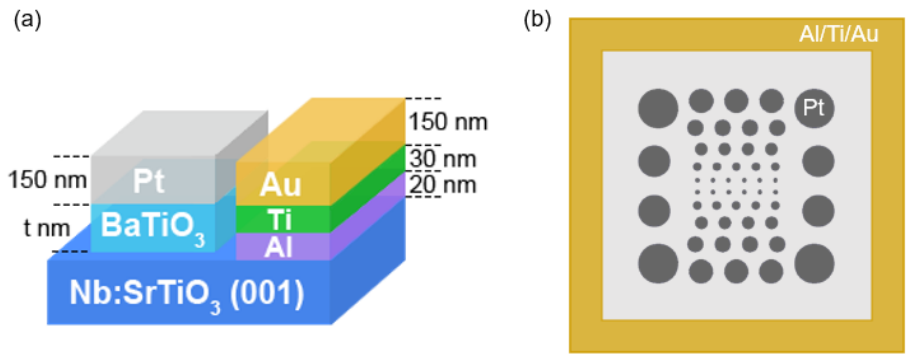

Figure 3.10. (a) Side and (b) top schematic view of fabricated BTO MIM capacitor. Electrode radii in panel (b) from smallest to largest are 25, 50, 75, 100, 150, 200, 250 μm.

Device fabrication for all films were performed using the following procedure unless explicitly stated otherwise. Following MBE growth, samples were removed and transferred to an AJA ATC 2000 sputter system (AJA International, Inc., USA) for ~ 150 nm of Pt to be deposited at room temperature. Next, photoresist was spun and patterned using a standard photolithography process. The pattern consisted of multiple electrodes of various sizes, radii from ~25 μm to 250 μm. All measurements in this work were done on electrodes with radii of 100 μm. After spinning the photoresist, performing the exposure, and doing the development, the Pt top electrodes were formed by ion mill etching (Intlvac Thin Film Corporation, USA) through the entire top Pt layer and into either the dielectric or bottom electrode. Next, contacts needed to be made to the bottom electrode. If the etch process did not reach the substrate, a further etch would be done around the outside of the sample, far from the electrodes located in the center.

The ion mill etching process is known to make perovskite oxides conducting, so following this step an oxygen anneal was done. Films were annealed for one hour at 900°C

in an oxygen-rich environment in a tube furnace. The oxygen anneal also served the purpose of decreasing oxygen vacancy concentrations in the perovskite oxide films, which would be present even without etching. Although probing of the bottom electrode would then be possible following the etching process, making Ohmic contact directly with perovskite oxides can be difficult. For this reason, metal contacts would be sputtered, once again, around the outside of the sample on top of the bottom electrode. These contacts were 20 nm Al / 30 nm Ni or Ti / 150 nm Au. Al makes a good Ohmic contact to most perovskite oxides, Au acts as a barrier to oxidation, and Ni or Ti was inserted in between to inhibit intermixing of Al and Au.

Chapter 4

4. Hybrid Molecular Beam Epitaxy Growth of $BaTiO_3$

The ability to reproducibly synthesize thin films with precise composition and controlled structure is essential for fundamental study and mass production. Here, the hybrid MBE is used for the growth of epitaxial, single crystalline $BaTiO_3$ films of different thicknesses on Nb-doped $SrTiO_3$ substrates with atomically smooth surfaces. By combining scanning transmission electron microscopy, temperature-dependent HRXRD, RHEED, and AFM, the effect of growth conditions and the interplay between stoichiometry and epitaxial strain on the resulting structure is studied. Furthermore, a close to bulk-like ferroelectric phase transition in thicker films is demonstrated and highlights the effect of strain on the phase transition temperature. This work establishes the hybrid MBE approach for the growth of heteroepitaxial $BaTiO_3$ films on conducting substrates with scalable thickness and controlled stoichiometry.

This chapter was adapted from: William Nunn, Sara Sandlass, Maike Wegner, Ryan Haislmaier, Abinash Kumar, Malleswararao Tangi, James LeBeau, Eckhard Quandt, Richard D. James, and Bharat Jalan. Hybrid Molecular Beam Epitaxy Growth of $BaTiO_3$ Films. *J. Vac. Sci. Technol. A* **39** (2021).

4.1 Introduction

Growth of thin film BTO has been reported using various thin film deposition techniques including MBE which has the advantages of being able to produce materials with atomic-layer control and low in impurities, leading to high quality BTO films.[145,189,190] MBE growth of BTO films can prove difficult, however, mostly due to the problem associated with stoichiometry control. Regulating the relative Ba/Ti metal fluxes is often challenging, and, in oxide MBE, oxygen deficiency can also occur, as a relatively low oxygen background pressure (~ 10^{-5} – 10^{-6} Torr) must be used to maintain the characteristic MBE large mean-free path. While oxygen deficiency can be overcome by post-growth annealing, controlling cation stoichiometry is still a major challenge.

Recently, advances have been made in MBE synthesis to include metal-organic-based hybrid MBE techniques which replace solid elemental metal sources with metal-organic compounds. Using this approach, it has been shown that an adsorption-controlled "MBE growth window" for self-regulating stoichiometry exists for a variety of compounds, including titanates,[86,139,145] vanadates,[148] and stannates.[149] Of the titanates, a few reports exist for BTO involving hybrid MBE growth, however,[145,147,191-193] only one report directly address the growth window.[145] BTO was shown to grow completely coherently on an insulating $GdScO_3$ substrate where the growth window was identified by a Ba to Ti flux ratio region within which films displayed a constant out-of-plane lattice parameter.[145] Here, a closer look is taken at the growth of BTO films using hybrid MBE and study the effect of growth conditions and film thickness when grown on the more

commonly used conducting Nb-doped $SrTiO_3$ substrates which is expected to not support coherent growth past a few nanometers.

4.2 Hybrid MBE Growth and Characterization

The hybrid MBE growth technique was used for the deposition of BTO films, as was described in Chapter 3.1. Films were grown on Nb-doped $SrTiO_3$ (001) (Nb:STO) substrates at 950°C. Relative growth conditions were determined from the ratio of the Ti:Ba fluxes measured as a beam equivalent pressure using a beam flux monitor inserted below the substrate prior to growth. Growth rates ranged from ~ 50 – 60 nm/hr. Post-growth annealing was done, after initial characterizations, in an oxygen-rich environment in a tube furnace operated at 900°C for one hour.

Cross-sectional scanning transmission electron microscopy (STEM) samples of the BTO thin film were prepared using mechanical wedge polishing followed by Ar ion milling to obtain an electron transparent sample. STEM imaging was performed using a probe-corrected FEI Titan G2 60-300 kV S/TEM equipped with an extreme field emission gun (X-FEG) and was operated at 200 kV with a beam current of 50 pA and probe convergence semi-angle of 19.6 mrad. The high-angle annular dark-field (HAADF-STEM) collection inner semi-angle was 77 mrad. Drift and scan distortion correction were applied using the revolving STEM approach.[194]

A representative HRXRD pattern for a BTO film grown on Nb:STO is shown in Figure 4.1a. Single peaks are present for the (001) planes showing single crystalline, epitaxial films consistent with the single domain structure of the tetragonal *c*-axis oriented

out-of-plane. Finite thickness fringes, evidence of high structural quality on a short lateral length scale, were present around the (001) peak. The surface of the BTO film consisted of atomic step terraces as seen in AFM and sharp streaky RHEED images with a 2× reconstruction along the [100] substrate azimuth, Figure 4.1b and 4.1c, respectively, both attesting to the smooth surface morphology of the film.

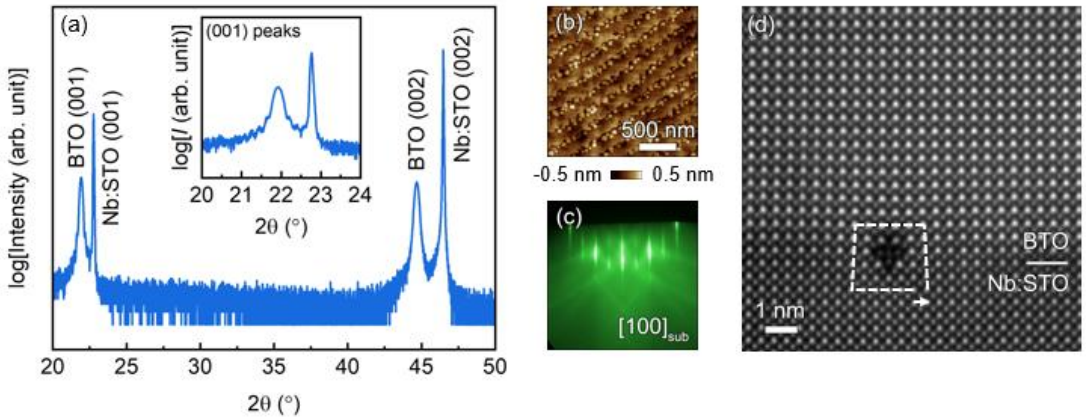

Figure 4.1. (a) HRXRD, (b) AFM, and (c) RHEED of 46 nm BTO/Nb-doped STO (001) (blue) Ti:Ba BEP ratio of 13.7. The inset of (a) shows a zoomed-in look at the (001) peak. (d) Cross-sectional HAADF-STEM image of the film-substrate interface of thicker 240 nm BTO grown on Nb-doped STO (001), viewed along the [100] zone axis. The dashed white line draws the Burgers circuit around a misfit dislocation with the white arrow signifying the Burgers vector **b** = *a*[010].

To take a closer look at these films, cross-sectional HAADF-STEM was performed on a thicker 240 nm BTO film grown on Nb:STO (Figure 4.1d). An atomically abrupt film-substrate interface was found, however with misfit dislocations sporadically distributed along the interface. This observation of misfit dislocations is consistent with relaxing films owing to a large lattice mismatch of -2.2% for BTO film grown on STO. However, the thinner films, e.g. 42 nm shown in Figure 4.1a – 4.1c, showed an expanded out-of-plane

lattice parameter (a_{op}) obtained from HRXRD, 4.058 ± 0.002 Å compared to the bulk value of 4.036 Å, suggesting these thinner films are still strained. While the presence of strain is likely responsible for the expanded a_{op}, it can also be argued to be due to non-stoichiometric related defects. To further investigate the effect of non-stoichiometry and strain relaxation as well as the interplay between the two, two series of samples were grown: (1) with varying Ti:Ba BEP flux ratios, and (2) with varying thicknesses at a fixed Ti:Ba BEP ratio.

4.3 Growth Window

First, the effect of Ti:Ba BEP ratio on films' structure and surface morphology is discussed. Figure 4.2a plots a_{op} vs. Ti:Ba BEP ratio before and after a 1 hour anneal in an oxygen-rich environment at 900°C. The purpose of the anneal was to decrease oxygen vacancies, which are commonly found in MBE-grown BTO films.[195] All films showed a decrease in a_{op} after annealing which is most likely due to the filling of oxygen vacancies and/or further strain relaxation. At a first glance, from the trend in a_{op} vs. Ti:Ba BEP ratio, the MBE growth window, as reported previously for the hybrid MBE of BTO films,[145] is not evident. The increase and then a decrease in a_{op} with increasing Ti:Ba contradicts the previous hybrid MBE report of a constant a_{op} with Ti:Ba for a fully-coherent film on $GdScO_3$. However, the case of BTO grown on STO is more complicated due to the expected strain relaxation from the significant lattice mismatch (-2.2%) as opposed to when grown on $GdScO_3$, which has approximately a -0.5% lattice mismatch.

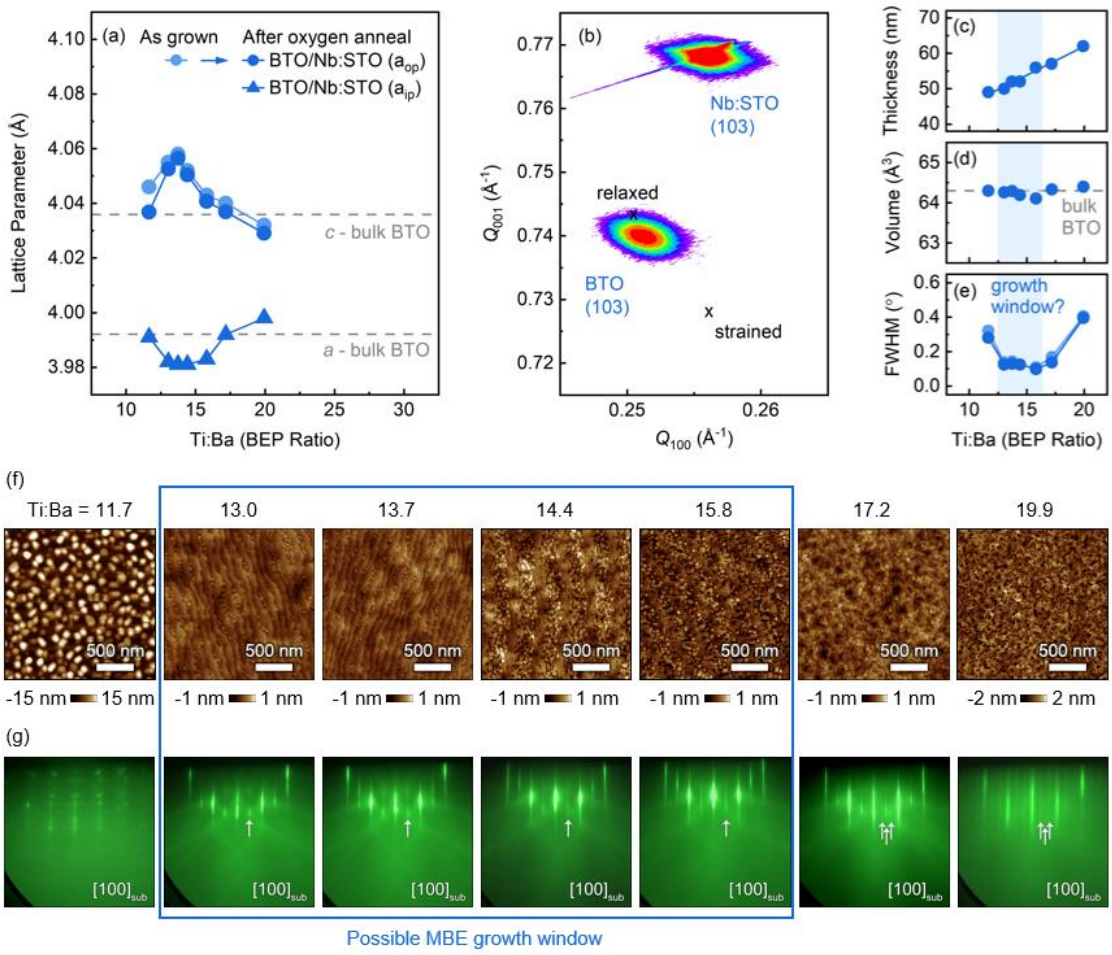

Figure 4.2. (a) Lattice parameters of BTO films grown on Nb:STO before (light color) and after (dark color) oxygen annealing. (b) (103) RSM of BTO film at the peak lattice parameter growth condition Ti:Ba = 13.7. (c) Thickness, (d) unit cell volume, and (e) FWHM of (002) rocking curve. (f) AFM and (g) RHEED images along the substrate [100] azimuth with varying Ti:Ba growth conditions. White arrows mark surface reconstruction streaks.

To this end, RSMs of the films were measured to determine the strain state. Figure 4.2b shows the RSM of a 53 nm film which had the largest a_{op}, grown at Ti:Ba = 13.7, which revealed a mostly, but not completely, relaxed film as evidenced by the film peak being between the expected relaxed and strained positions. It should be noted that the coherently strained in-plane lattice parameters (a_{ip}) of a BTO film on STO substrates refers

to the lattice parameter of cubic STO, 3.905 Å. Whereas the expected coherently strained a_{op}, 4.121 Å, was calculated using the BTO elastic constants C_{11} and C_{33} as shown in Equation (4.1) where ε_{ip} is the in-plane strain applied to BTO from the substrate.[196]

$$a_{op}(coherent) = a_{op}(bulk)\left[1 - \frac{2 \times C_{11} \times \varepsilon_{ip}}{C_{33}}\right] \quad (4.1)$$

The expanded a_{op} of the BTO film grown here can therefore be explained by the residual strain present in the film and the partial relaxation. This observation is further consistent with presence of the misfit dislocations in the STEM image in Figure 4.1d.

Nevertheless, the increasing and then decreasing trend in a_{op} seen in Figure 4.2a does raise questions on the stoichiometry of these films. If an MBE growth window does exist, a range of flux ratios is expected to be seen within which there is adsorption-controlled stoichiometric growth signified by a constant a_{op} for a coherent film. For BTO growth here, this is not seen due to strain relaxation. However, an adsorption-controlled growth regime is expected to occur when using this hybrid MBE technique as demonstrated earlier.[145] It was found, when taking into account not only a_{op} but also a_{ip} obtained from RSMs (Figure 4.3) a nearly constant volume, assuming a tetragonal unit cell, of 64.3 ± 0.1 $Å^3$, the value of bulk BTO. This can be seen in Figure 4.2d throughout the Ti:Ba ratios used here. Along with a constant and low FWHM of the (002) BTO film rocking curves in the center of these growth series, Figure 4.2e, it is possible that an adsorption-controlled window is present but the more complex strain state of BTO/Nb:STO causes the changes seen in a_{op}. At the very least, any non-stoichiometric related defects present within this flux range do not have an effect on the structural quality that can be probed by XRD.

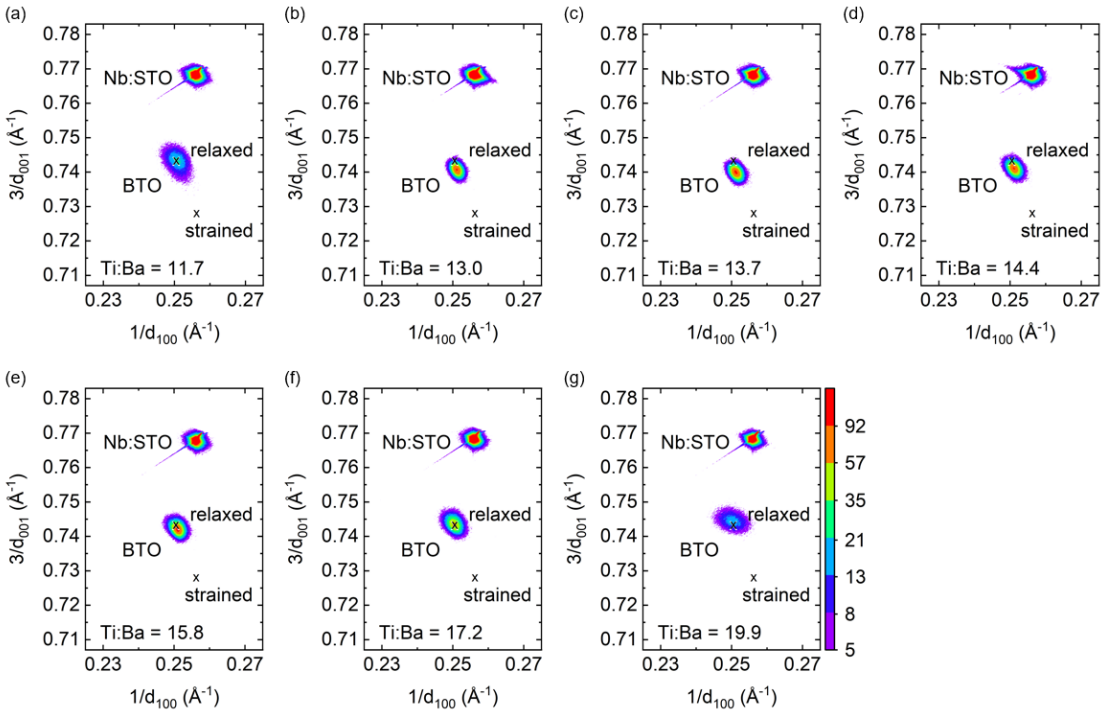

Figure 4.3. (103) RSMs of 49-62 nm BTO films grown on Nb:STO with varying Ti:Ba BEP flux ratios. All intensity ranges are kept the same and shown next to (g). Expected relaxed and coherently strained intensity peak positions are marked with x's.

Consistent with the above observation, films grown within this flux range also showed atomically smooth surface morphology with step edges (Figure 4.2f) along with identical 2× surface reconstruction (Figure 4.2g). Moving to a Ba-rich regime (low Ti:Ba), an island growth mode was seen with spotty RHEED and large island formations in AFM. On the other side, the Ti-rich regime (Ti:Ba ≥ 17.2), a transition away from steps on the surface was seen with the emergence of 3× reconstruction in RHEED. The non-stoichiometry present in the film not only increases bulk structural disorder, as seen by the FWHM, but also the growth mode and surface morphology. The drastic change in surface morphology as moving to the Ba-rich regime is in contrast with the hybrid MBE growth of

$SrTiO_3$. In the case of $SrTiO_3$, moving off stoichiometry towards both the Sr- and Ti-rich regime does not cause such levels of surface roughening, attesting to the difference of depositing with Ba vs Sr in oxide hybrid MBE.

4.4 Thickness and Temperature Dependence

To further check film's cation stoichiometry and probe the strain relaxation, thickness-dependent study on a representative BTO growth condition was performed. Figure 4.4a shows the HRXRD patterns of films, ranging in thickness from 20 to 500 nm, grown at the peak a_{op} growth condition in Figure 4.2a, Ti:Ba BEP = 13.7. As expected, due to strain relaxation, a peak shift to larger 2θ with increasing thickness was observed. The a_{op}, obtained from these peak positions, shows this expected decrease, settling to approximately the bulk lattice parameter at a thickness of 115 nm, as seen in Figure 4.4b.

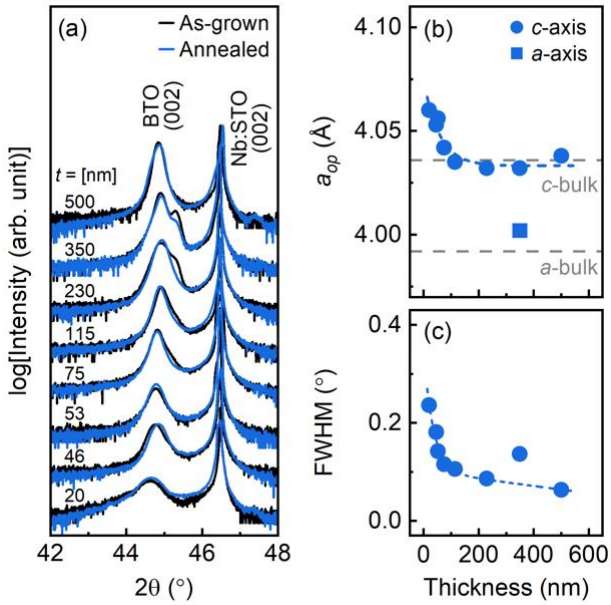

Figure 4.4. (a) HRXRD of 20 to 500 nm BTO samples before and after oxygen annealing, increasing in thickness from bottom to top. (b) Thickness dependent out-of-plane lattice parameter taken from both peaks when present, representing *c*- and *a*-axis domains. (c) FWHM of (002) film rocking curves. All films were grown at the peak lattice parameter growth condition, Ti:Ba = 13.7. Values reported in panels b and c are taken after oxygen annealing.

The lack of strain was confirmed by RSM (Figure 4.5) of the thickest sample, 500 nm BTO on Nb:STO where the film peak aligned with the expected bulk relaxed position. Films also showed a decrease in the (002) film rocking curve FWHM with increasing thickness, Figure 4.4c, suggesting improved crystallinity. Interestingly, after strain relaxation was complete as films were grown to larger thicknesses, both *c*- and *a*-domains emerged. A second peak began to appear in the HRXRD, for all but the thickest 500 nm film, signifying a second domain consistent with *a*-axis of BTO aligned out-of-plane. This agrees well with what has been shown for BTO films, that the absence of biaxial in-plane compressive strain helps form multidomain films, not only the *c*-axis orientation.[197]

Remarkably, however, the post oxygen annealing was found to decrease or even eliminate *a*-domains (depending on the film thicknesses) as evident from the lowering of the peak intensity associated with the *a*-domains (Figure 4.4a).

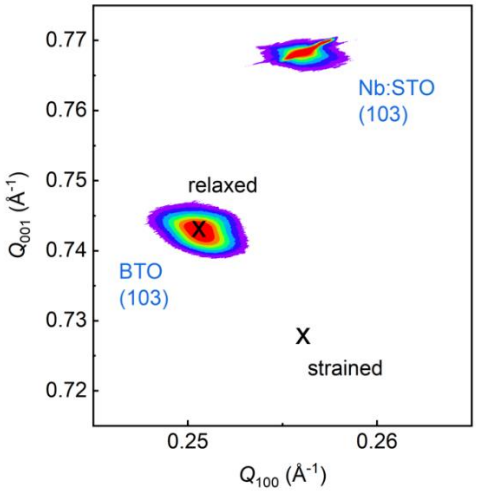

Figure 4.5. (103) RSM of 500 nm BTO film grown on Nb:STO after oxygen annealing showing completely relaxed lattice parameters.

With the growth condition effect on the stoichiometry and strain-state determined, the effect of temperature on the lattice parameters of these films was then studied. Figure 4.6 shows the a_{op} obtained from temperature dependent HRXRD of 50 nm and 350 nm BTO films. Consistent with the first order phase transition in a bulk BTO single crystal, the 350 nm BTO film showed a close to bulk phase transition temperature,[38] with only a slight increase in T_c. On the other hand, the thinner 50 nm film yielded a phase transition with significantly higher T_c (also see Figure 4.7), following the known trend of an increased T_c with increased strain.[67]

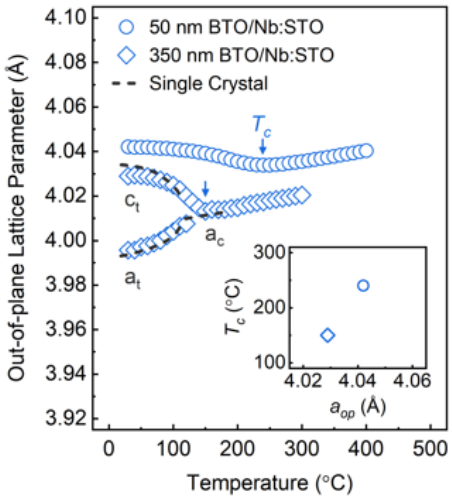

Figure 4.6. (e) Temperature dependent out-of-plane lattice parameters of 50 nm and 350 nm BTO films grown on Nb:STO with Ti:Ba = 13.7. Arrows mark Curie temperatures (T_c). Dashed gray line is bulk single crystal *c*-domain (c_t) and *a*-domain tetragonal (a_t) as well as cubic (a_c) lattice parameters. Inset shows the Curie temperature changing with the out-of-plane lattice parameter.

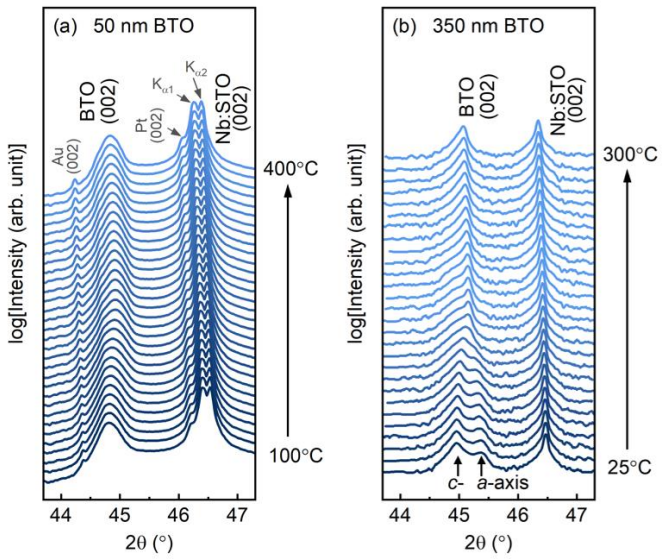

Figure 4.7. Temperature dependent HRXRD patterns of (a) 50 nm BTO film grown on Nb:STO and (b) 350 nm BTO film grown on Nb:STO. Extra peaks are present in (a) due to 1) lack of monochromator and 2) Au and Pt sputtered on the film for future dielectric measurements. All other HRXRD measurements in this report used monochromated X-rays

In summary, single crystalline, epitaxial BTO films were grown on a conducting Nb-doped STO substrate using hybrid MBE. Samples grown within the "MBE growth window" yielded films with a constant lattice volume, low FWHM, and atomically-smooth surface morphologies with an identical 2× reconstruction in RHEED. With increasing film thickness, BTO films begin to relax, reaching to bulk lattice parameters at film thicknesses ≥ 115 nm. A close to bulk phase transition temperature was demonstrated in a 350 nm BTO film on Nb:STO substrate with a slightly increased T_c ~ 150° C. Consistent with prior results, in-plane strain was found to raise T_c. This work shows the influence of stoichiometry and strain relaxation the BTO film structure and surface morphology in addition to establishing hybrid MBE for nominally stoichiometric, epitaxial BTO films on a conducting Nb-doped STO substrate, which is much needed to create all-epitaxial perovskite capacitor structures.

Chapter 5

5. Challenges with $BaTiO_3$ Capacitors

5.1 $BaTiO_3$ Dielectric Measurement

As discussed in the previous chapter, $BaTiO_3$ films were grown on conducting bottom substrates, Nb-doped $SrTiO_3$. By growing on these conducting substrates, dielectric device measurements could be performed after further fabrication to create a complete metal-insulator-metal capacitor. The details of this general fabrication process can be found in Chapter 3.8.

To begin, Figure 5.1 shows the real part of the dielectric constant (ε') and the dielectric loss tangent ($\tan\delta$) for a representative BTO film grown on Nb:STO (001). Across the frequency range measured here, ε' was relatively constant with a value of ~ 300 and $\tan\delta$ remained at a low value of 0.01 in the low frequency range until it began to increase around 10^5 Hz. The increase in $\tan\delta$ could be due to extrinsic effects like inductance, which tends to happen at higher frequencies, or due to the onset of dielectric relaxation which tends to happen above 10^8 Hz for BTO films.[198] Equivalent circuit fitting was performed to determine if an extrinsic effect was playing a role in the dielectric

behavior seen here. The simplest circuit that gave a good fit, which can be seen in the inset of Figure 5.1a, consisted of a contact electrode resistance (R_{el}) in series with a constant phase element (CPE_f) and resistance of the film (R_f), of which the latter two are in parallel with each other. The relation for the impedance of this circuit is then given by

$$Z = R_{el} + \left(\frac{R_f}{1 + R_f Q (j\omega)^{\alpha}} \right) \tag{5.1}$$

From the fitting α = 0.99, close to 1, which means the film is acting as almost an ideal capacitor. Also, as no other extrinsic effects were seen from the fitting, the impedance could be accounted for with just the contact and the film and the increase in tanδ with increasing frequency is most likely from the onset of dielectric relaxation in the BTO film.

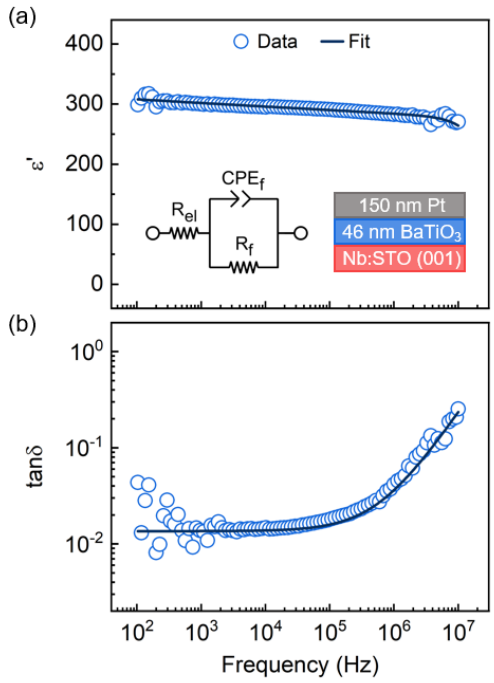

Figure 5.1. (a) Dielectric constant and (b) loss tangent of 46 nm BTO films grown on Nb:STO with Pt top electrode. Dark line is a fit to the inset equivalent circuit.

The value of ε' obtained was ~ 300, which is close to bulk single crystal values of BTO.[199] However, this value was measured for a fairly thin film, 46 nm, and one would expect a smaller than bulk value around these thicknesses due to possible depolarization regions from a dead layer effect. To get a better idea of the "bulk" value of ε' for these hybrid MBE-grown BTO films, studying the effect of film thickness was necessary.

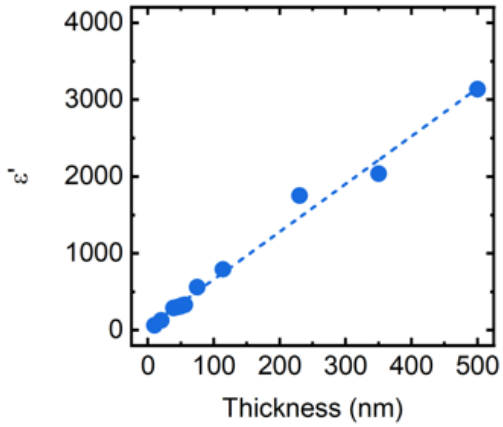

Figure 5.2. Thickness dependence of the dielectric constant of films grown on Nb:STO.

BTO films were grown from 20 nm to 500 nm on Nb:STO, as was discussed in Chapter 4. After device fabrication, impedance spectroscopy was used to determine the dielectric constant as a function of film thickness, plotted in Figure 5.2. As can be seen, ε' linearly increased with increasing thickness. This is not uncommon to see in films and is usually attributed to the dead layer effect. At the interfaces, there can exist these low dielectric constant layers, and their capacitances then add in series with the bulk of the film. Eventually as the film thickness is increased, the effect of these layers should become negligible and the "bulk" value will be reached. Here, this trend is not seen and ε' continues to increase up to 500 nm, the thickest film grown here. It is possible that the ε' will saturate

at even higher film thicknesses, but the value obtained from the impedance is already ~ 3000, an order of magnitude larger than bulk BTO.

5.2 *In-situ* Electrode Growth

Although effects like the dead layer effect are intrinsic to the materials used, the dead layer size can be increased due to defects created at the interfaces as well.[13] To determine if this was the case, to minimize interfacial defects, *in-situ* hybrid MBE-grown La-doped STO films were grown on STO (001) substrates to act as a bottom electrode and BTO films were grown on top. The heterostructure after MBE growth was 100 nm La-doped $SrTiO_3$/20 nm $SrTiO_3$/$SrTiO_3$ (001) (La:STO). The sheet carrier density of La-doped STO was measured as 4.0 x 10^{15} cm^{-2}, compared to 7.5 x 10^{18} cm^{-2} from Nb:STO substrates. The 20 nm of STO prior to La-doped STO was grown to keep the metallic layer separated from the substrate's surface.

Although BTO was grown on structurally the same material, doped STO, differences in the structure of BTO were observed and will be discussed first, before moving to dielectric measurements. To directly compare films grown on Nb:STO (described in Chapter 4) and La:STO, many figures from Chapter 4 will be reproduced with the new data from films on La:STO.

Representative HRXRD scans of BTO films grown on Nb:STO and La:STO are shown in Figure 5.3a. Like those on Nb:STO, films grown on La:STO were single crystalline, epitaxial films consistent with the single domain structure with the tetragonal *c*-axis out-of-plane. However, large differences were found in a_{op}, 4.058 ± 0.002 Å and

4.097 ± 0.002 Å for films on Nb:STO and La:STO, respectively. While the surface of the BTO films on Nb:STO consisted of atomic step terraces as seen in AFM and sharp streaky RHEED images with a 2× reconstruction along the [100] substrate azimuth, (Figure 5.3b and 5.3c), respectively, those on La:STO showed an atomically smooth surface but no steps in AFM (Figure 5.3d) and a RHEED pattern with a 3× reconstruction (Figure 5.3e).

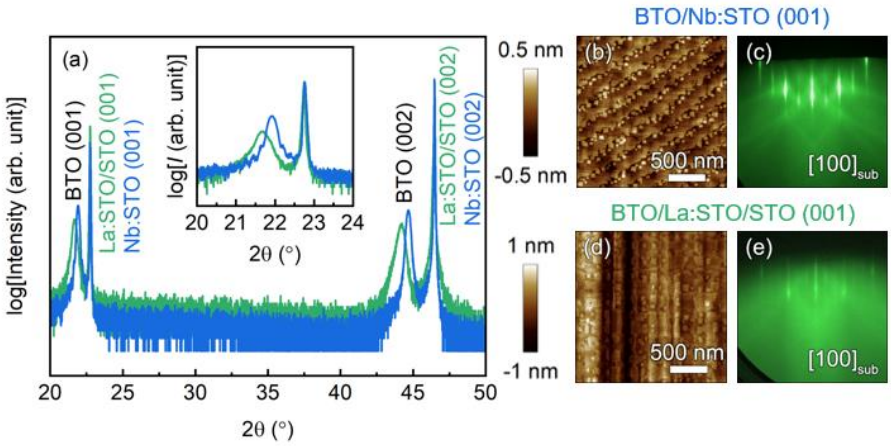

Figure 5.3. (a) HRXRD of 46 nm BTO/Nb-doped STO (001) (blue) and 43 nm BTO/La-doped STO/STO (001) (green) grown at Ti:Ba BEP ratios of 13.7 and 15.2, respectively. The inset shows a zoomed-in look at the (001) peaks. (b) AFM and (c) RHEED of representative 46 nm BTO film grown on Nb:STO. (d) AFM and (e) RHEED of representative 43 nm BTO film grown on La:STO.

The difference in structure can be seen even more clearly based on the dependence on the growth condition, or Ti:Ba flux ratio. Figure 5.4a plots a_{op} for films grown with varying Ti:Ba. Although there were differences in the value of a_{op}, both sets of films showed the same qualitative behavior of an increase and then decrease with increasing Ti:Ba. A shift in the Ti:Ba ratio for the peak a_{op} did occur as well and may be due to differences in the experimental conditions, error in flux measurements, or differences in the growth temperatures arising from the use of different substrates (Nb-doped STO vs

undoped STO). RSMs (Figure 5.4b and 5.4c) were then used to conclude the differences in a_{op} were due to a difference in the strain state. Films grown on La:STO were more strained, even though the lattice mismatch (-2.2%) was the same.

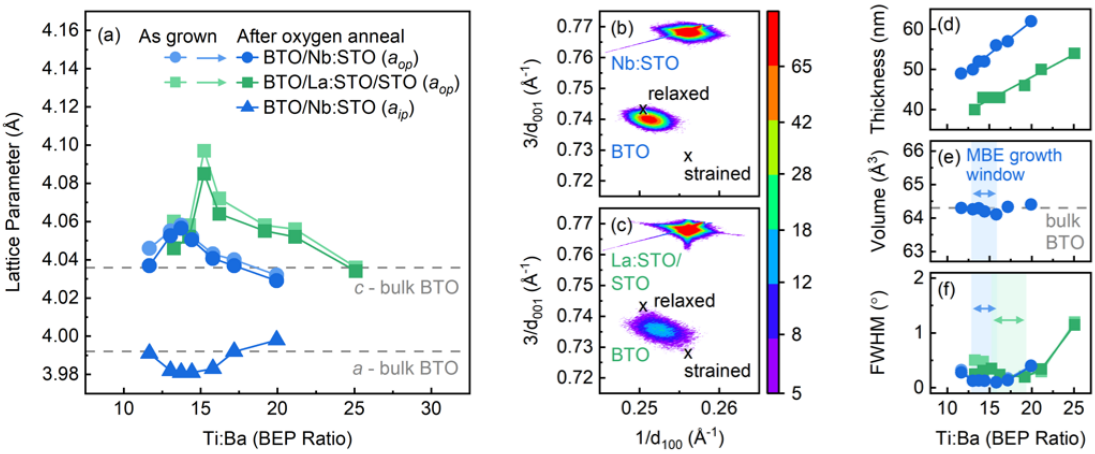

Figure 5.4. (a) Lattice parameters of BTO films grown on Nb:STO (blue) and La:STO (green), before (light color) and after (dark color) oxygen annealing. (013) RSMs of BTO films grown on (b) Nb:STO and (c) La:STO at the peak lattice parameter growth condition, Ti:Ba = 13.7 and 15.2, respectively. (d) Thickness, (e) unit cell volume, and (f) FWHM of (002) rocking curve.

RSMs were not taken for all samples grown on La:STO, so a_{ip}, and therefore unit cell volume, was not determined. However, a similar trend in the FWHM of the film rocking curves was seen (Figure 5.4f), a range of low FWHM with an increase to either side, suggesting the presence of a growth window.

The stabilization of an increased strain-state on La:STO was then confirmed further by growing a series of films with increasing thickness. Even at 400 nm, a_{op} did not relax to the bulk value of BTO (Figure 5.5a), although the FWHM of the film rocking curves decreased in a similar manner (Figure 5.5b). RSM of the thickest film, 400 nm, showed

both a_{op} and a_{ip} falling between the expected fully strained and relaxed positions (Figure 5.5d), while in the 500 nm film on Nb:STO they fell exactly on the expected relaxed position (Figure 5.5c). Finally, with the increased strain state, an increase in T_c occurred, as was expected (Figure 5.5e).

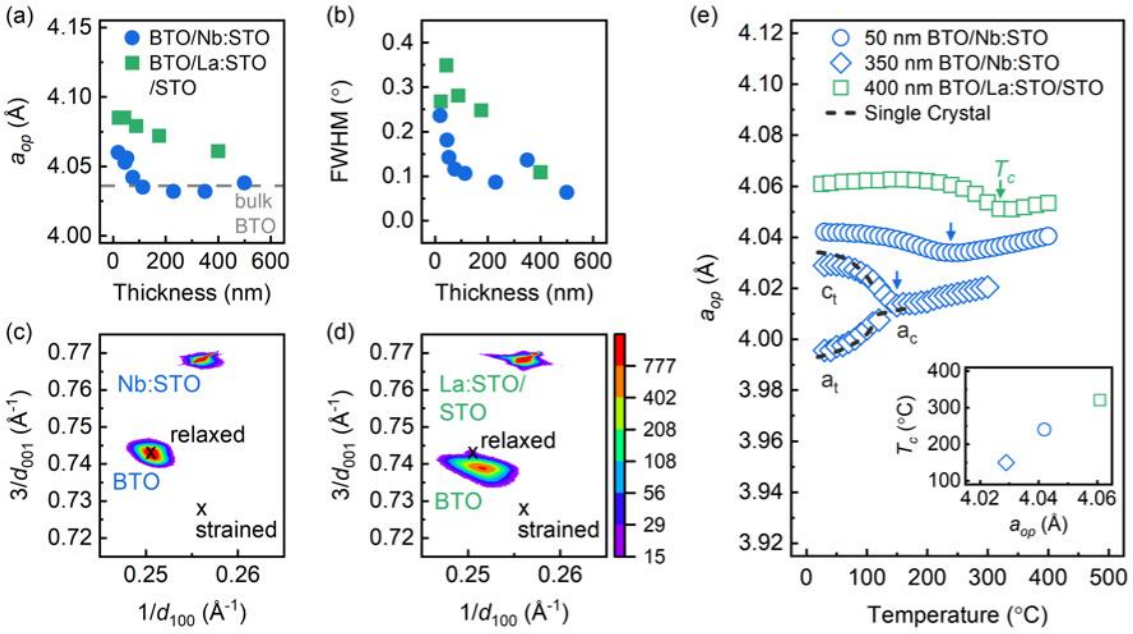

Figure 5.5. Thickness dependent (a) lattice parameter and (b) (002) rocking curve FWHM of BTO films grown on Nb:STO (blue) and La:STO (green) after oxygen annealing. All films were grown at the peak lattice parameter growth condition, Ti:Ba = 13.7 on Nb:STO and 15.2 on La:STO. (013) RSM of (c) 500 nm BTO film on Nb:STO and (d) 400 nm BTO film on La:STO. (e) Temperature dependent out-of-plane lattice parameters of 50 nm and 350 nm BTO films grown on Nb:STO and 400 nm BTO film grown on La:STO. Arrows mark Curie temperatures (T_c). Dashed gray line is bulk single crystal *c*-axis (c_t) and *a*-axis tetragonal (a_t) as well as cubic (a_c) lattice parameters. Inset shows the Curie temperature changing with the out-of-plane lattice parameter.

The question remains as to why BTO films grown on La:STO undergo less strain relaxation than those on Nb:STO despite identical growth conditions and same lattice mismatch with the underlying layers. Based on the previous and following results, the

difference is attributed to the electrical boundary condition. Although the measured room-temperature resistivities of Nb:STO substrates (6 mΩ·cm) and La:STO films (2 mΩ·cm) were similar (within a factor of 3), they had significantly different sheet carrier densities (n_{2D}), 7.5 x 10^{18} cm^{-2} and 4.0 x 10^{15} cm^{-2}, respectively, owing to their different thicknesses. The electrical boundary condition has been shown to affect domain formation in ferroelectric thin films by changing the depolarization field present in the ferroelectric film.[71,200] This could potentially influence the strain relaxation process and therefore a_{op}.

To test this hypothesis, two ~ 40 nm BTO films were grown on a conducting and an insulating STO layer. A Ti:Ba BEP ratio of 14.2 was used. As illustrated in Figure 5.6a and 5.6b, both substrate and the buffer layer were kept identical with the only difference being the conducting vs insulating surface. The conducting layer was obtained by doping the top 25 nm of STO with La dopant. Consistent with the results above for BTO films grown on a highly conducting Nb:STO (n_{2D} = 7.5 x 10^{18} cm^{-2}) substrate vs. on a less conducting La:STO (n_{2D} = 4.0 x 10^{15} cm^{-2}) substrate, the controlled films grown on an insulating surface (i.e., no carriers) yielded a much larger a_{op} (4.102 ± 0.002 Å) as compared to films (4.058 ± 0.002 Å) grown on a conducting surface (Figure 5.6e). Accompanied by the change in lattice parameters, a drastic change in surface morphology was also seen, suggesting growth modes may also be affected by the electrical boundary condition.

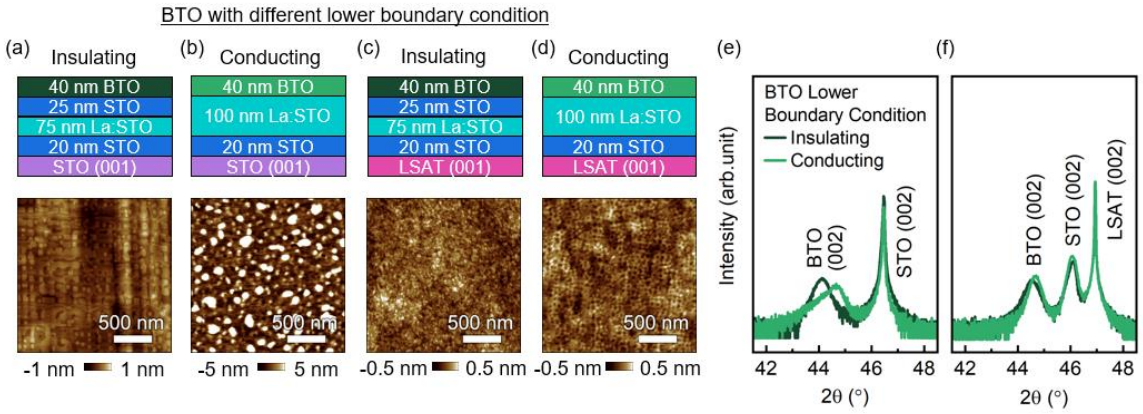

Figure 5.6. (a-d) Film heterostructures and AFM images of BTO films with insulating and conducting bottom boundary conditions on STO (001) and LSAT (001) with Ti:Ba = 14.2. HRXRD of insulating interface BTO/STO (dark green) and conducting interface BTO/La:STO (green) film heterostructures grown on (e) STO (001) and (f) LSAT (001).

It is conceivable that the mechanical boundary condition may also interfere with the electrical boundary condition during ferroelectric film growth. Therefore, to study the interplay between the electrical and mechanical boundary conditions, BTO films were also grown on conducting and insulating STO which was strained to match $(LaAlO_3)_{0.3}(Sr_2TaAlO_6)_{0.7}$ (LSAT) (001) substrates. When grown coherently on LSAT,[201] STO matches the in-plane lattice parameter of LSAT, 3.868 Å, thereby increasing the lattice mismatch with BTO from -2.2% (with STO substrate) to -3.1% (with STO/LSAT substrate). Shown in Figure 5.6c and 5.6d, increasing the lattice mismatch causes less of a difference in the surface morphology of BTO when grown on the two contrasting electrical boundary conditions. The magnitude of the shift in a_{op} also decreases, as seen by the reduced peak shift in HRXRD (Figure 5.6f). These results suggest that although growing on an insulating layer can drastically change the microstructure, and a_{op} in the case of BTO on STO, this effect can be negated by a change in the mechanical boundary condition as

seen on STO/LSAT. It is also noted that in addition to the electrical and mechanical boundary conditions, surface roughness of the underlying layer may play an important role in the strain relaxation process, the effect of which is minimized by growing underlying STO layers via MBE as opposed to using STO substrate as an active interface.

5.3 Measurement of *In-situ* Electrode Device

Keeping in mind the differences in structure of the BTO films based on their bottom electrode, and following the complete device fabrication, impedance spectroscopy was used once again to determine ε' for a range of thicknesses, 22 nm to 400 nm. The results are shown in Figure 5.7a. At first, it did appear the problem was solved and ε' was beginning to saturate as film thickness was increased. However, when looking at the Nyquist plots, Figure 5.7b, an additional component, a semicircle, is present at high frequencies but was not for films grown on Nb:STO. Nyquist plots are a useful way of quickly determining if the MIM device behavior is like a capacitor (straight vertical line), a resistor (straight horizontal line), or a mixture of the two (semicircle). The origin of this additional component is unknown (some extrinsic effect, most likely) but can be removed by equivalent circuit fitting to determine the true value of ε' for the film. The equivalent circuit used can be seen in Figure 5.7c, for both films grown on Nb:STO and La:STO. Satisfactory fits could only be obtained with the addition of an extrinsic capacitive (CPE_e) and extrinsic resistive element (R_e), in parallel, for films grown on La:STO. From these fits, the actual film ε' could be determined from the capacitive component for the individual films (CPE_f) and the results showed that both sets of films had the same linearly increasing

ε' as a function of thickness, Figure 5.7d. Growing films on an *in-situ* grown bottom electrode did not solve the problem of the lack of bulk ε' saturation.

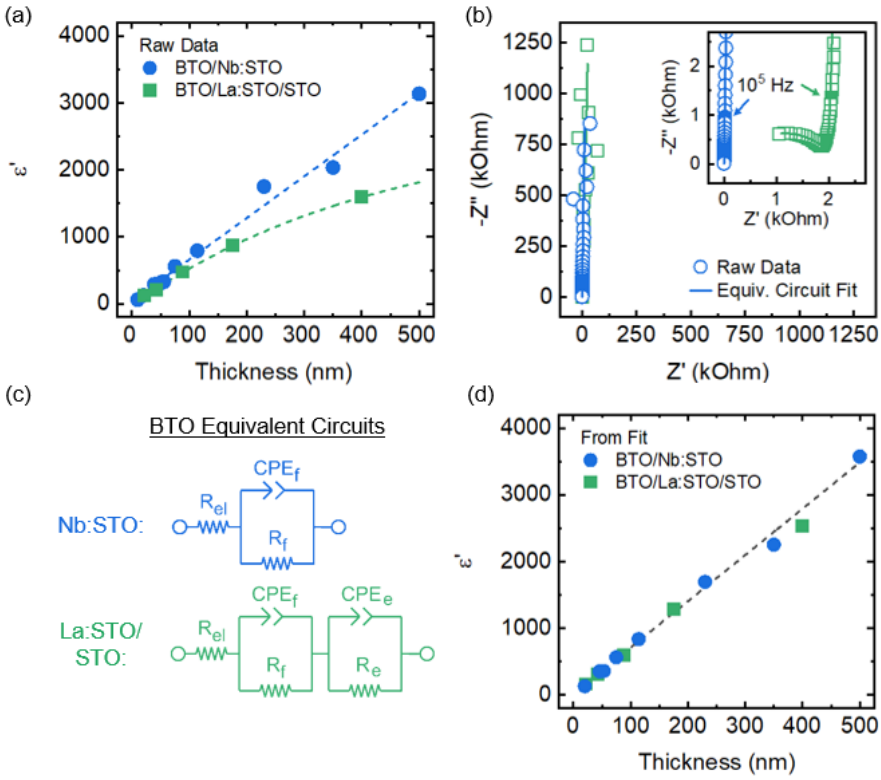

Figure 5.7. (a) Thickness dependence of the dielectric constant of films grown on Nb:STO and La:STO. (b) Nyquist plot, imaginary vs real part of impedance, for ~ 45 nm BTO films on both Nb:STO and La:STO. Inset shows high frequency, low impedance values. Solid lines are fits to the respective equivalent circuits, shown in (c). (d) Thickness dependence of the dielectric constant taken from only the film component (CPE_f) obtained from the equivalent circuit fitting.

5.4 Device Fabrication Routes

The other interface could be the source of the parasitic interfacial capacitance that is dominating the impedance measurements. To study the effect of the top electrode, three different routes of fabrication were done with the goal of removing possible extrinsic

defects between the BTO films and Pt top electrodes. This top interface is exposed to atmosphere when removed from the MBE system.

Figure 5.8 outlines the three fabrication flows used here to determine if there is any impact on the dielectric properties. Sample A was fabricated with the typical route used in the previous section and in the next chapter. It involves a blanket sputter deposition of Pt, an ion mill etch, an oxygen anneal, and a bottom contact sputter deposition, as is described in more detail is Chapter 3.8. Sample B makes a slight change by introducing an additional oxygen anneal directly after growth with the idea that the Pt top layer my impede oxygen diffusion, thereby not decreasing oxygen vacancy concentrations near the top interface. Sample C only does the oxygen anneal after growth, not after etching.

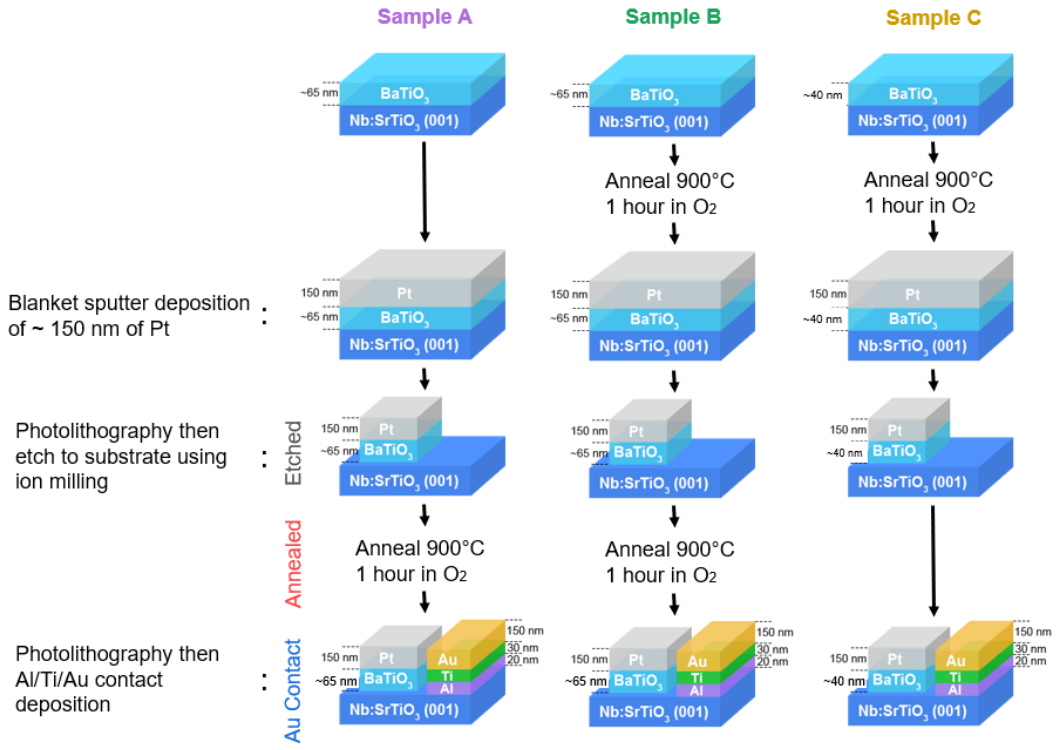

Figure 5.8. Schematic pathways for device fabrication of three BTO samples grown on Nb-doped STO(001) substrates.

Figure 5.9 plots the Nyquist plots for these three samples. Sample A and Sample B exhibit close to ideal capacitor behavior while, as can be seen more clearly in the inset, Sample C does not. It becomes clear that the oxygen anneal is needed after ion mill etching, otherwise a non-negligible conductivity is introduced in the BTO film and the semicircle behavior is seen in the Nyquist plot.

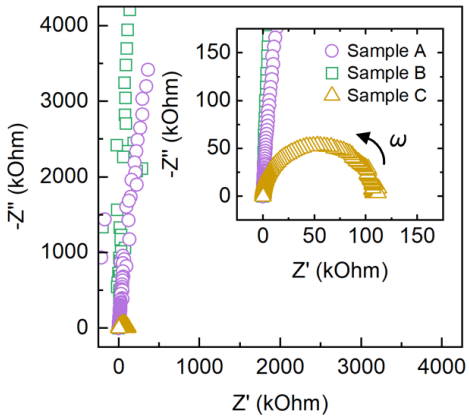

Figure 5.9. Nyquist plot for Sample A, B, and C. Inset shows zoomed in plot at low real and imaginary impedance.

Comparing Sample A and Sample B allows for the determination of if an initial oxygen anneal is needed following the growth. Figure 5.10 compares ε' and $\tan\delta$ along the fabrication process for both samples. Impedance spectroscopy measurements were taken following the etch, the final anneal (which is the only anneal for Sample A), and the Al/Ti/Au bottom contact deposition. Neither sample showed reproducible or very discernable dielectric signal prior to the bottom contact deposition because it is difficult to

make Ohmic contact with probes directly to Nb:STO. Sample B, however, did show a low frequency static dielectric constant after the final anneal, but this signal quickly relaxed to zero. It was only after the complete fabrication that the expected dielectric behavior was seen for both samples, a relatively constant ε' and tanδ throughout the frequency range. Comparing the two, only slight differences were seen. Sample A show more of an increase in ε' at low frequency which is most likely from space charge effects. It appears the lack of an initial oxygen anneal can cause incomplete oxygen vacancy filling, which is the usual source of these space charge effects. For tanδ, slightly larger values were also obtained for Sample A without the first oxygen anneal. Although a slight increase in the dielectric properties was found in Sample B compared to Sample A, this change was not drastic enough to be the source of the increasing ε' with film thickness in the previous section.

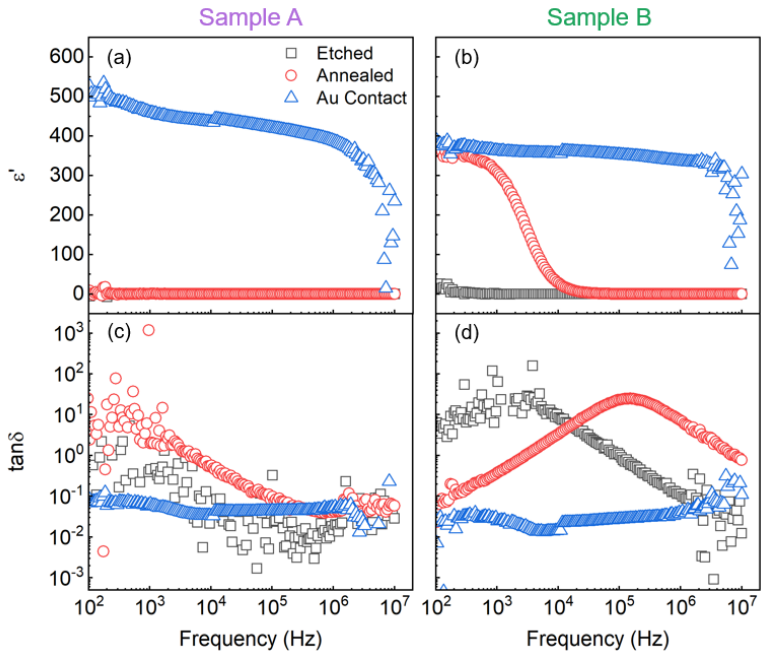

Figure 5.10. Dielectric constant (ε') and loss tangent (tanδ) vs frequency for (a) and (c) Sample A and (b) and (d) Sample B, respectively. The discontinuity in the data around 10^4 Hz is an artifact from the measurement.

5.5 Outlook

It has become clear that doped STO does not make a suitable electrode for BTO as grown here. This is most likely some intrinsic effect similar to a dead layer effect between the two, with an interfacial capacitance that is dominating the dielectric measurement. In fact, even growing a completely *in-situ* grown capacitor with doped STO bottom and top electrodes did not change the results. Also, the band alignment of BTO and STO is not ideal, Figure 5.11a, and films will most likely be leaky, as they were here, even if this interfacial effect was not present. Because of this leakage, no ferroelectric polarization-electric field (P-E) loops could be obtained for any sample. The exact reason for the undesirable BTO-Nb:STO interface will be the focus of future work.

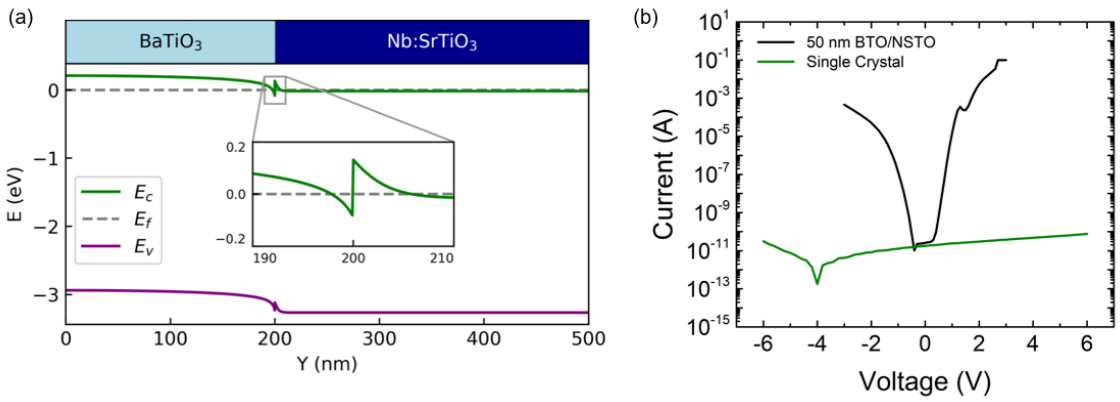

Figure 5.11. (a) Simulated band alignment of BTO and Nb:STO. (a) Current vs voltage for a 50 nm BTO film grown on Nb:STO compared to a single crystal.

However, another solution for obtaining a proper dielectric measurement is to use a different electrode. As mentioned in the introduction, certain materials are better suited for decreasing the dead layer effect when creating ferroelectric devices. The two most

popular choices are Pt and $SrRuO_3$. Pt has the superior electrostatic screening length, can be grown epitaxially on STO, and, when done so, is closely lattice matched with BTO. $SrRuO_3$, on the other hand, also has good electrostatic screening due to a high ionic polarizability, has the same perovskite crystal symmetry as BTO, can be used for an all-oxide device, and is also closely lattice matched. Developing new synthesis techniques for the MBE growth of these electrodes, and therefore completely *in-situ*-grown capacitors, will be the focus of Chapter 8 and 9.

Chapter 6

6. Dielectric Response in $BaSnO_3$ films

The dielectric response of epitaxial $BaSnO_3$ films grown on Nb-doped $SrTiO_3$ (001) substrates using a hybrid molecular beam epitaxy approach was studied. Metal-insulator-metal capacitors were fabricated to obtain frequency- and temperature-dependent dielectric constant and loss. The dead layer effect did not play as large of a role as in the case of $BaTiO_3$ due to the order of magnitude smaller dielectric constant. Irrespective of film thickness, cation stoichiometry, and dislocation density, the dielectric constant obtained from $Ba_{1-x}Sn_{1-y}O_3$ films remained largely unchanged at 15-17 and were independent of frequency and temperature. A loss tangent of $\sim 1 \times 10^{-3}$ at 1 kHz < f < 100 kHz was obtained for stoichiometric films, which increased significantly with non-stoichiometry. Using density functional theory calculations, these results are discussed in the context of point defect complexes that can form during film synthesis.

This chapter was adapted from: William Nunn, Abhinav Prakash, Arghya Bhowmik, Ryan Haislmaier, Jin Yue, Juan Maria Garcia Lastra, and Bharat Jalan. Frequency-and temperature-dependent dielectric response in hybrid molecular beam epitaxy-grown $BaSnO_3$ films. *APL Mater.* **6**, 066107 (2018).

6.1 Introduction

$BaSnO_3$ (BSO) is a wide bandgap perovskite oxide, which has recently gained considerable attention due to the discovery of a large room temperature mobility.[108,151,157,158,202-206] When doped with La, BSO has been shown to have a mobility of 320 $cm^2 V^{-1} s^{-1}$ in bulk[203-205] and up to 183 $cm^2 V^{-1} s^{-1}$ in thin films at remarkably high carrier densities of the order of 10^{20} cm^{-3}.[108] The combination of high carrier density and mobility makes doped BSO a promising candidate for transparent conducting oxides and power electronic applications.[207-209] Both electronic and optical properties of BSO can be strongly affected by their dielectric behavior. However, despite the increasing amount of work on the electronic and optical properties of BSO, there have been no reports on the dielectric response of BSO in thin film form. A few reports of dielectric properties exist and are measured using polycrystalline bulk samples.[210-213] For example, a dielectric constant of about 20 is reported for bulk BSO ceramics synthesized using solid state ceramic method.[210] Most recent work reported a value of 45 using powder BSO samples.[213] Theoretical calculations have also been carried out and have predicted a value of 22, which is in good agreement with the experimental bulk value.[213]

Thin film geometry can offer additional advantages of tailoring dielectric constant through strain engineering approaches. However, it also yields several challenges associated with point defect control and strain relaxation-induced dislocation formation. The latter becomes a more severe problem for films that have large lattice mismatch with substrates, as is commonly the case with BSO.[108,127,149,157,214] A large density of threading dislocations, 10^{11}-10^{12} cm^{-2}, is nominally found in BSO films grown on various substrates

including STO (001).[108,214,215] These dislocations are argued to be charged centers[109,151,204] and, present in significant concentrations, can arguably influence polarization and thereby dielectric constant of BSO in thin film geometry. Additionally, factors such as film/electrode interfaces can influence dielectric constant of BSO films. For instance, thickness dependent dielectric constants have been commonly observed in ferroelectric systems including (Ba,Sr)TiO_3 system owing to an interfacial "dead layer" effect.[216-219] It is, however, also argued that dead layer effect may not be observable in films having a low dielectric constant.[220]

Here, the dielectric constant (ε') and the dielectric loss tangent (tanδ) of nominally stoichiometric BSO films are studied as a function of film thickness, frequency, and temperature between 77–300 K. Films grown under Ba- and Sn-deficient conditions are also examined to investigate the role of cation stoichiometry on dielectric responses. These results are then discussed using density functional theory (DFT) calculations revealing important role of Ba, Sn, and O vacancies and related defect complexes on dielectric constant of BSO.

6.2 Growth, Fabrication, and Characterization

BSO films were grown on conducting 0.5 wt% Nb-doped $SrTiO_3$ (001) substrates using the hybrid MBE approach described in Chapter 3 and in more detail elsewhere.[109,149,151] Stoichiometry was tailored by controlling Sn:Ba beam equivalent pressures ratios.[151] The degree of non-stoichiometry was estimated by correlating Sn:Ba BEPs and the BSO out-of-plane lattice parameters with the Rutherford Backscattering

spectrometry results for BSO films grown on $SrTiO_3$.[151] The MIM capacitor structures, as illustrated schematically in the inset of Figure 6.1, were fabricated for dielectric measurements as described in Chapter 3.8. It is noted that as-grown BSO films were insulating suggesting no measurable oxygen vacancy defects, however, films were still annealed at 900°C for 1 hour in excess of oxygen to decrease possible contributions from oxygen vacancies that may be introduced during the ion milling process.

HRXRD coupled 2θ-ω scans were taken on a Panalytical X'Pert thin film diffractometer. Complex impedances were measured using an Agilent B1500A from 1 kHz - 1 MHz with a peak oscillating electric field of about 20 kV/cm. A Lakeshore CPX-VF cryogenic probe station was used to perform temperature-dependent impedance measurements from 77-300 K. A variety of defect states within a 2×2×2 supercell were studied using DFT based simulations for formation energy and dielectric properties.

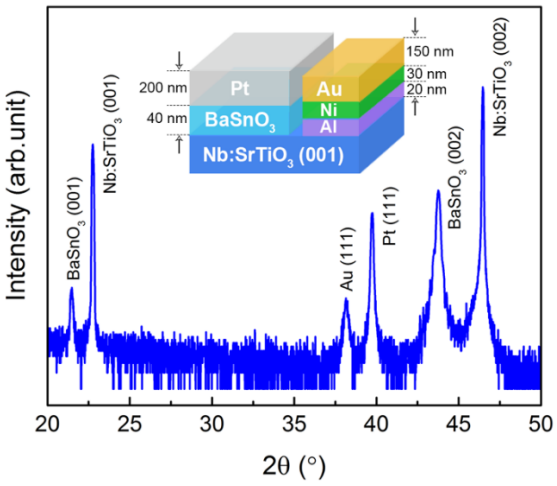

Figure 6.1: HRXRD pattern for a 40 nm BSO film on Nb-doped $SrTiO_3$ (001) substrate after complete capacitor fabrication. Inset shows a schematic of the device structure.

Figure 6.1 shows the HRXRD pattern of the film stack in a MIM capacitor configuration consisting of 40 nm stoichiometric BSO/Nb:STO (001) and metal electrodes after complete processing. A schematic of the capacitor structure is shown in the inset. The HRXRD result shows phase-pure, epitaxial, single crystalline BSO films on Nb:STO (001). Additional peaks corresponding to Pt (111) and Au (111) were also present indicating crystalline and epitaxial (in *Z*-direction) metal electrodes. It is noted that cation stoichiometry for BSO films were confirmed using adsorption-controlled growth regime offered by the hybrid MBE approach.[151]

6.3 Effect of Stoichiometry

Figure 6.2a and 6.2b show the frequency (*f*) dependence of ε' and tanδ, respectively, for films with different compositions. Film thicknesses were kept between 40-49 nm. Fits in Figure 6.2b for tanδ as a function of *f* were calculated from complex impedance fits using the equivalent circuit shown as an inset. Best fits were found using a constant phase element (CPE_f) for the film, which may act as an imperfect capacitor. The overall impedance (*Z*) of the circuit is therefore given by

$$Z = R_{el} + \left(\frac{R_f}{1 + R_f Q(j\omega)^{\alpha}}\right) + j\omega L \qquad (6.1)$$

where R_{el} and R_f are the electrode and film resistance, respectively; $\omega = 2\pi f$, Q is a frequency independent constant, and L is the inductance of the equivalent circuit. α is a parameter between 0 and 1 which gives the constant phase of $-(90\alpha)°$, where $\alpha = 1$ is a perfect capacitor and $\alpha = 0$ is a pure resistor. Regardless of stoichiometry, excellent fits were obtained using this circuit and yielded $\alpha = 0.998$-0.999, further confirming nearly

perfect capacitor behavior. An inductance of 5.5 μH was also found from the fit, which is in good agreement with perovskite thin film capacitors and has usually been attributed to the electrode behavior.[221] The frequency dependent value of ε' remained largely unchanged for all samples (see Figure 6.2a). A value of 14.8 ± 0.5 was measured for stoichiometric (Sn:Ba = 1.00 ± 0.02), and Ba-deficient (1.15 ± 0.02) films whereas a slightly higher value, 15.6 ± 0.5, was obtained for Sn-deficient film (0.95 ± 0.02). Stoichiometric films however yielded much lower tanδ, $1.6\times10^{-3} \pm 1\times10^{-4}$ in 1 kHz < *f* < 100 kHz, whereas much higher tanδ was obtained for non-stoichiometric films. Irrespective of cation stoichiometry, all three samples showed an increase in tanδ for *f* > 100 kHz, suggesting an onset of dielectric relaxation. A larger frequency range would be needed to confirm dielectric relaxation processes in BSO films.

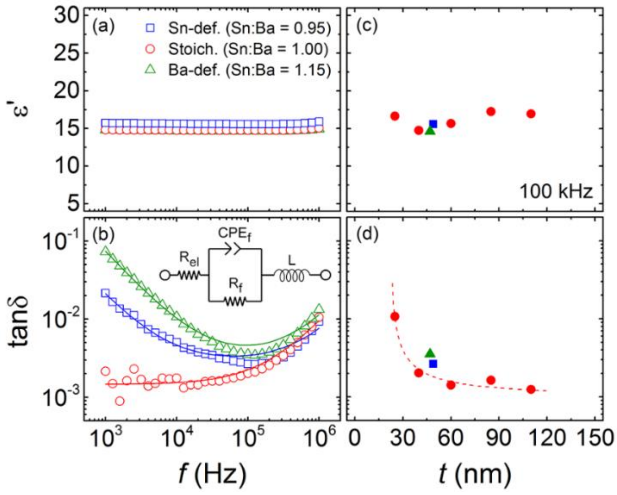

Figure 6.2: Frequency dependence of (a) ε' and (b) tanδ for stoichiometric (40 nm), Sn-deficient (49 nm), and Ba-deficient (47 nm) BSO films. Error to the RBS composition is ±0.02. Solid lines are fits using the schematic equivalent circuit as illustrated in the inset incorporating electrode (R_{el}) and film (R_f) resistance, film capacitance in terms of a constant phase element (CPE_f), and inductance (L). Film thickness dependence of (c) ε' and (d) tanδ for stoichiometric and Ba- and Sn-deficient films measured at 100 kHz. Dashed line is a guide to the eye. Error bars are of the size of symbols.

The experimental results for thin BSO films have about a 25% lower dielectric constant than the reported bulk value of 20 in ceramic samples, and these values are independent of cation stoichiometry. These findings raised questions on the possible roles of dimensionality, threading dislocations, and interfaces that may degrade a film's dielectric performance. To this end, a thickness series of nominally stoichiometric BSO films were grown to determine how dielectric properties evolve with film thickness (*t*). Figure 6.2c and 6.2d shows ε' and tanδ, respectively, measured at f = 100 kHz for stoichiometric films (red circle symbol). Results of Ba-deficient (green triangle symbol) and Sn-deficient (blue square symbol) samples are also shown on the same plots for comparison. ε' was found to be relatively constant, whereas tanδ decreased hyperbolically with increasing film thickness to a value ~1×10^{-3}. A similar behavior of tanδ vs f was seen by Li *et al.*[222] for $SrTiO_3$ films and was attributed to the interfacial "dead layer" effect. However, it is noteworthy that there was no change in ε' vs t as one may expect from a dead layer. This behavior is attributed to the low dielectric constant of BSO.[220] Another factor that may influence the dielectric loss is threading dislocation density in BSO films. In prior work, it has been shown that threading dislocation density decreases with increasing thicknesses resulting in an increase of electron mobility.[151] It is thus also conceivable to attribute the observed behavior of tanδ vs f to the threading dislocations. Future theoretical work should be directed to investigate role of dielectric dead layer and threading dislocations on dielectric loss.

6.4 Temperature Dependence

Finally, the temperature dependence of dielectric constant and loss was investigated. Figure 6.3a and 6.3b show T-dependent ε' and tanδ, respectively, measured at 100 kHz from 77-300 K for films with different cation stoichiometry. No change in ε' was observed in this temperature range, but tanδ showed significant variation with temperature. With decreasing temperature, tanδ first increased for the stoichiometric sample followed by a broad peak around 100-175 K. A similar broad peak was observed for Ba-deficient films but tanδ initially decreased with decreasing temperature. Sn-deficient films, on the other hand, showed a drop in tanδ with decreasing temperature reaching below that of stoichiometric film, and no obvious broad peak. While it is yet to be established the main source of peak in tanδ, it may be attributed to extrinsic defects[223] including threading dislocations, residual oxygen vacancies[224], or phase transition in the Nb:STO substrate. Intrinsic factors such as Debye dielectric loss can also result in a peak in tanδ with temperature, but this behavior is usually operative at much higher frequencies.

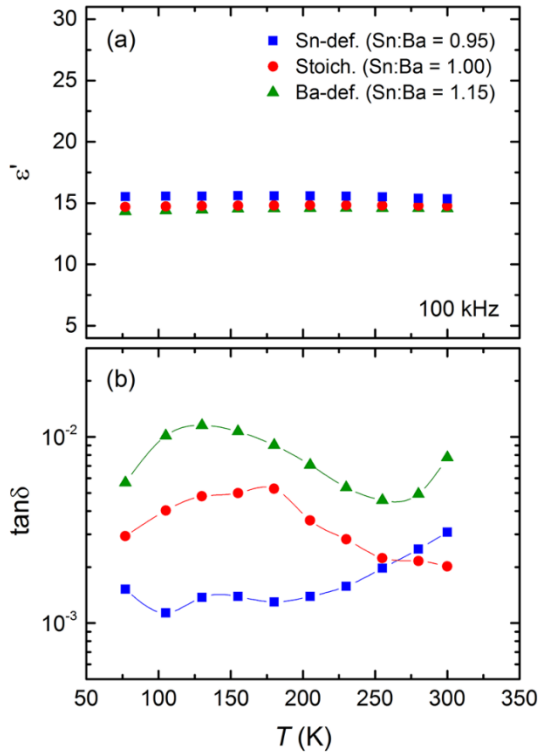

Figure 6.3: Temperature dependence of (a) ε' and (b) tanδ measured at 100 kHz for stoichiometric (40 nm), Sn-deficient (49 nm), and Ba-deficient (47 nm) BSO films. Error to the RBS composition is ±0.02 and error bars are of the size of symbols.

6.5 Defect Simulation

To investigate an apparent tolerance of the dielectric constant to cation stoichiometry, DFT simulations were used. The calculated dielectric constant for bulk, defect-free BSO was 18.1 comprising of electronic and ionic contributions of 4.7 and 13.4, respectively. The calculated electronic contribution agrees well with previous theoretical work by Bévillon *et al.*,[213] whereas the ionic contribution is smaller. The discrepancy arises from the difference in phonon frequency estimates, although Born charges (Z^*_{xx} of +2.76/+.37/-3.34 for Ba/Sn/O ions) match with reported values.[213] To simulate defect

structures in non-stoichiometric films, a subset of possible defects configurations including cation and oxygen vacancies and their defect complexes were considered. DFT yielded formation energies of +0.71 eV for $\ddot{V}_o$ and +6.22 eV and +10.66 eV for V''_{Ba} and V''''_{Sn}, respectively. A possible defect complex in Sn-deficient samples consisting of one V''''_{Sn}, and two $\ddot{V}_o$ in the 40 atom supercell showed a total vacancy formation energy of +3.88 eV when these vacancies are next to each other, i.e., $\ddot{V}_o$-V''''_{Sn}-$\ddot{V}_o$ angle is 90°. Likewise, for a Ba-deficient sample, a defect complex consisting of one V''_{Ba} and one $\ddot{V}_o$ vacancy requires much lower formation energy, +3.67 eV, when there is a missing O atom in second coordination, 5.03 Å from missing the Ba atom. For different supercell configurations with these vacancy complexes, DFT calculation revealed small changes in the Born charge of ions and very small reduction in the ionic contribution to the dielectric constant. Similarly, the electronic contribution to the dielectric constant remained largely unchanged, except in the supercell with only an O vacancy, where it increases to 6.84 as compared to 4.74 in defect-free BSO. Furthermore, DFT calculations revealed anomalous Born charge on some O atoms (Z^*_{xx} of -5.5), Sn atoms (Z^*_{xx} of +5.73) and Ba atoms (Z^*_{xx} of +3.37) in a supercell with only an O vacancy, leading to substantial ionic contribution to dielectric response (50.5) and the total dielectric constant (57.4).

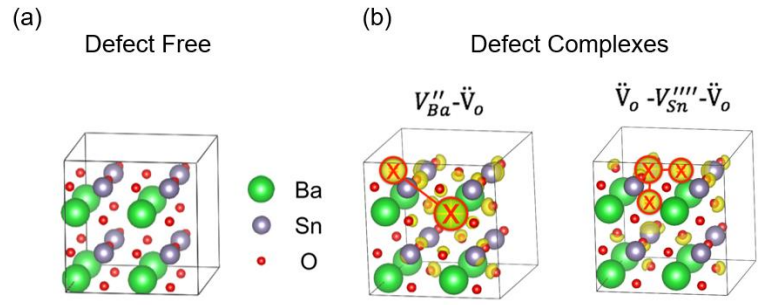

(c)

Defect/ Defect Complexes	$\ddot{V}_o$	V''_{Ba}-$\ddot{V}_o$	$\ddot{V}_o$ -V''''_{Sn}-$\ddot{V}_o$	V''_{Ba}	V''''_{Sn}
Formation Energy	+0.71 eV	+3.67eV	+3.88 eV	+6.22 eV	+10.66 eV

Figure 6.4. (a) Atomic configuration of defect-free 2×2×2 BSO supercell. (b) Atomic configuration showing probably defect complex formation when Ba-deficient (Ba and O vacancy) and Sn-deficient (Sn and double O vacancy). (c) Table of formation energies from DFT simulations for single defects and defect complexes.

In summary, the dielectric properties of BSO films grown by hybrid MBE were characterized. The measured dielectric constant was 15 for stoichiometric films and remained largely unchanged with stoichiometry, film thickness, frequency, and temperature. Stoichiometric films yielded the lowest tanδ, 1×10^{-3} at room temperature, but exhibited a broad peak between 100-175 K. DFT simulations were used to investigate the effect of possible point defects/defect complexes on the dielectric constant and was found to be consistent with the experimental results. Future theoretical work should however be directed to investigate the specific contribution of different defects on dielectric loss behavior.

Chapter 7

7. $BaTiO_3$ – $BaSnO_3$ Alloy System

Ferroelectric materials with large polarizations and piezoelectric responses have been increasingly sought after for use in a variety of devices such as capacitors and micro-electromechanical systems (MEMS) devices like certain sensors and actuators.[225-227] Of these, unfortunately, most leading ferroelectrics contain the toxic element lead, as was described in more detail in the introduction. The $BaTiO_3$-$BaSnO_3$ alloy system, or $BaTi_{1-x}Sn_xO_3$, has been looked at as a replacement for lead-based ferroelectrics like lead-zirconate-titanate due to the enhanced ferroelectric and piezoelectric responses at around $x = 0.11$, where a quasi-quadruple point and morphotropic phase boundaries exist.

This chapter was adapted from a yet to be published work: William Nunn, Abinash Kumar, Shukai Yu, Venkatraman Gopalan, James LeBeau, and Bharat Jalan. Thin Film Growth of Sn-modified $BaTiO_3$ with Enhanced Polarization (2021).

Although most studies on BTSO have been done in ceramics, a few reports of thin film growth do exist. These include by sol-gel methods,[228,229] sputtering,[230-233] and PLD.[234,235] Determining if the giant increase in the ferroelectric response can be transferred to film growth has yet to be determined. Growing materials low in defects and with great control over the composition will be key for achieving these properties and understanding this system in films. Molecular beam epitaxy excels at this and, here, for the first time, will be used for the complete BTSO system growth, from $BaTiO_3$ (BTO, x = 0) to $BaSnO_3$ (BSO, x = 1). The hybrid MBE technique is used, which has already been shown in this thesis work to be capable of growing the two end members in a high-quality manner.

7.1 Composition Control

BTSO films were grown on undoped STO substrates by varying the B-site flux ratio of TTIP to HMDT, from 100% TTIP for the first end member BTO (x = 0) to 100% HMDT for the second end member BSO (x = 1), while holding the A-site flux of elemental metal Ba constant. Individual fluxes were measured prior to growth as a BEP. Because the individual B-site fluxes required for BTO or BSO growth were not the same, BEP(TTIP) = 1.1×10^{-6} Torr and BEP(HMDT) = 2.7×10^{-6} Torr, respectively, fluxes were increased or decreased as a percentage of their individual total. In the end, the desired amount of Sn compared to Ti incorporation (x) was estimated prior to growth using Equation 7.1.

$$x\,(BEP) = \frac{BEP(HMDT)}{BEP(HMDT)+BEP(TTIP)} \tag{7.1}$$

The HRXRD patterns around the (002) film and substrate peaks for ~ 45 nm films grown from x = 0 to x = 1, bottom to top, are shown in Figure 7.1a. The c-axis of BTO, the

expected out-of-plane orientation, has a smaller lattice parameter (4.036 Å) compared to the cubic lattice parameter of BSO (4.116 Å). As a result of this difference and as was expected, a shift in the (002) film peak from higher to lower 2θ occurred as HMDT flux was increased and TTIP flux was decreased. The peak shift to lower 2θ, or lattice expansion, not only signified the incorporation of Sn, but also that Sn is most likely substituting into the B-site. At the B-site, Sn^{4+} has a larger atomic radius than Ti^{4+}, indicating an expansion of the lattice. If Sn were to go into the A-site, Sn^{2+} would have a smaller atomic radius than Ba^{2+}, indicating the opposite. The incorporation of Sn and its 4+ oxidation state was later confirmed after growth using XPS and STEM.

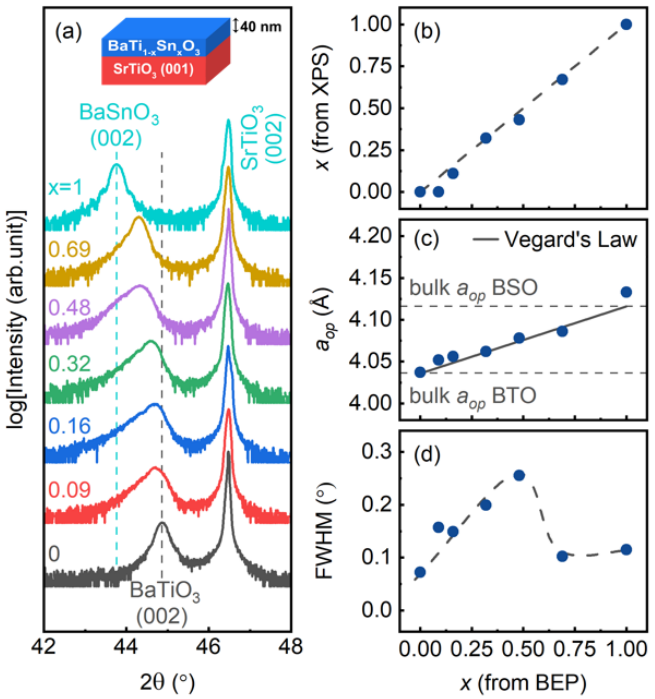

Figure 7.1. (a) High resolution X-ray diffraction patterns of ~ 45 nm $BaTi_{1-x}Sn_xO_3$ films on $SrTiO_3$ (001). (b) Atomic percentage of Sn (*x*) determined by XPS plotted against the atomic percentage estimated from BEP ratio. (c) Out-of-plane lattice parameter (a_{op}) and (d) FWHM of film (002) rocking curve. Solid line in (c) is the expected a_{op} from Vegard's law.

The simple relation in equation 1 turned out to be a good estimation of the Sn incorporation as evidenced by XPS measurements taken after growth. The amount of Sn in the films was measured, albeit just from the surface, using XPS and is plotted against the estimated x from BEP measurements (Equation 7.1) in Figure 7.1b. A close to one-to-one relationship was found between the two, which is a positive from a synthesis aspect as the amount of Sn can be reliably predicted from the growth conditions. It should be noted that the sample with the smallest amount of Sn (x = 0.09) did not show a Sn signal from XPS. However, evidenced by the expansion of the lattice parameter, Sn was incorporated into the film and this was later confirmed by TEM. Because there was Sn present in this film, the referred to composition, x, throughout this report is based on the BEP measurements and not from XPS. There is error in these values from both methods, BEP being from an indirect measurement as well as the inherent error from XPS, but the one-to-one relation in Figure 7.1b gives confidence to these values.

Taking the peak intensity position from each film, a_{op} was calculated and is shown in Figure 7.1c. As Sn incorporation increased, a_{op} increased from the bulk BTO value to close to the bulk BSO value as predicted by Vegard's law.[236] The larger discrepancy for the BSO (x = 1) film has previously been shown to be due to residual strain remaining in the film.[149] Following Vegard's law between BTO and BSO once again shows the Sn is being substituted for Ti at the B-site.

While a_{op} was taken from the peak intensity position, the (002) film peaks were, in all cases except x = 0 and 1, asymmetric. As Sn incorporation increased, so did the asymmetry up to x = 0.48 where it then began to return to a more symmetric shape. The

asymmetry indicates there is a range of lattice parameters in these alloyed films. The same trend was also observed in the FWHM of the film (002) rocking curves, seen in Figure 7.1d. Together, these trends signify increased disorder in the film as the Sn concentration increases, up to a point where it sharply returns to a less defective structure with a FWHM similar to that of BSO. The disorder may signify the increasing presence of multiple phases or complicated domain structures involving polar nanoregions (PNR) as Sn is added to the structure. This will be discussed based on SHG and STEM results in the following sections.

7.2 Symmetry and Polarization

While the hybrid MBE synthesis technique used here gave great control over the Sn to Ti composition, it became clear that understanding the arrangement of Sn and Ti and the evolution of the resulting structure and symmetry required further analysis. BSO has the prototypical cube perovskite crystal structure, $Pm\bar{3}m$, but, after alloying with BTO which is tetragonal, $4mm$, it should be expected that a change in symmetry occurs with the change in structure observed by HRXRD. To determine the crystal symmetry, optical second harmonic generation (SHG) polarimetry was utilized, a schematic of which is shown in Figure 7.2.[237]

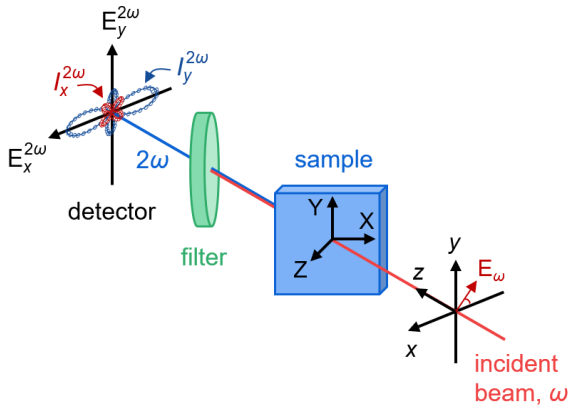

Figure 7.2. Schematic representation of SHG measurement. Incident beam of frequency ω interacts with a sample and combines to a collected signal 2ω, after residual incident signal is filtered out. The collected signal intensity along the two directions, $I_x^{2\omega}$ and $I_y^{2\omega}$, can be fit to determine the crystal symmetry.

SHG relies on nonlinear optical phenomena where two photons, at a wave frequency ω, combine after interacting with a material into a single, collected photon of frequency 2ω. In SHG, the collected signal, $I_x^{2\omega}$ and $I_y^{2\omega}$, will only be seen if the material measured has no inversion symmetry, or is non-centrosymmetric. Therefore, from this measurement technique, the cubic centrosymmetric BSO sample, $x = 1$, should not have an SHG signal, which was the case in the measurements here. In fact, no signal could be collected until the $x = 0.48$ sample. This result signifies that a large amount of Ti can be substituted into BSO, at least until $x = 0.69$, and the symmetry will remain centrosymmetric.

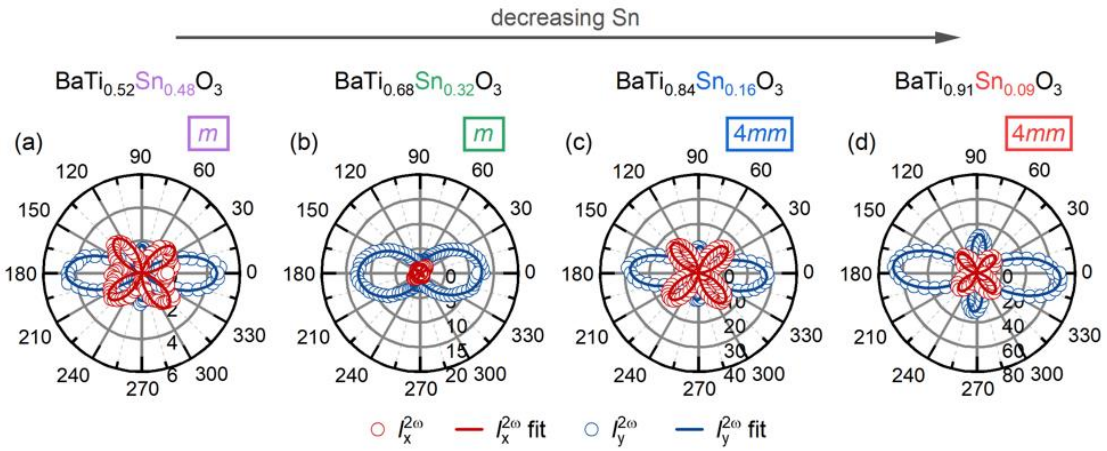

Figure 7.3. SHG polar plots for BTSO films, decreasing Sn incorporation from left to right. The point group obtained from each individual fitting is found in the top right of the plot. No signal was seen for $x = 1$ and 0.69.

As the amount of Sn was decreased further, an SHG signal, albeit a small one, was first seen at $x = 0.48$ and then for all other samples with smaller x. Polar plots and their fittings for all Sn-modified samples which showed signal are shown in Figure 7.3. The symmetry change can be seen from the point group obtained from the fittings, a change from $Pm\bar{3}m$ to m and finally to $4mm$. With small amounts of Sn, up to $x = 0.16$ here, the tetragonal structure of BTO remains, which is a promising result for the enhanced ferroelectric properties of BTO. Noticeably, this result differs from bulk ceramic reports where a shift from tetragonal to orthorhombic at room temperature occurs at $x \approx 0.04$.[58] This indicates the stabilization of the higher-temperature phase when in thin film form, an effect most likely imparted by the substrate.

Temperature-dependent SHG (Figure 7.4a – 7.4d) and HRXRD (Figure 7.4e – 7.4h) measurements were then performed to see if any changes in crystal symmetry or any phase

transition could be determined. First, from SHG, all samples exhibited a decrease in the SHG signal with increasing temperature, meaning they are developing their inversion symmetry. This is a common result in ferroelectrics and relaxor ferroelectrics, for example BTO transitioning to a cubic structure at ~ 120°C. Broad peaks in SHG were seen upon heating in the two samples with the least Sn and could signify a phase transition. However, this is difficult to determine based solely on SHG as many phenomena could cause this, for example changes in domain formation.

Instead, a better method is to track the change in a_{op} with temperature from HRXRD scans. From these measurements, a_{op} increases linearly with large amounts of Sn, $x \geq 0.32$ for the temperature range measured here (Figure 7.4e and 7.4f). However, as Sn is decreased further, a non-linear change in a_{op} occurred and resembled what is typically seen for a phase transition in these BTO-based materials. From the local minimum at higher temperature, T_c of 320°C and 340°C was obtained for $x = 0.16$ and 0.09, respectively. The increase in T_c with decreasing Sn does follow the usual trend of BSTO, but because data points were taken only every 20°C, these are most likely just within error of each other. Finally, with regards to the broad peaks seen in SHG, the change in a_{op} did not match with temperature-dependent SHG intensity, therefore indicating the peak in the SHG results were not directly caused by a phase transition.

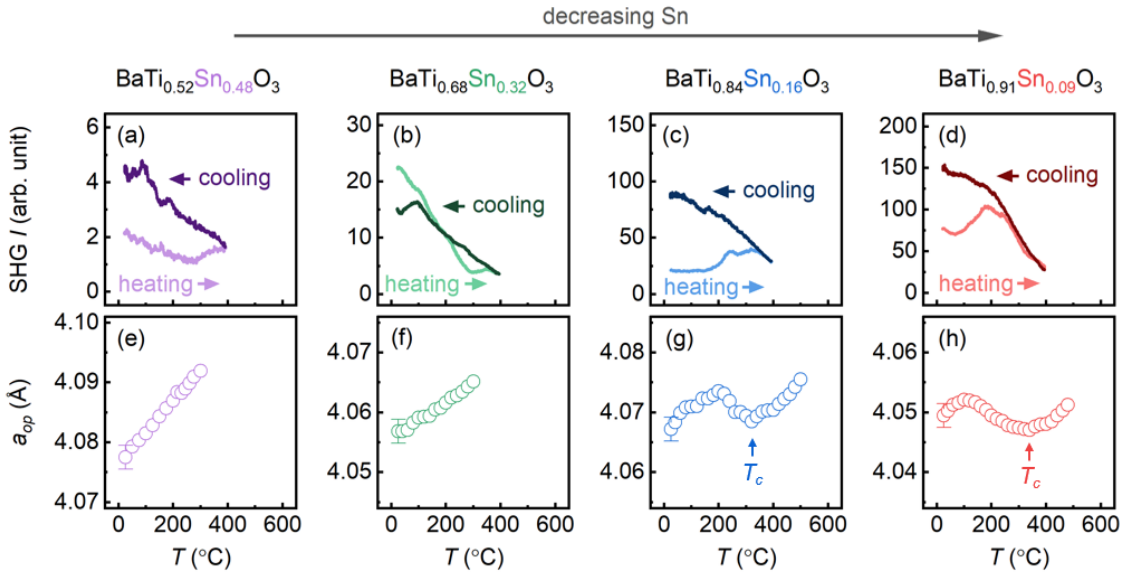

Figure 7.4. Temperature dependent (a-d) SHG intensity upon heating and then cooling to 400°C and (e-h) a_{op} upon heating obtained from HRXRD. Error bars for all a_{op} are the same but only displayed for the first data point.

SHG also allows for an estimation of the overall polarization of a material based on the collected intensity, as the square root of SHG intensity is proportional to the polarization. When alloying from BSO to BTO, the polarization should increase and this was the case here, shown in Figure 7.5. A maximum in polarization was seen at $x = 0.09$, close to the expected maximum based on ceramic results ($x \approx 0.11$).[58] For future work, effort should be given to finer composition control around this point, to determine exactly where the maximum polarization is achieved.

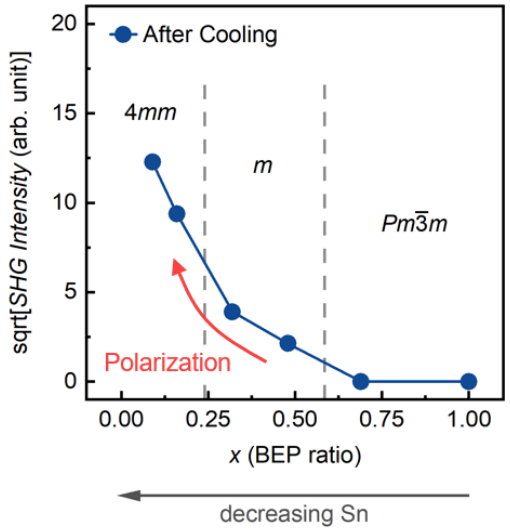

Figure 7.5. Room-temperature square root of the SHG intensity, which is proportional to polarization, plotted against the Sn to Ti ratio, *x*, after heating to 400°C and then cooling. Point groups are noted for samples in each respective region. The boundaries are not exact.

It should also be noted that SHG and temperature dependent HRXRD was performed on the BTO $x = 0$ sample. However, from the TEM results (Figure 7.6), which will be described further for other samples, it was discovered that the $x = 0$ sample was non-stoichiometric. BaO rock salt structure was seen in TEM, indicating a Ba-rich film. For this reason, comparing SHG signals from this sample would not be feasible as the non-stoichiometry negatively impacts the phase transition as well as the overall ferroelectric and SHG response. Other samples measured in TEM did not show these non-stoichiometric related phases or defects.

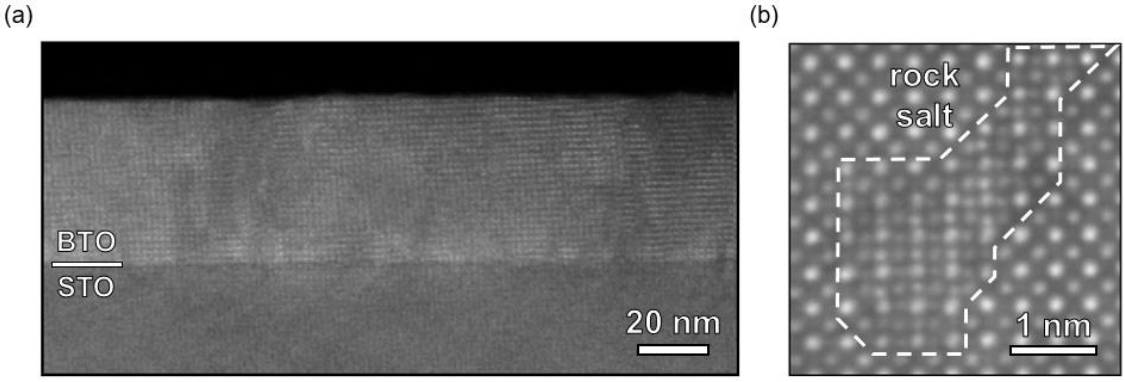

Figure 7.6. (a) Cross-sectional HAADF-STEM image of the BTO (x = 0) sample, viewed along the [100] zone axis. (b) Atomic resolution image of select region highlighting the rock salt structure, signifying a non-stoichiometric material.

7.3 Local Disorder

SHG is a relatively macroscopic technique, able to probe a large area of a sample (~ 28 μm spot size). As an example of the impact of this, while the symmetry results from compositions x = 0.32 and 0.48 were monoclinic, this is only the highest symmetry able to be assigned on this macroscopic level. As observed from the asymmetry and the increasing FWHM from the HRXRD results, the structure and symmetry of these films are most likely too complicated to be assigned to one single point group. To examine the structure of these films on a more local level and determine exactly how the Sn to Ti ratio affects the structure and symmetry, STEM was employed.

STEM results for two samples will be discussed: 1) x = 0.09, the composition which showed the maximum in polarization and 2) x = 0.48, the composition which showed the maximum disorder as evidenced by the FWHM. To first determine how the Sn and Ti dispersed throughout the film, energy-dispersive x-ray spectroscopy (EDX) was used and

the results are shown in Figure 7.7. An accumulation of Sn was observed in different areas for both samples. At x = 0.09, up to about 8 nm from the film-substrate interface, a band of Sn accumulation occurred and was accompanied by a lack of Ti. This would explain why no Sn signal was seen in XPS but still an expansion in a_{op}, as a large majority of the Sn was located below the surface near the interface. With much more Sn incorporation, x = 0.48, a band was not seen but Sn accumulation did occur in small groupings near the interface, around misfit dislocations. Sn may have diffused and accrued near these dislocation centers if they are favorably Ti rich, but this will the focus of future studies.

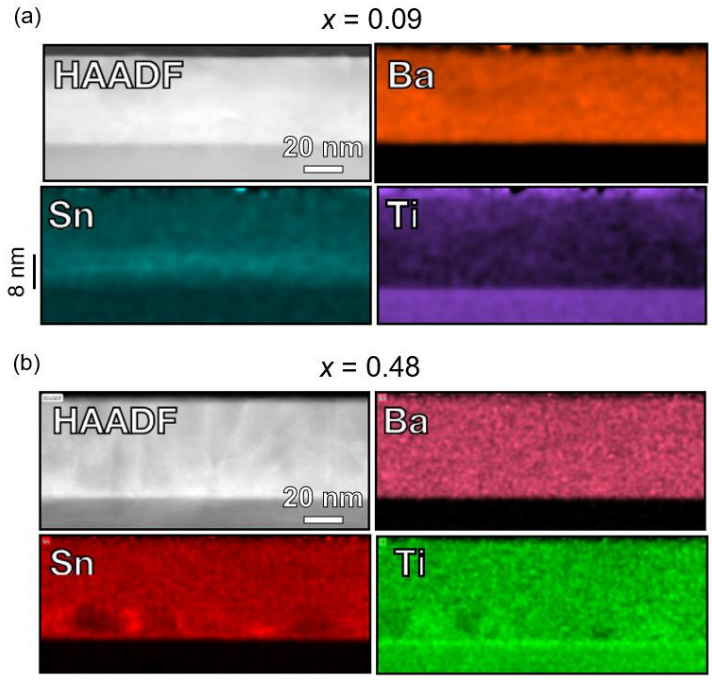

Figure 7.7. HADDF-STEM image and STEM-EDX mapping of Ba, Sn, and Ti for (a) x = 0.09 and (b) x = 0.48.

Atomic resolution images were then taken, Figure 7.8, and ordered atomic columns could be seen in both cases, with no evidence of non-stoichiometric-related defects or

phases like in the $x = 0$ sample discussed earlier. Misfit dislocations were present along the interfaces as a result of strain relaxation, unsurprising as both films have considerably larger lattice parameters than the substrate, STO. Up to a few nanometers away from the interface, significant disorder existed due to the increase Sn accumulation and dislocations.

To get an idea of how the bulk of the films behaved, projected displacement maps were formed away from the disordered interfaces and based on the displacement from center of the cations (Ba^{2+}, Ti^{4+}, and Sn^{4+}) relative to the anions (O^{2-}), shown in Figures 7.7b and 7.7f for $x = 0.09$ and 0.48, respectively. At $x = 0.09$, long-range polarization existed with the majority oriented out-of-plane in the [001] direction. However, PNRs, clusters of random polarization directions, were present. These regions have been shown in other material systems, especially relaxor ferroelectrics, to increase dielectric and piezoelectric response,[238] agreeing well with the increased polarization based on SHG. Multiple polarization domains were also imaged, with 90° and 180° domain walls easily visible on the displacement map. In the case of higher Sn concentrations, at $x = 0.48$, much more disorder was seen and long-range polarization diminished. The material began to look more like a relaxor ferroelectric, agreeing with heightening of disorder from HRXRD.

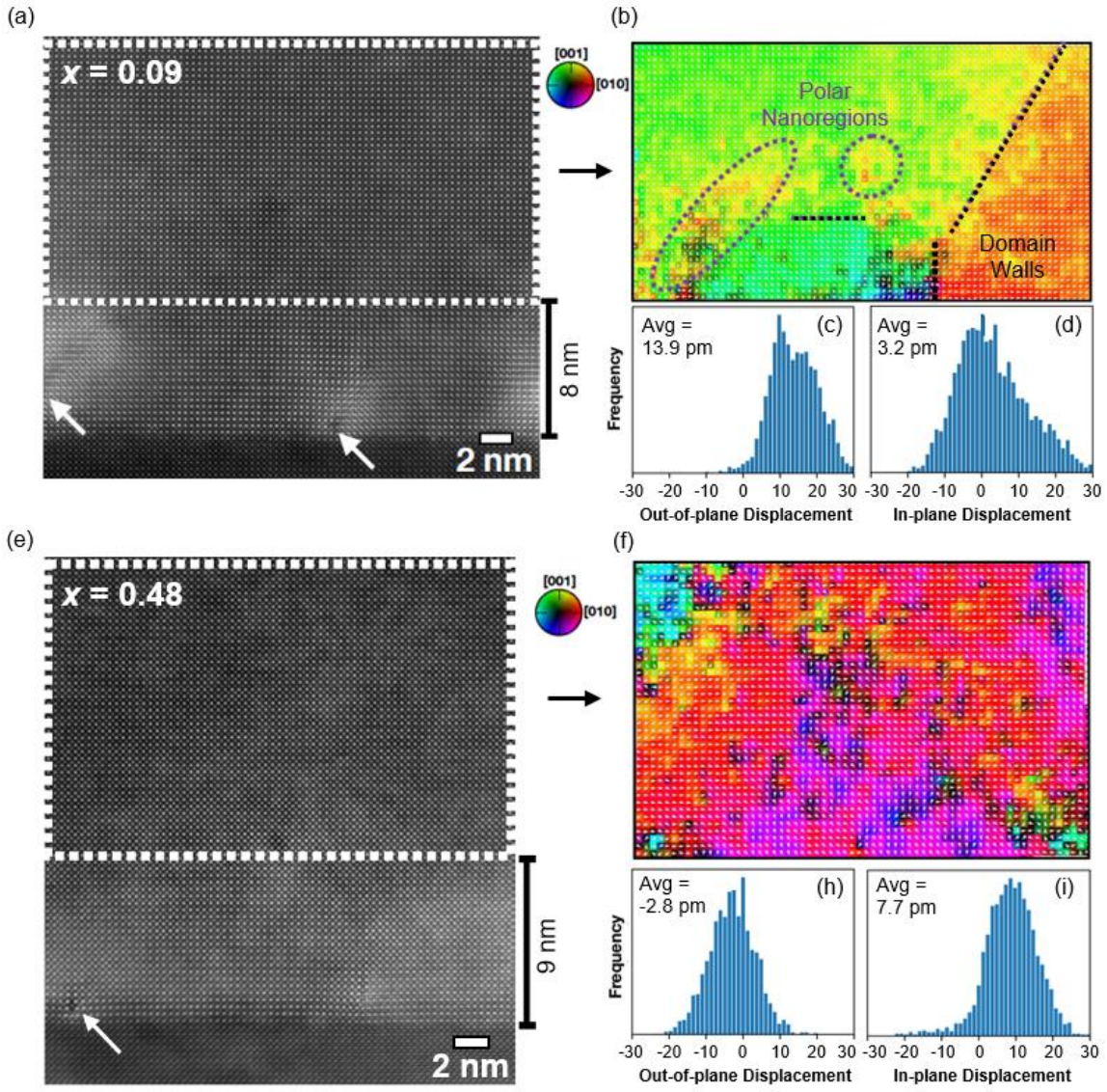

Figure 7.8. HAADF-STEM images of the film-substrate interface for (a) $x = 0.09$ and (e) $x = 0.48$. Arrows mark examples of disordered regions due to misfit dislocation formation. Purple and black dashed lines signify PNRs and domain walls, respectively. Highlighted area is the region of the (b) and (f) projected displacement (polarization) maps, away from the film-substrate interface. Histograms of the out-of-plane and in-plane components of the projected displacement are given in (c) and (d) for $x = 0.09$ and (h) and (i) for $x = 0.48$, respectively.

As a comparison between the two samples, and to try to compare to the SHG results for relative polarization, histograms of the atomic displacements were made and split into

an out-of-plane and in-plane component, Figure 7.8. Consistent with the SHG results, increased displacement, or polarization, out-of-plane was discovered in $x = 0.09$, with about 5x as large of values (SHG ~ 6x increase). Additionally, the displacement was largely out-of-plane with a very small in-plane component, which is favorable for creating thin film capacitors or most other related devices.

In conclusion, BSTO films were grown to complete the alloy system from $BaTiO_3$ to $BaSnO_3$ using the hybrid MBE technique. Film lattice parameters were found to agree well with Vegard's law and the composition of Sn to Ti could be reliably predicted based solely on the Sn to Ti metal-organic precursor fluxes. SHG was used to determine overall crystal symmetry and relative polarization. Starting with BSO, a centrosymmetric cubic structure, a transition to a monoclinic and then tetragonal structure occurred as Sn was decreased. This trend was also accompanied by an increase in polarization, as estimated by the SHG collected intensity, with a maximum at $x = 0.09$ which agreed well with bulk ceramic reports. Finally, from STEM results, long range polarization was confirmed in the $x = 0.09$ sample with an out-of-plane cation to anion displacement 5x that of $x = 0.48$, the sample which showed the most structural disorder.

Future efforts should be given to understanding the migration of Sn as it relates to defects, such as accumulation near interfaces and dislocations. Confirming the increase in polarization towards $x = 0.09$ by fabricating a proper MIM capacitor will also be fundamental to understanding the impact of Sn.

Chapter 8

8. Solid Source Metal-Organic Molecular Beam Epitaxy

Advances in physical vapor deposition techniques have led to a myriad of quantum materials and technological breakthroughs affecting all areas of nanoscience and nanotechnology which rely on the innovation in synthesis. Despite this, one area that remains challenging is the synthesis of atomically precise complex metal oxide thin films and heterostructures containing "stubborn" elements that are not only non-trivial to evaporate/sublimate but also hard to oxidize. For example, being able to deposit Pt or $SrRuO_3$ in a simpler, more cost-effective, and safer way would be advantageous for the growth of *in-situ* electrodes for ferroelectric heterostructures, as has been discussed. Here, a simple yet atomically-controlled novel synthesis approach that bridges this gap is presented.

This chapter was adapted from a yet to be published work: William Nunn, Anusha Kamath Manjeshwar, Jin Yue, Anil Rajapitamahuni, Tristan K. Truttmann and Bharat Jalan. Novel Synthesis Approach for "Stubborn" Metals and Metal Oxides. *Proc. Natl. Acad. Sci.* (to be published August 2021).

Using platinum and ruthenium as examples, both the challenges of low vapor pressure and difficulty in oxidizing a stubborn element are addressed by using a solid metal-organic compound with significantly higher vapor pressure, and with the added benefits of being in a pre-oxidized oxidation state along with excellent thermal and air stability. Synthesis of highly perfect single crystalline, epitaxial Pt and RuO_2 films is demonstrated, resulting in a record-high residual resistivity ratio (RRR = 27) in Pt films and low residual resistivity of ~ 6 $\mu\Omega\cdot$cm in RuO_2 films. Further, using $SrRuO_3$ as an example, the viability of this approach for more complex materials is demonstrated with the same ease and control that has been largely responsible for the success of the molecular beam epitaxy of III-V semiconductors.

This approach is a major step forward in the synthesis science of "stubborn" materials which have been of significant interest to the materials science and the condensed matter physics community. Atomically precise complex oxides, containing these elements such as ruthenium, iridium, and platinum among others, hold tremendous promise as designer quantum materials for exploring novel electronic, magnetic, superconducting, and topological phases owing to their strong spin-orbit interaction. The studies described here show this novel method to synthesize such materials by eliminating the major synthesis bottleneck discussed. These results provide significant insights to researchers seeking to synthesize defect-managed thin films and interfaces with atomic layer control. This study serves as a "proof-of-concept" allowing 1) growth of Pt, RuO_2 and $SrRuO_3$ thin films by supplying Pt and Ru precursors at 65°C-100°C in a low-temperature effusion cell as opposed to the several thousand °C needed using electron-beam evaporators, 2) a bulk-like

room temperature resistivity, and 3) ultimately, novel pathways to creating atomically precise quantum structures.

8.1 Challenges with "Stubborn" Metals

Improvements in thin film deposition processes have broadly impacted many technology innovations and breakthroughs,[90,239] not only by shaping the current electronics industry, but by also extensively affecting areas such as optics, solar cells, coatings, biomedical devices, and aerospace engineering. Developing synthesis techniques for material improvement is driven in part by the desire to achieve intrinsic properties in thin films, a challenge that has and continues to motivate materials scientists and physicists. However, as deposition processes have advanced, many new phenomena have been discovered due to the increased control over chemistry, structure, and defects. For example, it was the ability to grow a heterostructure with an interface very low in defects that led to the discovery of the integer and fractional quantum Hall effect (1985 and 1998 Physics Novel Prize).[90] Similarly, exotic new phases such as 2D-electron gases and superconductivity have been made possible as a result of being able to grow heterostructures with these high quality interfaces.[240-242] Control over structure and defects has also led to ever improving properties such as electron mobilities,[243] in some cases surpassing those of the bulk material itself.[244] Finally, the additional advantage of epitaxial strain has allowed for an enhancement or emergence of certain material properties e.g. ferroelectricity[67,68] and superconductivity.[245,246]

Advancements in deposition techniques, like MBE and other PVD approaches, have recently largely relied on process optimization and improvements in vacuum level.[247] Many materials have still proven challenging to grow, especially when they contain metals with ultra-low vapor pressures which therefore require extremely high temperatures to evaporate or sublime.

Figure 8.1a shows the vapor pressures of a few commonly used metals[248] as well as the typical vapor pressure range used in MBE growth, 10^{-5} – 10^{-2} Torr. While, for example, effusion cells are suitable for the sublimation of Sr and Ba, commonly used in various complex oxides, or evaporation of Al and Ga, used in GaAs/AlGaAs heterostructures, their use for refractory and noble metals such as Pt, Ru, Ir, and W can prove difficult or even impossible. To overcome this problem, most turn to electron beam evaporation which is capable of heating a material to much higher temperatures than an effusion cell. Although this allows for sufficient vapor pressure, difficulties can arise with maintaining a constant flux due to the extremely localized heating and due to potential safety issues. Synthesizing thin films of complex materials can therefore become problematic as controlling the relative fluxes of the precursor materials is key to stoichiometry control. Feedback control can be used to maintain the flux, but this can be complicated and add to the already large cost and complexity of electron beam evaporators.[162]

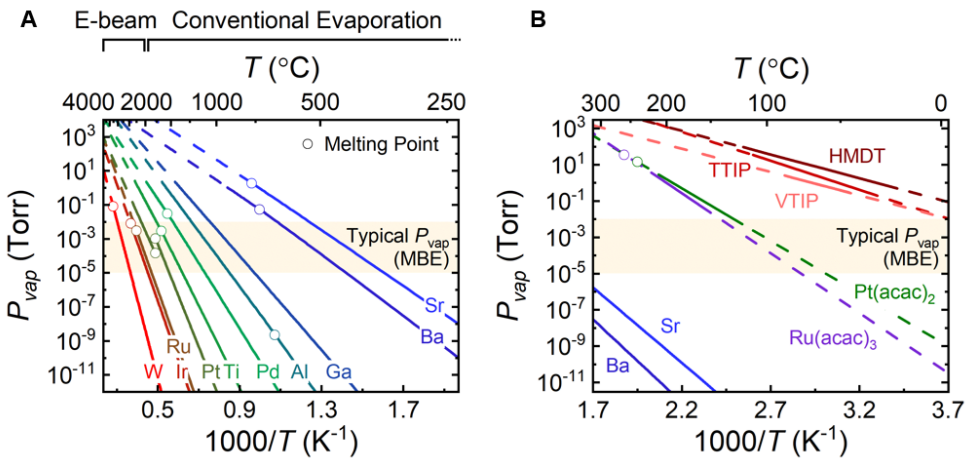

Figure 8.1. (a) Vapor pressures (P_{vap}) for a variety of commonly used metals in thin film deposition processes. Dashed lines are linear extrapolations. (b) Vapor pressure of $Pt(acac)_2$ and $Ru(acac)_3$ compared to commonly used metal-organics and metals in MBE.

Other problems can occur in PVD when growth is complicated with the addition of gases such as oxygen for the synthesis of oxide materials. Many metals have problems with source oxidation or low oxidation potentials, such as Ti and Sn, respectively. For MBE, a modification of the conventional technique, known as hybrid or metal-organic MBE (MOMBE), has successfully overcome some of these issues by using metal-organic precursors for a few of the metals in question. These techniques utilize volatile metal-organic compounds, containing the desired metal, injected into the vacuum system through an external gas inlet system. Although metal-organic precursors have been found to address the issues of low vapor pressures, oxidation of source materials, and low oxidation potentials for metals like Ti,[86] Sn,[149] and V,[148] it has been non-trivial to find suitable precursors for other metals.

8.2 Solid Source Metal-Organic Molecular Beam Epitaxy Approach

To this end, a new technique has been developed and will be described here for supplying metallic elements for the growth of metals or metal-containing materials in PVD processes, specifically targeting ultra-low vapor pressure elements. Metal-organic compounds can be designed to supply these elements, partially or completely oxidized to the desired oxidation state and with additional oxygen bonded to the metallic center by the choice of suitable ligands. Specifically, if this metal-organic compound is a solid and air stable, it can be sublimed in an effusion cell at a relatively low temperature. This technique shows that it is possible to deliver the desired metal for growth of high-quality single crystalline films and without the risk of oxidizing elemental sources and components of the vacuum chamber. Although similar to hybrid MBE, which also uses metal-organic precursors, this technique differs in an important way. In hybrid MBE, precursors are usually evaporated as a liquid with a large vapor pressure of ~10 Torr at operating temperature. To achieve this, the precursor must be placed in a bubbler outside the vacuum chamber. By using a precursor which is solid and has an intermediate vapor pressure, the compound can be placed in a conventional low-temperature effusion cell directly in the vacuum chamber irrespective of the background pressure. This technique thus solves the problem of it being difficult to find metal-organic compounds for hybrid MBE which requires high vapor pressures and consequently liquid compounds in all reports thus far. For this reason, this technique will be referred to as *solid-source* MOMBE. This process also differs from some solid source metal-organic chemical vapor deposition techniques[249,250] because with the precursor placed directly in the vacuum system, no

carrier gas is needed so a large mean free path is retained for growth when the background pressure is low.

As a demonstration of the potential of this synthesis technique for the growth of ultra-low vapor pressure metals and metal containing oxides, a variety of materials were grown including the simple metal Pt, binary oxide RuO_2, and complex oxide $SrRuO_3$ using the metal-organic precursors platinum(II) acetylacetonate, $Pt(acac)_2$, and ruthenium(III) acetylacetonate, $Ru(acac)_3$. Pt films have been useful as electrodes for dielectric materials due to its high work function and recent interest has also included the study of the spin Hall effect where films low in defects are desired.[251] RuO_2 has been studied for its low resistivity and high chemical and thermal stability for applications such as electrodes in supercapacitors,[252] catalysts in reactions like the oxygen evolution reaction,[253] and recently for the discovery of superconductivity when strained.[245] Finally, $SrRuO_3$ has been a material of significant interest due to its itinerant ferromagnetism, presence of the anomalous Hall effect, and for its use as electrodes in oxide electronics.[254] This work opens up a new method for tackling the highly rewarding problem of stabilizing challenging metals like these for further use and study of these exciting phenomena and applications.

The metal-organics $Pt(acac)_2$ and $Ru(acac)_3$ were identified as suitable precursors due to their vapor pressures falling in the desired range at low temperatures, about 10^{-3} Torr at 100°C.[255] In fact, films were grown here with source temperatures of only 65°C - 85°C for Pt and 100°C for RuO_2. Figure 8.1b shows the vapor pressure of $Pt(acac)_2$ and $Ru(acac)_3$ compared to metallic elements Ba and Sr and volatile metal-organics vanadium(V) oxytriisopropoxide (VTIP), TTIP, HMDT, commonly used in MBE.

$Pt(acac)_2$ and $Ru(acac)_3$ are also solids at these temperatures, with a melting point of 240°C[256] and 260°C,[257] respectively, which is important for its ease of use in an effusion cell. $Pt(acac)_2$ and $Ru(acac)_3$ are also thermally stable until about 210°C and 230°C,[255] respectively, indicating thermal decomposition does not occur at typical growth temperatures. These precursors additionally come bonded with oxygen in the ligands, which can act as an additional source of oxygen for growth of oxides. Finally, $Pt(acac)_2$ and $Ru(acac)_3$ are also non-toxic, removing some safety concerns that can come with the use of organometallic precursors like HMDT in hybrid MBE growth of Sn-containing compounds.[149] Table 8.1 summarizes some of these important factors that must be considered for PVD techniques and compares this approach to e-beam assisted MBE and hybrid MBE techniques.

Table 8.1. Factors which are critical to consider in physical vapor deposition techniques.

Factors Critical to PVD	Electron-Beam Assisted MBE	Hybrid MBE	Solid Source MOMBE
Vapor pressure	Ultra-low	High	Intermediate
Source state	Solid	Liquid	Solid
Oxygen in source	No	Yes	Yes
Pre-oxidized source	No	Yes	Yes
Source air stability	Yes	Yes	Yes
Complexity	High	Moderate	Low
Delivery Method	Electron-beam	External gas inlet	Effusion cell
Safety	High voltages	Can be toxic	No concern

A schematic of the technique setup is shown in Figure 8.2 involving a low temperature effusion cell for the metal-organic, oxygen plasma (needed for (001) crystal orientation control in Pt[258]), and an additional conventional effusion cell for expansion to more complex materials, such as using Sr for the $SrRuO_3$ grown here.

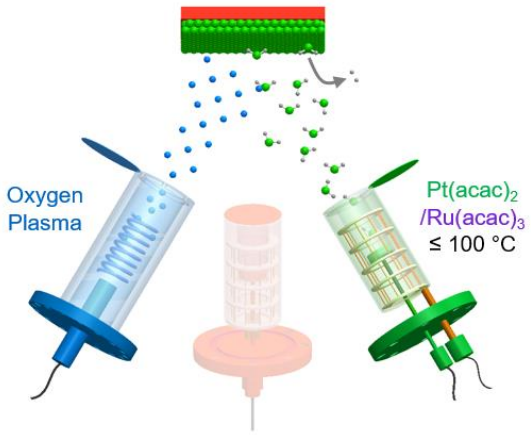

Figure 8.2. Schematic of solid-source metal-organic MBE technique.

An effusion cell (E-Science, Inc., US) was used for the low-temperature, 65°C - 85°C, sublimation of $Pt(acac)_2$ (97%, MilliporeSigma, US) and 100°C sublimation of $Ru(acac)_3$ (97% for RuO_2 and $SrRuO_3$, MilliporeSigma, US and 99.99% for RuO_2, American Elements, US). Sr was also supplied by an effusion cell for the growth of $SrRuO_3$. The powder precursors were placed directly in a pyrolytic boron nitride (PBN) crucible (E-Science, Inc., US) inside an effusion cell. A BEP of ~2 x 10^{-7} Torr was measured for Pt at 65 °C and ~1 x 10^{-7} Torr for Ru at 100°C. Both materials were grown in an oxygen environment as it has been shown necessary for the stabilization of the (001) epitaxial orientation[258] in Pt and to ensure complete oxidation of RuO_2 and $SrRuO_3$.

Oxygen was supplied at a pressure of 5 x 10^{-6} Torr by a radio-frequency (RF) plasma source (Mantis, UK) operated at 250 W and with charge deflection plates. Pt films were grown on $SrTiO_3$ (001) and Nb-doped $SrTiO_3$ (001) single-crystal substrates (Crystec GmbH). RuO_2 films were grown on TiO_2 (110) and TiO_2 (101) (MTI Corporation, US). $SrRuO_3$ films were grown on $SrTiO_3$ (001) (Shinkosha, Japan). The substrate surfaces were cleaned for 20 - 30 minutes in oxygen plasma prior to growth. Substrate temperatures were 760°C for Pt, 300°C for RuO_2, and 665°C for $SrRuO_3$. Following growth, the films were cooled in an oxygen plasma environment.

Temperature-dependent four-terminal resistivity measurements were performed down to 1.8 K using indium as an ohmic contact for Pt and aluminum for RuO_2 and $SrRuO_3$ in a DynaCool Physical Property Measurement System (Quantum Design, US). Hall measurements were performed using a four-quadrant sweep of magnetic field between -9 T and +9 T normal to the film surface in the DynaCool PPMS. Temperature and magnetic field-dependent magnetization measurements were performed with a magnetic field applied along the in-plane [001] azimuth of the $SrTiO_3$ substrate using the Vibrating Sample Magnetometry (VSM) option in an EverCool Physical Property Measurement System (Quantum Design, US). Structural characterization techniques used are described in more detail in Chapter 3.

8.3 Platinum Growth

Pt films were grown on $SrTiO_3$ (001) substrates using a $Pt(acac)_2$ source temperature of only 65°C. The low-temperature sublimation led to films with structural

characteristics very similar to previous reports of Pt films grown on $SrTiO_3$.[259-261] Single platinum (002) peaks were present in the HRXRD, as seen in down to 520°C showing phase pure films with an epitaxial (001) orientation parallel to the substrate surface. Thickness fringes on the (002) peaks were present at higher substrate temperatures and gave thicknesses of 9 to 16 nm, linearly increasing from 760°C to 930°C, for a one-hour growth, seen in Figure 8.3a.

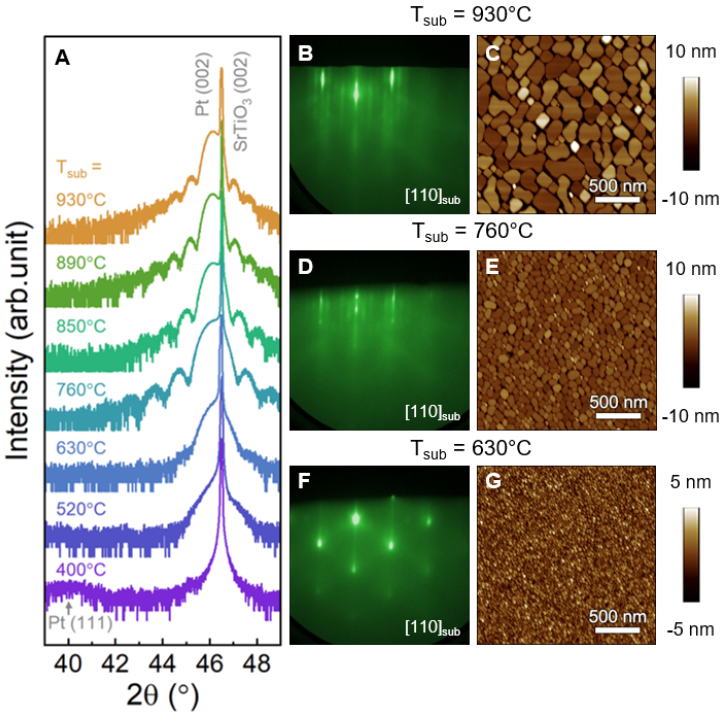

Figure 8.3. (a) HRXRD of Pt films on $SrTiO_3$ (001) substrates with increasing substrate temperature from bottom to top. (b), (d), (f) RHEED and (c), (e), (g) AFM of substrate temperatures 930°C, 760°C, and 630°C, respectively.

Although the HRXRD in Figure 8.3a suggested single crystalline films, the microstructure of the films visualized by AFM proved otherwise. Atomically smooth islands were seen with a decreasing island size as the substrate temperature was decreased.

The elongated island morphology shown here at higher temperatures is commonly attributed to the favorable agglomeration of metals on dielectric materials. A transition from 2-D to 3-D growth occurred as substrate temperature was increased. At a temperature of 630°C and below, the film surface consisted of many smaller faceted islands. This can also be seen in the RHEED patterns after growth along the $SrTiO_3$ [110] azimuth, a spotty pattern occurred from transmission through these faceted islands. As the substrate temperature was increased, RHEED evolved into a streaky pattern due to diffraction from the atomically smooth island surfaces. Finally, when the substrate temperature was decreased to 400°C, the Pt (002) peak disappeared and the Pt (111) peak appeared, the energetically preferred orientation for Pt.

Historically, growing atomically smooth Pt films on dielectric substrates such as $SrTiO_3$ has been difficult but is desired for electrode heterostructure applications, as is a motivation here. Instead of growing on $SrTiO_3$, here, it was found that by changing to a conducting substrate, Nb-doped $SrTiO_3$, Pt films were able to be grown with these desired surfaces. A 70 nm Pt film with a single peak in HRXRD is shown in Figure 8.4a. Steps are seen on the surface from AFM images, Figure 8.4b, with a step height of one Pt unit cell, showing this technique is able to grow films with atomically-smooth surface. Similar RHEED patterns were obtained as those films grown at high substrate temperatures on undoped $SrTiO_3$, but with more well-defined streaks, attesting to the high crystalline quality and smooth surface.

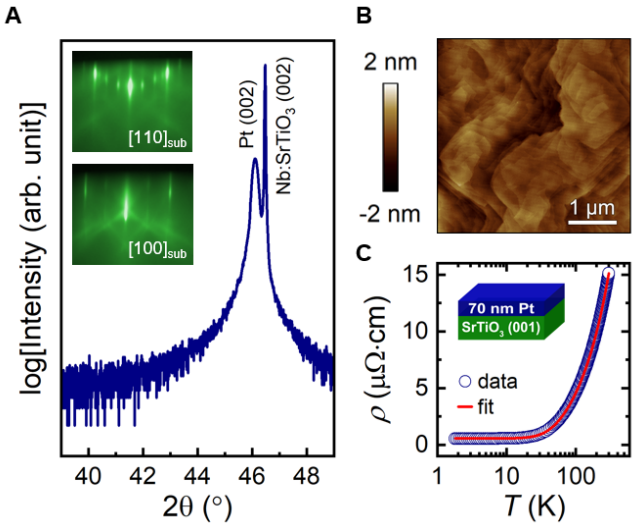

Figure 8.4. (a) HRXRD and (b) AFM of 70 nm Pt film grown on conducting Nb-doped $SrTiO_3$ (001) substrate. Inset of (a) shows RHEED along the substrate [110] and [100] azimuths. (c) Resistivity of 70 nm Pt film grown on insulating $SrTiO_3$ (001) substrate. Red line is fit to Bloch–Grüneisen behavior.

To test the electronic properties of the Pt films, a 70 nm film was grown at an intermediate $SrTiO_3$ substrate temperature of 760°C along with a source temperature of 85°C to increase the growth rate, from 9 to 35 nm/hr, also thereby showing a scalable growth rate. Temperature-dependent resistivity measurements were performed in van der Pauw geometry[262] down to 1.8 K as can be seen in Figure 8.4c. A room-temperature resistivity (ρ) of 15 μΩ·cm was obtained, slightly larger than the bulk Pt value of ~ 11 μΩ·cm. The residual resistivity ratio (*RRR*), defined here as ρ(300 K)/ρ(1.8 K), was 27. The resistivity vs temperature behavior was then fit with the Bloch-Grüneisen equation[263]

$$\rho = \rho_0 + \rho_{ee}T^2 + \rho_{sd}T^3\frac{J_3(\theta/T)}{7.212} + \rho_{ss}T^5\frac{J_5(\theta/T)}{124.14}, \quad (8.1)$$

where

$$J_N\left(\theta/T\right) = \int_0^{\theta/T} \frac{x^N dx}{(e^x-1)(1-e^{-x})}\,. \tag{8.2}$$

The Bloch-Grüneisen equation models the resistivity of metals considering contributions from electron-electron scattering (ρ_{ee}), interband scattering (ρ_{sd}), and intraband scattering (ρ_{ss}) in addition to the residual resistivity (ρ_0). The resistivity in bulk Pt is known not to be described by electron-electron scattering. The intraband scattering term was also found to be negligible. Excellent fits were obtained using only the ρ_0 and contribution from ρ_{sd} terms. Debye temperature Θ_D of 232 K was determined from the fitting, agreeing well with the bulk value of 240 K.[264] These observations attest to the bulk-like electronic properties and high quality of Pt thin films grown using this novel approach.

8.4 RuO_2 Growth

To show this technique does not only apply to simple metals like Pt, thin films of the metallic binary oxide RuO_2 were grown using $Ru(acac)_3$ with a source temperature of only 100°C. Epitaxial and phase-pure films were obtained at the low substrate temperatures of 300°C – 400°C on TiO_2 (110) and TiO_2 (101) substrates. HRXRD patterns seen in Figure 8.5a and 8.5b show the single (110) or (101) orientation, respectively, for the RuO_2 films grown at 300°C, with a thickness of 12 nm and 16 nm, respectively, obtained from the finite-thickness fringes.

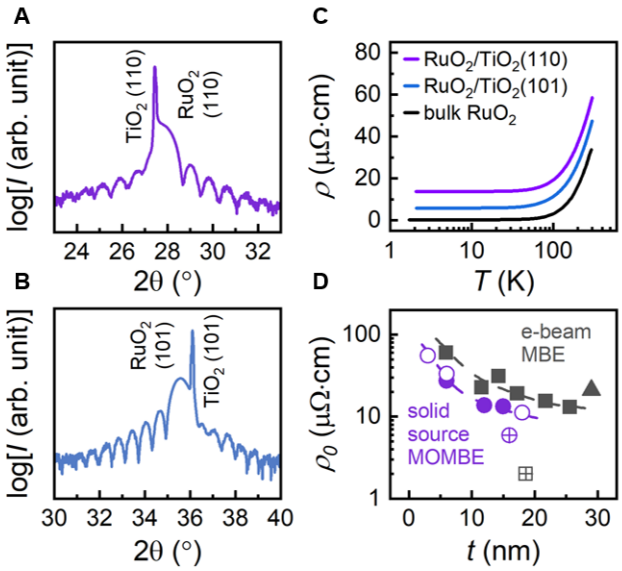

Figure 8.5. HRXRD of (a) 12 nm RuO_2 film grown on TiO_2 (110) and (b) 16 nm RuO_2 film on TiO_2 (101) substrates. (c) Resistivity of (a) and (b) compared to the bulk. (d) Residual resistivity of RuO_2 films grown with two different $Ru(acac)_3$ precursor purities (open circles = 97% and closed circles = 99.99%) compared to recent e-beam MBE reports by Ruf *et al.*[245] (squares) and Uchida *et al.*[265] (triangle). Single reports on TiO_2 (101) shown as open symbols with cross.

Streaky RHEED patterns, Figure 8.6, were seen along with atomic steps from AFM for films grown on TiO_2 (110), once again displaying the atomically-smooth films this growth process allows for. Temperature-dependent resistivity measurements as shown in Figure 8.5c indicate metallic behavior and resistivities approaching that of bulk RuO_2, with a lower resistivity for films grown on TiO_2 (101). The 16 nm film on TiO_2 (101) shown here had $\rho_0 = 6$ μΩ·cm and $RRR = 8$.

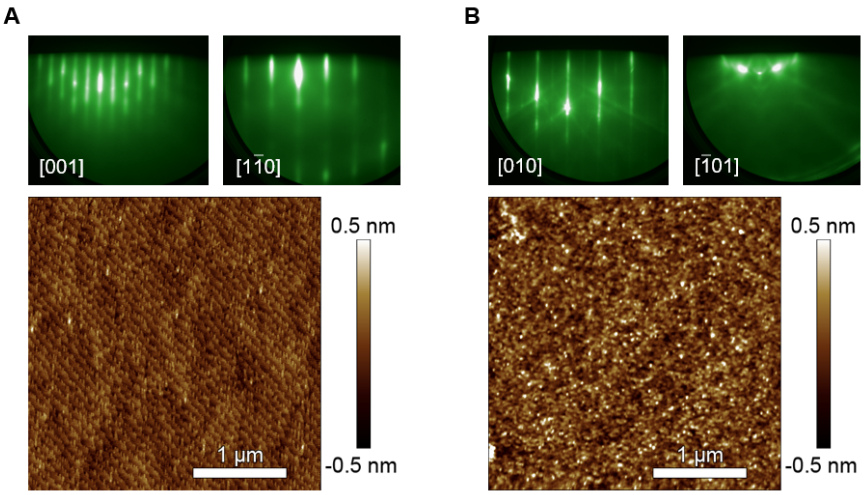

Figure 8.6. RHEED and AFM images for (a) 6 nm RuO_2 film grown on TiO_2 (110) substrate and (b) 16 nm RuO_2 film grown on TiO_2 (101) substrate. RHEED was taken down the film crystallographic direction notified in the bottom left of the respective images.

As a function of thickness, RuO_2 films grown on TiO_2 (110) revealed a decreasing resistivity with increasing thickness, a common result for thin metallic films which is likely due to finite size effects such as defects at the film/substrate interface or film's surface. As film thickness was increased beyond 18 nm, a large anisotropy occurred between the resistance along the [001] and [1$\bar{1}$0] directions, making four-terminal resistivity measurements difficult. The reason for this anisotropy is likely due to cracking of the film under tensile strain, as was observed in the previous report.[245] Although both RuO_2 and TiO_2 have the rutile crystal structure, there is a large lattice mismatch of +2.3% in the [1$\bar{1}$0] direction, causing a significant tensile strain on RuO_2. Regardless, RuO_2/ TiO_2 (110) showed record-low residual resistivities, comparable to recently reported e-beam MBE grown films,[245,265] with values approaching 13 μΩ·cm (Figure 8.5d). However, it is

recognized that a small difference in the residual resistivities is likely due to the difference in the epitaxial strain.

8.5 $SrRuO_3$ Growth

Finally, applying the solid source MOMBE technique to more complex materials, $SrRuO_3$ thin films were grown on $SrTiO_3$ (001) substrates. At a substrate temperature of 665°C and, again, a $Ru(acac)_3$ cell temperature of only 100°C, phase pure and epitaxial films were obtained. In Figure 8.7a the HRXRD pattern of a 16 nm film can be seen with a single film peak and finite-thickness fringes. Reciprocal space maps around the (103) peak showed a coherently strained film at this thickness consistent with the fully-strained orthorhombic phase.

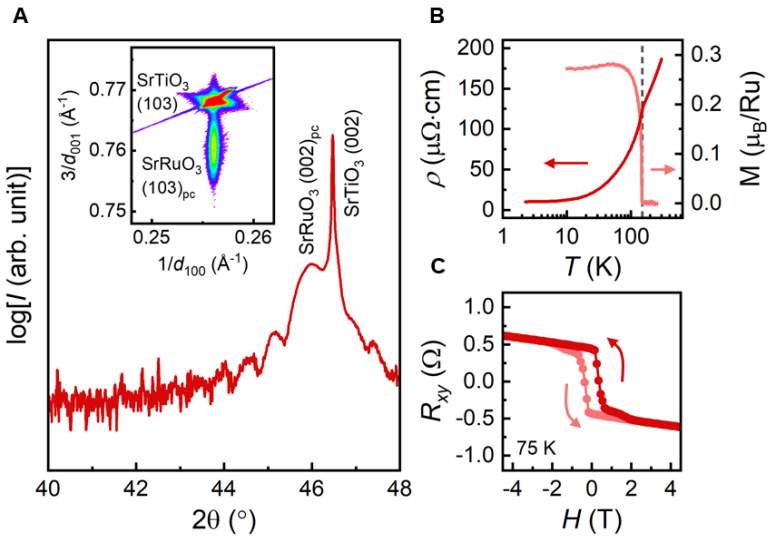

Figure 8.7. (a) HRXRD of $SrRuO_3$ film grown on $SrTiO_3$ (001) substrate. RSM of (103) peak shown in inset. (b) Resistivity-temperature on the left axis and magnetic moment-temperature under zero magnetic field on the right axis of the same $SrRuO_3$ film. Dashed line at 149 K marks the onset of ferromagnetism. (c) Total Hall resistance at 75 K with arrows signifying the field sweep direction, forward and then reverse.

Metallic behavior was present for the entire low temperature range (1.8 – 300 K) in this $SrRuO_3$ film with a discontinuity in the slope occurring at 149 K, Figure 8.7b, around the temperature (~ 160 K in bulk) where ferromagnetism is expected to appear.[254] The onset of ferromagnetism was confirmed by a non-zero magnetic moment below 149 K, Figure 8.7b, and a well-defined ferromagnetic hysteresis loop below this temperature, for example seen in Figure 8.8 at 75 K. The saturation magnetization of ~ 0.36 μ_B/Ru achieved on cooling in a magnetic field of 2 T, Figure 8.8, along the in-plane [100] azimuth of the substrate is comparable to previously reported values from $SrRuO_3$ films.[266] The ordinary and anomalous Hall effect were also present, as expected, and can be seen in the hysteretic Hall resistance as a function of applied magnetic field at 75 K in Figure 8.7c. Comparing to $SrRuO_3$ films grown by PVD techniques, the *RRR* of 18 obtained here is larger than any reported PLD-grown[267] or sputtered films,[268] but not quite as large as the highest reported MBE films[269] or bulk single crystals.[270] As these films were grown with a precursor purity of only 97%, it is believed there is still room for improvement with further growth optimization and by decreasing point defects with a higher purity starting material.

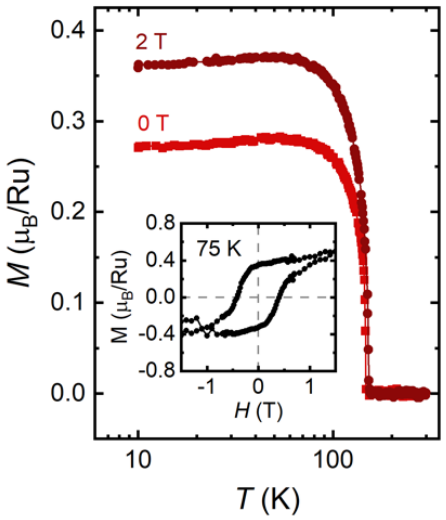

Figure 8.8. Magnetic moment-temperature of 16 nm $SrRuO_3$ film grown on $SrTiO_3$ (001) under zero magnetic field and under a 2 T field cooling along the [100] substrate direction (2T FC). Inset shows magnetic moment-magnetic field at 75 K.

8.6 Outlook

The ability to synthesize atomically controlled materials continues to drive modern technology and fundamental study. Andre Geim and Kostya Novoselov were awarded the 2010 Nobel Prize in Physics "for groundbreaking work regarding the two-dimensional material graphene". It was the simplicity of exfoliation as a synthesis method that made it possible for them and for a wide scientific community to access this material experimentally. This aspect of their exfoliation approach has resulted in the exponential rise in the work involving graphene with over two hundred thousand publications so far. To put the potential broader impact of the solid source MOMBE approach into a context, the number of publications is shown Figure 8.9a (blue bars) on different materials containing Pt, Ru, Ir, or W. A large number of publications exceeding 10's of thousands

highlights their relevance for both fundamental study and technological applications. In contrast, however, only few thousands are relevant to thin films (green bars) and, even more surprisingly, there only few 10's of them are on films grown using MBE approach. This statistic therefore clearly illustrates a large gap between materials demand and the current capability to synthesize them in an atomically-controlled fashion. The difference is recognized as due to these materials containing elements with ultra-low vapor pressures.

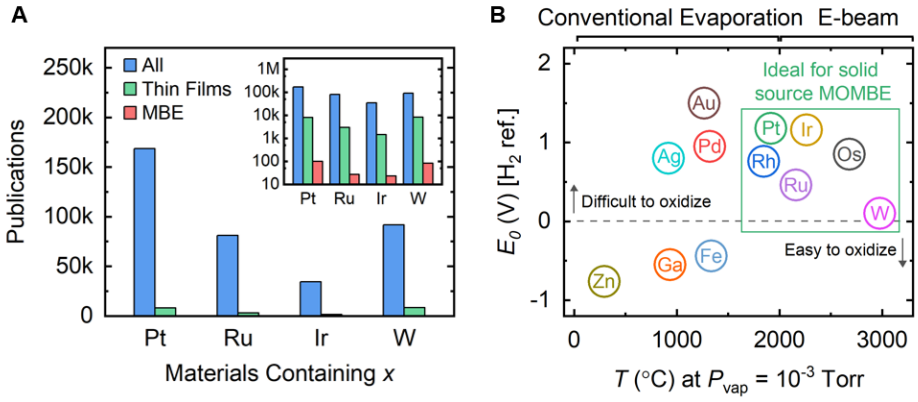

Figure 8.9. (a) Number of publications (to-date) for materials containing select elements such as Pt, Ru, Ir, and W illustrating a large gap between their importance and the current ability to synthesize them in thin-film form. Blue bars represent all the publications on the topic involving materials containing Pt, Ru, Ir, and W, green bars represent the number of publications on thin films containing Pt, Ru, Ir, and W, and red bars represent the number of publications on the topic of MBE-grown films containing Pt, Ru, Ir, and W. Inset shows the same plot on the log-y scale. (b) Standard reduction potential (E_0) using a H_2 reference electrode for select metals plotted against the temperature at which their vapor pressure is 10^{-3} Torr[248]. Boxed elements represent ideal candidates for solid source MOMBE due to their ultra-low vapor pressure and low oxidation potential.

Furthermore, many of these low vapor pressure elements also possess low oxidation potential (or high reduction potential), which makes their oxidation non-trivial, especially in low pressure PVD techniques. Figure 8.9b shows reduction potential (E_0) of these select elements as a function of temperature at which their vapor pressure is 10^{-3} Torr, i.e. suitable

for their MBE growth. The solid source MOMBE technique therefore aims to close this publication gap by allowing for low temperature sublimation (at $T < 100°C$) instead of the extremely high temperatures (typically 2000°C – 3000°C) in e-beam evaporation along with the added benefits of their pre-oxidized state in the metal-organic precursor. As an example of the latter, growth of epitaxial RuO_2 and $SrRuO_3$ was shown, where Ru in its pre-oxidized 3+ state in $Ru(acac)_3$ can be oxidized to the desired 4+ state using oxygen plasma, a weaker oxidant than ozone which is typically used.

Finally, by being such a low temperature process, the complexity and cost of supplying the metal is decreased while maintaining the quality common to MBE-grown materials. For example, keeping in mind that there are differences in substrates and thicknesses, Figure 8.10 shows *RRR* reports for Pt films grown by PVD techniques. The solid source MOMBE-grown Pt film has the largest *RRR* while only requiring relatively inexpensive and simple low-temperature sublimation compared to the process of sputtering a Pt target, controlling an electron beam for evaporation, or managing a laser in PLD. Larger *RRR* values are believed to be easily achieved using this technique by increasing the purity of the source materials as the ones used here were only 97% pure and the source purity can greatly affect the residual resistivity.

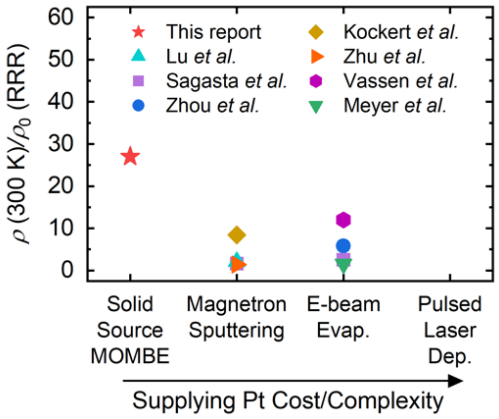

Figure 8.10. Residual resistivity ratio (*RRR*) of Pt thin films from this report compared to literature reports from e-beam evaporation and magnetron sputtering PVD techniques.[251,271-276] To the best of our knowledge, there are no reports of *RRR* for PLD Pt films.

In summary, the novel solid source MOMBE approach developed here is a unique route to supply "stubborn" metals such as Pt or Ru at operating temperatures less than 100°C which can be achieved in a low-temperature effusion cell as opposed to the several thousand °C needed using e-beam evaporators. To illustrate the capability of the SSMOMBE approach, the growth of single crystalline Pt and RuO_2 films was demonstrated as well as the more complex $SrRuO_3$ films, all containing an ultra-low vapor pressure metal. Pt films with record high RRR value were achieved whereas RuO_2 films revealed a record-low residual resistivity attesting to the ability of this approach to grow highly perfect materials in atomically-controlled fashion. Likewise, $SrRuO_3$ films with only 97% pure Ru precursor yielded a RRR value of 18, which is already higher than those grown using PLD and sputtering approaches. It is argued that the solid source MOMBE approach may potentially open up new PVD pathways (not just MBE) for "stubborn" materials such as delafossites, iridates, tungstates containing elements that have low vapor pressures and

are hard to oxidize in low pressure PVD approaches. This approach may even be applied to any other element if desired. Although not limited to the acetylacetonates tested in this work, a large amount of these metal-organic precursors do exist and are commercially available, as seen in Figure 8.11.

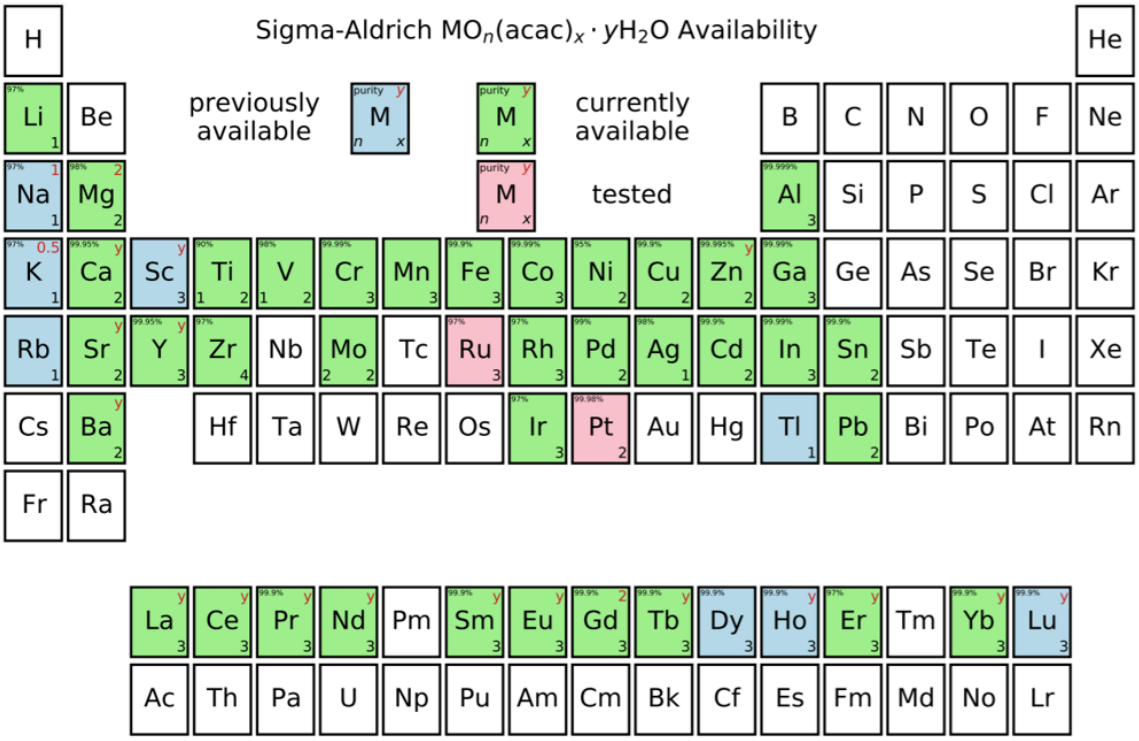

Figure 8.11. The considerable amount of metal-organic acetylacetonates which are (green), or have been (blue), commercially available by Sigma-Aldrich. The ones tested here, for Ru and Pt, are shown in red.

Chapter 9

9. Highly Conducting Epitaxial RuO_2

Building upon the previous chapter, here, additional work on the growth of RuO_2 epitaxial thin films using the solid source MOMBE technique is reported. The effect of growth temperature, thickness, and choice of substrate on the structure and electrical properties of films will be discussed.

9.1 RuO_2 Background

RuO_2 has gained considerable attention for the rich material properties it exhibits. High thermal conductivity, strong resistance to chemicals, and high electrical conductivity resulted in RuO_2 being used historically in thermometers,[277] integrated circuits,[278] plasmonics,[279] and as electrodes in supercapacitors.[252,280] RuO_2 also shows excellent catalytic properties, for example being a highly active oxygen evolution reaction catalyst.[253,281]

This chapter was adapted from a yet to be published work: William Nunn, Sreejith Nair, Anusha Kamath Manjeshwar, Anil Rajapitamahuni, Hwanhui Yun, Dooyong Lee, Andre Mkhoyan, and Bharat Jalan. Solid Source Metal-Organic Molecular Beam Epitaxy of Epitaxial RuO_2 (2021).

When alloyed with metals like La, RuO_2 exhibits a decrease in thermal conductivity and therefore has been argued to be potentially useful in thermoelectric devices.[282,283] More recently, several novel phenomena have also emerged in RuO_2 films, such as itinerant antiferromagnetism, and strain-stabilized superconductivity (Figure 9.1).[245,265] Additionally, RuO_2 also serves as a precursor to the growth of more complex materials such as perovskite $SrRuO_3$ and Sr_2RuO_4, which are shown to exhibit itinerant ferromagnetism and unconventional superconductivity, respectively.

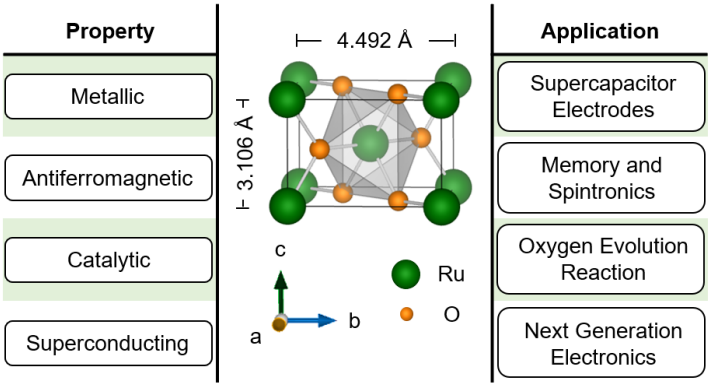

Figure 9.1. Rutile crystal structure and lattice parameters for RuO_2, the "simple" binary oxide which exhibits many different property-application relationships.

Bulk RuO_2 stabilizes in the prototypical tetragonal rutile crystal structure with space group #136, $P4_2/mnm$ and with lattice parameters $a = b = 4.492$ Å and $c = 3.106$ Å.[284] For thin films, RuO_2 has mostly been prepared as polycrystalline films[285-289] although, recently, more epitaxial crystalline preparations have been reported.[245,265,290-296] MBE is one of these thin film techniques which has been used for the growth of epitaxial single crystalline RuO_2,[245,265,290-292] however, challenges do remain in stabilizing these films in a simpler and more reproducible way. Growth of Ru-based oxides in oxide MBE is generally

challenging due to the ultra-low vapor pressure and low oxidation potential of Ru. Temperatures exceeding 2000°C are needed to achieve a suitable Ru vapor pressure for growth which is why reports of MBE-grown RuO_2 have all used electron-beam evaporators. Furthermore, the low oxidation potential makes stabilizing the Ru^{4+} in RuO_2 difficult and has led to ozone, a highly oxidizing source, being the preferred oxidant in most reports. While the use of e-beam source and ozone has facilitated synthesizing epitaxial RuO_2 or other Ru-based oxides, they possess several challenges associated with the issues related to the instability of fluxes, and source oxidation in the presence of ozone.

For these reasons, the solid source MOMBE technique for the growth of RuO_2 is expanded upon here, highlighting how this simpler, cost-effective, and safer approach is able to grow these films in a high-quality manner. An effusion cell source temperature of 100°C was used for $Ru(acac)_3$ and oxygen was supplied with a radio-frequency inductively coupled plasma source. An oxygen background pressure of ~ 10^{-6} – 10^{-5} Torr was used. Substrate temperatures were 300°C, unless stated otherwise. Films were grown on R-plane sapphire (*r*-Al_2O_3), TiO_2 (101), TiO_2 (110), TiO_2 (001), and TiO_2 (100) substrates.

9.2 Growth Temperature

Using the solid-source MOMBE approach, the effect of substrate temperature on the growth of RuO_2 was first examined. RuO_2 films were grown on *r*-Al_2O_3 with substrate temperatures (T_{sub}) from 300°C to 850°C, for a fixed growth time. All films were epitaxial and phase pure with a single peak corresponding to RuO_2 (101) orientation, the common epitaxial orientation for rutile films on *r*-Al_2O_3 as shown in the HRXRD scans in Figure

9.2a.[297] As T_{sub} was increased, the growth rate increased, Figure 9.2b, which led to differences in thickness of the films from 7 – 17 nm. As will be discussed it later, the films grown at T_{sub} = 750°C and 850°C had surfaces too rough to determine a reliable thickness using GIXR. However, an estimate of the growth rates, and therefore thicknesses, is given in Figure 9.2b, obtained from the peak broadening of (101) film peak using the Scherrer formula.[298] While the Scherrer analysis can give a poor approximation of the film thickness, thicknesses obtained here agreed well with those from GIXR and HRXRD thickness fringes for T ≤ 650 °C.

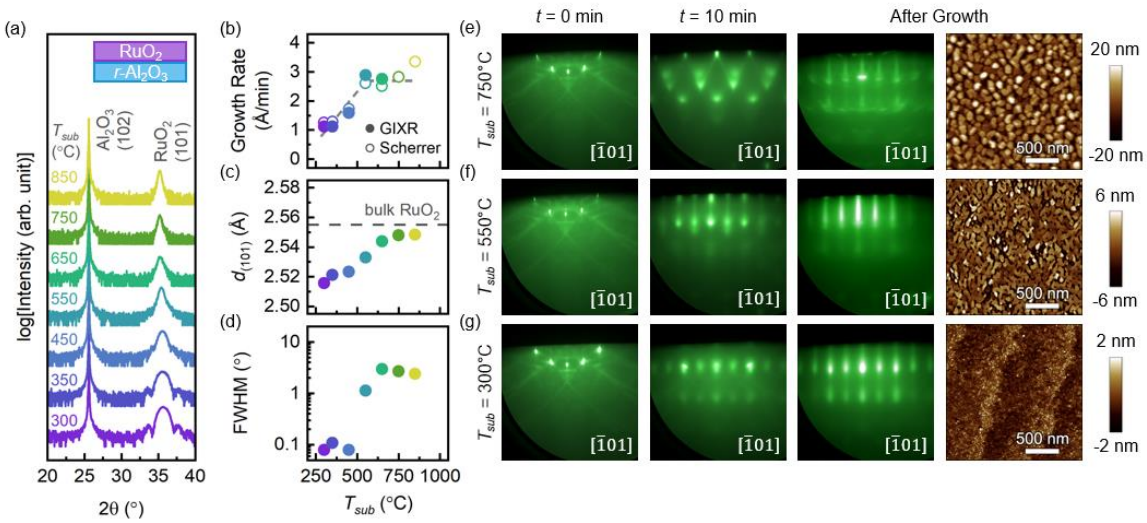

Figure 9.2. (a) HRXRD patterns for RuO_2 films grown on *r*-Al_2O_3 with increasing substrate temperature from bottom to top. (b) Out-of-plane (101) plane spacing, (c) growth rate, and (d) FWHM of the rocking curve (101) film peaks. RHEED along the film [1̄01] azimuth and AFM images before, 10 minutes into, and after growth for substrate temperature of (e) 750°C, (f) 550°C, and (g) 300°C.

The initial increase and later saturation of the growth rate with increasing T_{sub} indicates a change of growth mechanism from a reaction-limited to a flux-limited regime.[299] This suggests that below 650°C the growth rate is limited by the thermal

decomposition of the $Ru(acac)_3$ precursor. Above 650°C, the relatively constant growth rate is typical of being limited by the amount of precursor being supplied, or the flux.[299] No desorption-limited growth regime, i.e. a decrease in growth rate with increasing temperature, was observed. Nevertheless, the change from reaction- to flux-limited regime is not surprising and has been seen in other binary oxide systems grown by hybrid MBE approaches.[297,300,301]

With increasing T_{sub}, an increase in the out-of-plane spacing of (101) planes ($d_{(101)}$) was seen reaching toward the expected bulk value. The change in $d_{(101)}$ with T_{sub} is most likely due to the strain relaxation. To determine whether strain relaxation was due to the growth rate or film thickness, thicker films were grown at a constant growth rate, by keeping T_{sub} = 300°C (Figure 9.3). In this case, even as thickness was increased up to 48 nm, $d_{(101)}$ did not reach the bulk value. For instance, film thickness of 48 nm yielded $d_{(101)}$ = 2.538 ± 0.002 Å, which is significantly less than that of the 17 nm film ($d_{(101)}$ = 2.544 ± 0.002 Å) grown at higher temperatures (and at higher growth rate). This results thus suggests that the strain relaxation is more dominant effect at higher substrate temperature which is also accompanied by the higher growth rates.

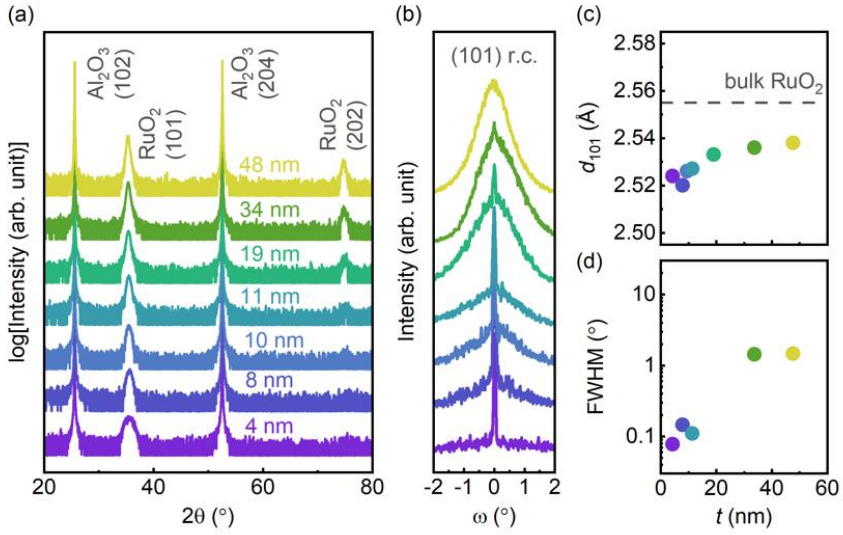

Figure 9.3. (a) HRXRD patterns and (b) (101) film rocking curves for RuO_2 films grown on *r*-Al_2O_3 at T_{sub} = 300°C with increasing thickness from bottom to top. (c) Out-of-plane (101) plane spacing and (d) FWHM of the (101) film rocking curve peak.

Consistent with strain relaxation with increasing temperature, the FWHM of the film (101) rocking curves increased by about an order of magnitude from 450°C to 550°C, as shown in Figure 9.2d. RHEED images taken before growth, 10 minutes into growth, and after growth and cool down in oxygen (T_{sub} = 200°C), as well as the post-growth AFM images, are shown in Figures 9.2e – 9.2f. From the AFM images, it can be clearly seen that the increase in FHWM was also accompanied by a roughening of the film surface. The difference in the surface morphologies was confirmed by RHEED to be a result of a change in the growth mode during growth. At 10 minutes of growth, considerable differences in the RHEED patterns can be seen for these films grown at higher temperatures, with a change to an island growth mode. Irrespective of T_{sub}, XPS confirmed Ru^{4+} valence states in these samples (Figure 9.4).

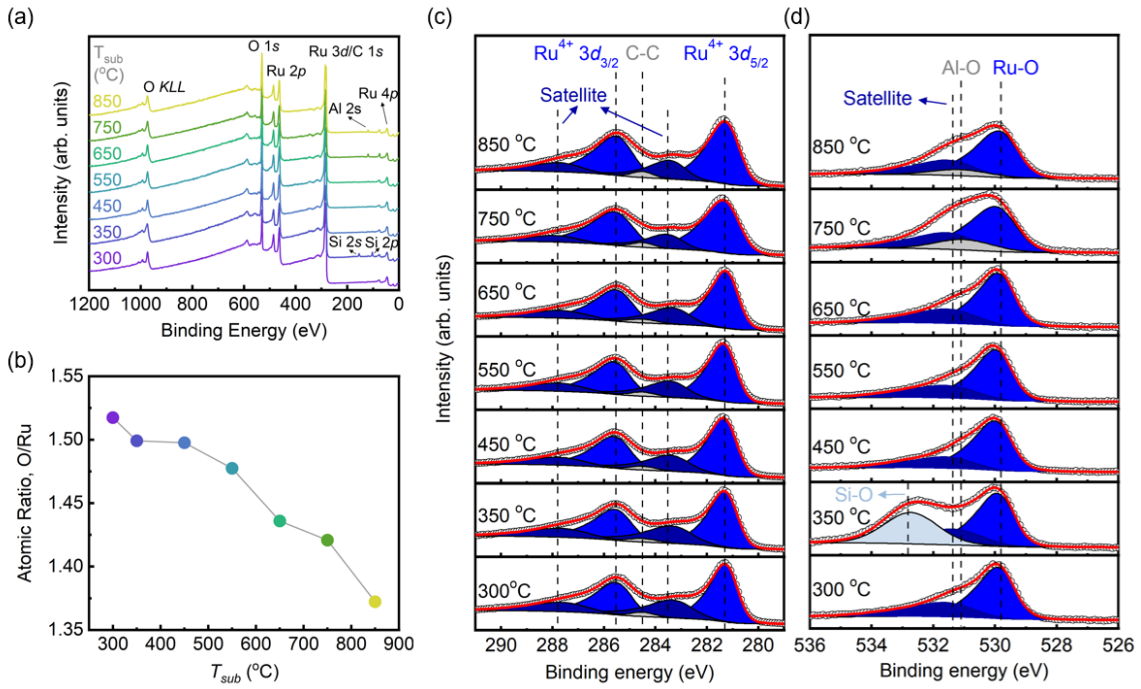

Figure 9.4. (a) XPS survey spectra of RuO_2 films on *r*-Al_2O_3 with different substrate temperatures. (b) Atomic ratio of O:Ru. Higher-resolution XPS spectra around (c) the Ru^{4+} and carbon peaks and (d) Ru-O peak. Al-O peak signal is seen at T_{sub} = 750°C and 850°C. Si-O peak is seen for the T_{sub} = 350°C but the source is unknown, most likely from accidental contamination post-growth.

Having identified the optimal substrate temperatures of 300°C – 450°C, RuO_2 films were grown at 300°C on TiO_2 substrates with different orientations. HRXRD scans, Figure 9.5a, confirm phase pure, epitaxial, single crystalline films on all these substrates. Finite thickness fringes are present in all cases, although not very well defined in the case on TiO_2 (001), attesting to the high structural quality on a short lateral length scale. To investigate the structure of these films on an atomic scale, STEM imaging was performed on a representative RuO_2 film grown on TiO_2 (101) along $[\bar{1}01]$ and [010] zone axes. Consistent with the HRXRD data, phase pure, epitaxial film is seen with a sharp film/substrate interface with no misfit dislocations. The lack of dislocations signifies

coherent growth, which agrees well with the strained d_{101} = 2.51 ± 0.002 Å obtained from HRXRD. EDX elemental maps further attest to a uniform distribution of Ru in the film.

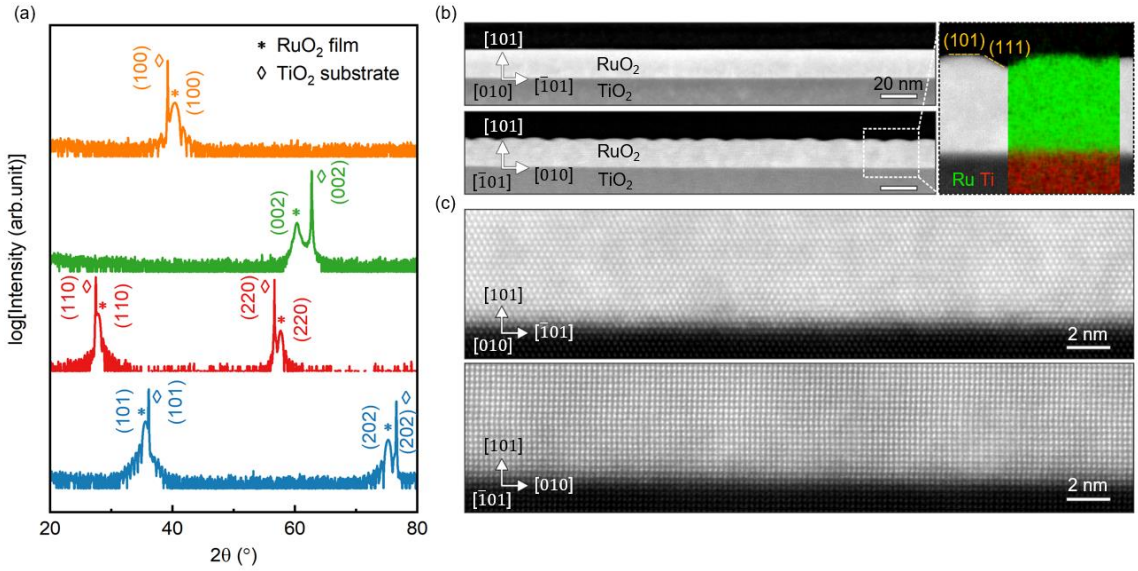

Figure 9.5. (a) HRXRD patterns of RuO_2 films grown on a variety of TiO_2 substrate orientations, (101), (110), (001), and (100) from bottom to top. Film thicknesses are 16 nm, 12 nm, 20 nm, and 10 nm, from bottom to top. (b) Cross-sectional HAADF-STEM image of 16 nm RuO_2 thin films grown on TiO_2 (101) in the [010] (top) and [$\bar{1}$01] (bottom) directions and STEM-EDX (energy dispersion X-ray) elemental map. The EDX map was constructed using Ru L_α and Ti K_α edges. (c) Atomic-resolution HAADF-STEM images of the RuO_2-TiO_2 interface.

Interestingly, STEM images also reveal an atomically smooth surface along the [010] zone axis whereas a significantly rougher morphology was observed when viewed along [$\bar{1}$01] zone axis (Figure 9.5b). As shown in the zoom-in image of Figure 9.5b, the rough surface was found to be terminated not only at the expected (101) plane parallel to the (101) TiO_2 substrate but also other plane consistent with (111) face. While the origin of this unusual surface morphology is unclear, and remains a subject of future study, it is

argued that it may be related to the significantly different strain mismatch of +0.04% and +2.3%, along [$\bar{1}$01] and [010] direction, respectively.

9.3 Film Thickness

As a next step, the strain relaxation behavior of RuO_2 film/TiO_2 (110) was investigated with thickness from 3 - 26 nm. Theoretically, RuO_2 on TiO_2 (110) has a relatively large lattice mismatch of about - 4.7% and + 2.3% along the [001] and [1$\bar{1}$0] directions, respectively, indicating coherently strained growth may be challenging on TiO_2 (110). Figure 9.6a shows HRXRD scans revealing thickness fringes and film (110) peaks being partially overlapped with that of the substrate. The well-defined Kiessig fringes again attest to the high-quality film on a short lateral length scale.

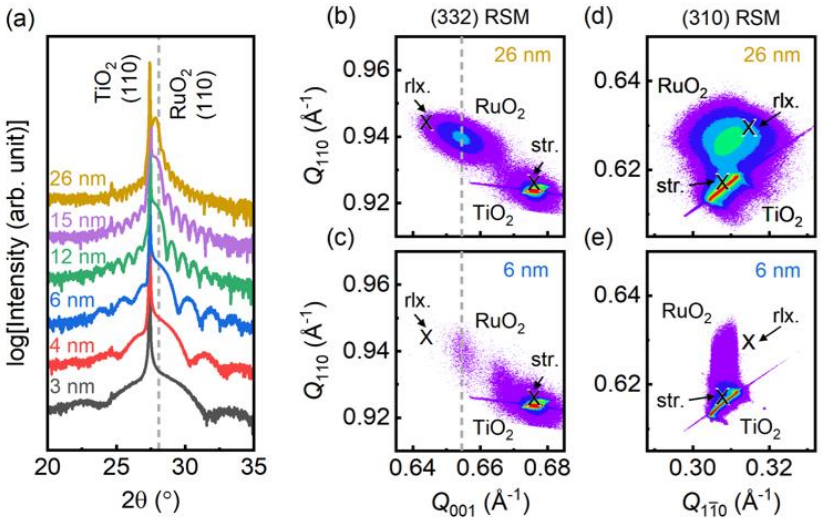

Figure 9.6. (a) HRXRD patterns of RuO_2 films grown on TiO_2 (110) substrates with increasing thickness, from bottom to top. (332) RSM for (b) 26 nm and (c) 6 nm film. (310) RSM for (d) 26 nm and (e) 6 nm film.

Upon analysis of the film peak position, 26 nm RuO_2 film/TiO_2 (110) yielded $d_{(110)}$ = 3.204 ± 0.002 Å, which is larger than the bulk value of 3.176 Å suggesting partially strained films. To examine the strain state of these films along in-plane [001] and $[1\bar{1}0]$ directions, RSMs were taken. Figures 9.6b – 9.6e show RSMs around (332) and (310) reflections for two representative films with t = 6 nm and 26 nm. As was expected based on the value of $d_{(110)}$, the 26 nm sample was partially relaxed with both in-plane spacings, along the [001] and $[1\bar{1}0]$ directions, falling between the expected fully strained and fully relaxed values Figures 9.6b and 9.6d. Interestingly, the 6 nm sample showed the same in-plane spacing as the 26 nm sample along the [001] direction (the $[1\bar{1}0]$ direction could not be determined due to overlap with the substrate). These results suggest the strain relaxation begins to occur at t as small as 6 nm or less for film grown on TiO_2 (110).

Consistent with the strain-relaxation behavior, a broadening of the (220) RuO_2 film rocking curve was also seen with increasing thickness. Figures 9.7a and 9.7b show the rocking curves of 26 nm and 6 nm film, respectively. Rocking curves were fitted using two Gaussian peaks, marked as a broad and a narrow peak. The results of this fitting are shown in Figure 9.7c and 9.7d for all thicknesses. Figure 9.7c shows the narrow peak remained at a relatively constant FWHM of ~ 0.07° while the broad peak FWHM decreased. Taking the ratio of the peak intensity of the broad component (I_{broad}) to the total intensity of the two ($I_{total} = I_{broad} + I_{narrow}$), Figure 9.7d, revealed an almost linear increase in this ratio with increasing film thickness. Results from the identical analysis RuO_2 film/r-Al_2O_3 are also included in Figure 9.7d, which compare well with films grown on TiO_2 (110) substrates.

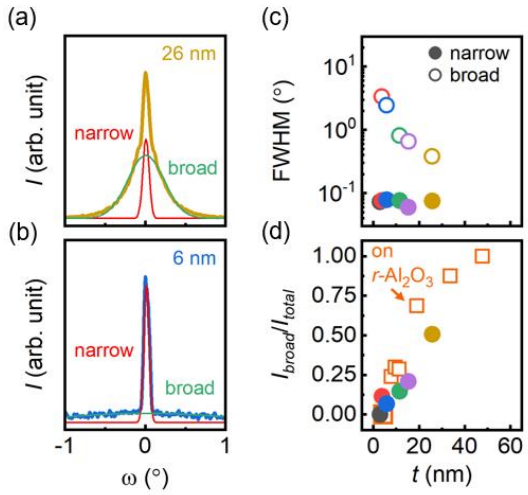

Figure 9.7. RuO_2 film (220) rocking curves for (a) 26 nm and (b) 6 nm film grown on TiO_2 (110). Gaussian fits are shown for the "narrow" and "broad" peaks. (c) FWHM of the narrow and broad fits and (d) intensity ratio of broad peak intensity to total intensity for (220) film peaks.

The origin of the broad component can be thought of as being caused by the disorder induced due to the strain relaxation. The strain relaxation process was shown to have begun by at least 6 nm based on the RSM results and likely at an even smaller thickness because of the presence of the broad component in the rocking curves of those films as well. As thickness is increased, the volume fraction of film that was influenced by the relaxation increases and, therefore, the intensity of the broad component does as well. Similar results were seen in films grown on *r*-Al_2O_3, however, with a faster increase in the intensity ratio with increasing *t*. This observation is again consistent with faster strain relaxation expected from a larger lattice-mismatch and difference in symmetry between RuO_2 and *r*-Al_2O_3.

9.4 Electronic Properties

Finally, the discussion is turned to the electrical properties of these films revealing a clear correlation between film thickness, strain relaxation, and electrical resistivity. Figure 9.8a shows the temperature-dependent ρ for RuO_2 film/TiO_2 (110) with thicknesses 3 - 15 nm. Films with thickness greater than 15 nm showed a large resistance anisotropy between the two in-plane directions for reliable four-terminal resistivity measurements, which is consistent with the prior results.[245] All films showed metallic behavior with increasing resistivity with decreasing thickness. The room-temperature ρ of 15 nm was 56 μΩ·cm, closest to the 35 μΩ·cm of bulk RuO_2 among the films grown on TiO_2 (110).[302] Figure 9.8b shows the residual resistivities ($\rho_0 = \rho$ at 1.8 K) revealing an exponential-like decrease with increasing thickness, saturating at ~ 13 μΩ·cm.

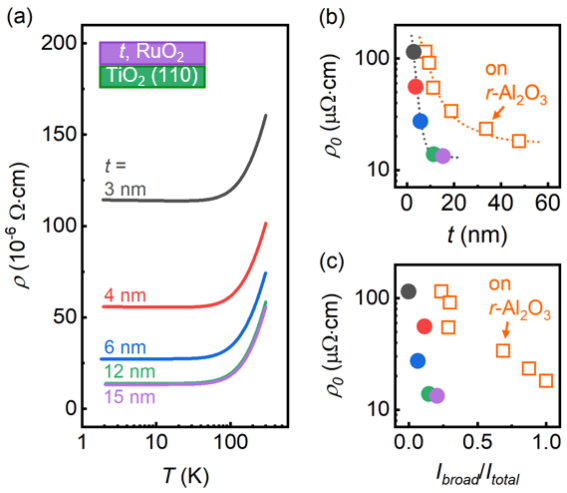

Figure 9.8. (a) Resistivity vs temperature from RuO_2 films grown on TiO_2 (110). Residual resistivity, taken at 1.8 K, for RuO_2 grown on TiO_2 (110) (filled circles) and on r-Al_2O_3 (open squares) vs (a) film thickness and (b) intensity ratio of broad peak intensity to total intensity for (220) film peaks.

Increasing film thickness can influence the electronic properties by way of finite size effects, such as effects from the film-substrate interface, dimensionality, as well as the defects arising from the strain relaxation process, such as misfit and/or threading dislocations. With regards to the latter, as strain relaxation occurs and more defects are formed, the residual resistivity should likely increase as it is generally dependent on these structural crystalline defects. Here the opposite trend was seen, implying the increase in thickness has a much larger effect on ρ than strain relaxation-related defect formation. To this end, a plot of ρ_0 vs. the film rocking curve intensity ratio, that was defined earlier, is shown in Figure 9.8c. This shows, once again, the opposite trend of what should be seen if strain relaxation was the critical factor. These data establish an important role of film dimensionality on the electrical transport properties of RuO_2 films.

In summary, the growth of epitaxial RuO_2 films has been shown with different orientations using different substrates by a novel solid-source MOMBE. Single crystalline films with low film rocking curve FWHMs were grown on *r*-Al_2O_3 with substrate temperatures between 300°C - 450°C. At higher temperatures, films showed a significant increase in structural disorder. Using this approach and by keeping substrate temperature of 300°C, films were then grown on TiO_2 substrates with different orientations. STEM results confirmed phase pure, epitaxial films free of strain-relaxation-related defects when grown on TiO_2 (101). However, films on TiO_2 (110) were found to relax at thickness as low as 6 nm. Films with resistivity similar to that of the bulk RuO_2 single crystals was obtained for 15 nm RuO_2/TiO_2 (110). Finally, with increasing film thickness, an important role of film thickness on electrical properties was revealed. This work establishes the solid-

source MOMBE technique for the growth of high-quality RuO_2 in a much simpler, and cost-effective manner when compared to conventional MBE approaches. For instance, Ru metal was supplied by subliming a solid metal-organic precursor, $Ru(acac)_3$ in a low temperature effusion cell operating at 100°C as opposed to several thousand using e-beam in conventional MBE.

Chapter 10

10. Summary and Outlook

Synthesizing ferroelectric films in a high-quality manner and optimizing device properties based on overall heterostructure design has been the focus of much work for many decades, dating back to the discovery of ferroelectric perovskite oxides in the 1940's. Ferroelectric materials have since been used in a large array of practical devices. While much progress has been made, many challenges exist for the design and growth of ferroelectric materials and their heterostructures. The ability to reproducibly synthesize these structures with precise composition, thickness, and controlled structure is essential for fundamental study and industrial production. Molecular beam epitaxy is thin film technique that has proven able to produce some of the highest quality films, dating back to its inception for the growth of III-V semiconductors with atomic layer control. Although many advancements have been made within the technique, challenges remain for the growth of complex materials like ferroelectric perovskite oxides. Control over the structure and composition such as avoiding non-stoichiometric related defects and taking advantage of epitaxial-strain engineering are constant sources of investigation.

Here, the more recently developed hybrid MBE has been used for the thin film growth of dielectric and ferroelectric perovskite oxides. Hybrid MBE is an exciting metal-organic-based modification of conventional techniques that has shown great control over cation stoichiometry and the resulting structure for many complex oxides. Taking advantage of these capabilities, the entire $BaTiO_3$-$BaSnO_3$ alloy system was grown and studied for the first time in MBE.

Epitaxial, single crystalline BTO films were grown with evidence of an "MBE growth window", or a range of cation flux ratios within which there is adsorption-controlled self-regulating stoichiometry. Although out-of-plane lattice parameters differed within this window, films show a constant unit cell volume, low FWHM, and identical surface morphologies and reconstruction. At larger film thicknesses, a close to bulk-like first-order phase transition was observed based on the change in both the *a*- and *c*-axis lattice parameters, important for ferroelectric energy conversion applications. Based on this work, hybrid MBE has been shown to have exceptional control over the stoichiometry, strain state, and the resulting properties. Although BTO films were grown on a conducting Nb-doped STO substrate, ferroelectric measurements proved inconclusive due to extrinsic effects of the metallic electrodes.

The dielectric response in BSO was investigated, a material which had previously been grown with considerable success by hybrid MBE. A dielectric constant of 15 was obtained, irrespective of film thickness, cation stoichiometry, and dislocation density. However, stoichiometric films exhibited the lowest dielectric loss, attesting to the importance of cation stoichiometry control in this material. DFT simulations were used and

proved useful in determining the likely defect complexes to form when BSO is grown off its stoichiometric condition.

With the hybrid MBE growth and characterization completed of the two end members in this alloy system of interest, samples were grown spanning the entire BTSO composition range. Great control over the B-site composition was achieved and could be reliably predicted simply from the growth conditions. Significant structural disorder was imparted on the material with increasing Sn incorporation into the BTO structure. However, a maximum in the polarization based on SHG was found at $x = 0.09$, agreeing well with ceramic studies. This material system is a promising alternative to lead-based ferroelectrics.

Finally, in an effort to address the obstacle of *in-situ* MBE growth of desirable metallic electrodes like Pt or $SrRuO_3$, a novel synthesis approach was conceived and developed: *solid source metal-organic MBE*. Many materials which contain "stubborn" elements, those which have ultra-low vapor pressures and/or low oxidation potentials, are difficult to deposit in evaporation techniques but useful for a variety of applications. Utilizing a solid metal-organic precursor in a low-temperature effusion placed directly in the vacuum system, deposition of Pt, RuO_2, and $SrRuO_3$ was shown with source temperatures less than 100°C for the Pt or Ru precursors. Single crystalline films with high figures of merit were achieved but in a much simpler, cost-effective, and safer manner than conventional MBE approaches, like electron-beam evaporation.

This work has aimed to highlight many of the challenges involved with the MBE growth of complex materials as well as the design and production of ferroelectric

heterostructures. Combining the hybrid MBE approaches with the solid source metal-organic MBE innovation, it should now be possible to grow high-quality, completely *in-situ*-grown ferroelectric heterostructures using some of the most effective metallic electrodes. Future work should now be aimed at the growth of these all-epitaxial heterostructures and the development of new leading lead-free ferroelectrics for applications such as energy conversion and storage.

References

1 Ramesh, R., Aggarwal, S. & Auciello, O. Science and technology of ferroelectric films and heterostructures for non-volatile ferroelectric memories. *Mater. Sci. Eng. R Rep.* **32**, 191-236, (2001).

2 Zhang, H. *et al.* Review on the Development of Lead-free Ferroelectric Energy-Storage Ceramics and Multilayer Capacitors. *J. Mater. Chem. C*, (2020).

3 Yang, L. *et al.* Perovskite lead-free dielectrics for energy storage applications. *Prog. Mater. Sci.* **102**, 72-108, (2019).

4 Zhao, P. *et al.* High-performance relaxor ferroelectric materials for energy storage applications. *Adv. Energy Mater.* **9**, 1803048, (2019).

5 Bucsek, A. N., Nunn, W., Jalan, B. & James, R. D. Energy Conversion by Phase Transformation in the Small-Temperature-Difference Regime. *Annu. Rev. Mater. Res.* **50**, 283-318, (2020).

6 Bucsek, A., Nunn, W., Jalan, B. & James, R. D. Direct Conversion of Heat to Electricity Using First-Order Phase Transformations in Ferroelectrics. *Phys. Rev. Appl.* **12**, (2019).

7 Martin, L. W. & Rappe, A. M. Thin-film ferroelectric materials and their applications. *Nat. Rev. Mater.* **2**, 1-14, (2016).

8 Bokov, A. & Ye, Z.-G. Recent progress in relaxor ferroelectrics with perovskite structure. *J. Adv. Dielectr.*, 105-164, (2020).

9 Dawber, M., Rabe, K. & Scott, J. Physics of thin-film ferroelectric oxides. *Rev. Mod. Phys.* **77**, 1083, (2005).

10 Rödel, J. *et al.* Perspective on the development of lead-free piezoceramics. *J. Am. Ceram. Soc.* **92**, 1153-1177, (2009).

11 Hong, C.-H. *et al.* Lead-free piezoceramics–Where to move on? *J. Materiomics* **2**, 1-24, (2016).

12 Saito, Y. *et al.* Lead-free piezoceramics. *Nature* **432**, 84-87, (2004).

13 Stengel, M. & Spaldin, N. A. Origin of the dielectric dead layer in nanoscale capacitors. *Nature* **443**, 679-682, (2006).

14 Zhou, C. & Newns, D. Intrinsic dead layer effect and the performance of ferroelectric thin film capacitors. *J. Appl. Phys.* **82**, 3081-3088, (1997).

15 Pena, M. & Fierro, J. Chemical structures and performance of perovskite oxides. *Chem. Rev.* **101**, 1981-2018, (2001).

16 Brahlek, M. *et al.* Frontiers in the growth of complex oxide thin films: past, present, and future of hybrid MBE. *Adv. Funct. Mater.* **28**, 1702772, (2018).

17 MacManus-Driscoll, J. *et al.* New approaches for achieving more perfect transition metal oxide thin films. *APL Mater.* **8**, 040904, (2020).

18 Bjaalie, L., Himmetoglu, B., Weston, L., Janotti, A. & Van de Walle, C. Oxide interfaces for novel electronic applications. *New J. Phys.* **16**, 025005, (2014).

19 Bhalla, A., Guo, R. & Roy, R. The perovskite structure—a review of its role in ceramic science and technology. *Mater. Res. Innov.* **4**, 3-26, (2000).

20 Schlom, D. G. Perspective: Oxide molecular-beam epitaxy rocks! *APL Mater.* **3**, 062403, (2015).

21 Prakash, A. & Jalan, B. Wide Bandgap Perovskite Oxides with High Room-Temperature Electron Mobility. *Adv. Mater. Interfaces* **6**, 1900479, (2019).

22 Sleight, A. W., Gillson, J. & Bierstedt, P. High-temperature superconductivity in the $BaPb_{1-x}Bi_xO_3$ system. *Solid State Commun.* **88**, 841-842, (1993).

23 Raveau, B., Maignan, A., Martin, C. & Hervieu, M. Colossal magnetoresistance manganite perovskites: relations between crystal chemistry and properties. *Chem. Mater.* **10**, 2641-2652, (1998).

24 Setter, N. *et al.* Ferroelectric thin films: Review of materials, properties, and applications. *J. Appl. Phys.* **100**, 051606, (2006).

25 Cohen, R. E. Origin of ferroelectricity in perovskite oxides. *Nature* **358**, 136-138, (1992).

26 Wang, J. *et al.* Epitaxial $BiFeO_3$ multiferroic thin film heterostructures. *Science* **299**, 1719-1722, (2003).

27 Goldschmidt, V. M. Die gesetze der krystallochemie. *Naturwissenschaften* **14**, 477-485, (1926).

28 Glazer, A. Simple ways of determining perovskite structures. *Acta Crystallogr., Sect. A: Found. Crystallogr.* **31**, 756-762, (1975).

29 Raymond, M. & Smyth, D. Defects and charge transport in perovskite ferroelectrics. *J. Phys. Chem. Solids* **57**, 1507-1511, (1996).

30 Nagaraj, B., Aggarwal, S., Song, T., Sawhney, T. & Ramesh, R. Leakage current mechanisms in lead-based thin-film ferroelectric capacitors. *Phys. Rev. B* **59**, 16022, (1999).

31 Chan, N. H., Sharma, R. & Smyth, D. M. Nonstoichiometry in $SrTiO_3$. *J. Electrochem. Soc.* **128**, 1762, (1981).

32 Schooley, J., Hosler, W. & Cohen, M. L. Superconductivity in Semiconducting $SrTiO_3$. *Phys. Rev. Lett.* **12**, 474, (1964).

33 Potzger, K. *et al.* Defect-induced ferromagnetism in crystalline $SrTiO_3$. *J. Magn. Magn. Mater.* **323**, 1551-1562, (2011).

34 Lee, D. *et al.* Emergence of room-temperature ferroelectricity at reduced dimensions. *Science* **349**, 1314-1317, (2015).

35 Klyukin, K. & Alexandrov, V. Effect of intrinsic point defects on ferroelectric polarization behavior of $SrTiO_3$. *Phys. Rev. B* **95**, 035301, (2017).

36 Li, W., Shi, J., Zhang, K. H. & MacManus-Driscoll, J. L. Defects in complex oxide thin films for electronics and energy applications: challenges and opportunities. *Mater. Horiz.* **7**, 2832-2859, (2020).

37 Sakayori, K.-i. *et al.* Curie temperature of $BaTiO_3$. *Jpn. J. Appl. Phys.* **34**, 5443, (1995).

38 Kay, H. Preparation and properties of crystals of barium titanate, $BaTiO_3$. *Acta Crystallogr.* **1**, 229-237, (1948).

39 Kingon, A. I., Maria, J.-P. & Streiffer, S. Alternative dielectrics to silicon dioxide for memory and logic devices. *Nature* **406**, 1032-1038, (2000).

40 Abel, S. *et al.* A strong electro-optically active lead-free ferroelectric integrated on silicon. *Nature Commun.* **4**, 1-6, (2013).

41 Zhang, S. & Li, F. High performance ferroelectric relaxor-$PbTiO_3$ single crystals: Status and perspective. *J. Appl. Phys.* **111**, 2, (2012).

42 Bellaiche, L., García, A. & Vanderbilt, D. Finite-temperature properties of $Pb(Zr_{1-x}Ti_x)O_3$ alloys from first principles. *Phys. Rev. Lett.* **84**, 5427, (2000).

43 Guo, R. *et al.* Origin of the high piezoelectric response in $PbZr_{1-x}Ti_xO_3$. *Phys. Rev. Lett.* **84**, 5423, (2000).

44 Noheda, B., Cox, D., Shirane, G., Gao, J. & Ye, Z.-G. Phase diagram of the ferroelectric relaxor $(1-x)PbMg_{1/3}Nb_{2/3}O_3-xPbTiO_3$. *Phys. Rev. B* **66**, 054104, (2002).

45 Jaffe, B., Roth, R. & Marzullo, S. Piezoelectric properties of lead zirconate-lead titanate solid-solution ceramics. *J. Appl. Phys.* **25**, 809-810, (1954).

46 Rao, B. N. & Ranjan, R. Electric-field-driven monoclinic-to-rhombohedral transformation in $Na_{1/2}Bi_{1/2}TiO_3$. *Phys. Rev. B.* **86**, 134103, (2012).

47 Zhang, S.-T., Kounga, A. B., Aulbach, E., Ehrenberg, H. & Rödel, J. Giant strain in lead-free piezoceramics $Bi_{0.5}Na_{0.5}TiO_3–BaTiO_3–K_{0.5}Na_{0.5}NO_3$ system. *Appl. Phys. Lett.* **91**, 112906, (2007).

48 Liu, W. & Ren, X. Large piezoelectric effect in Pb-free ceramics. *Phys. Rev. Lett.* **103**, 257602, (2009).

49 Garg, R., Rao, B. N., Senyshyn, A., Krishna, P. & Ranjan, R. Lead-free piezoelectric system $(Na_{0.5}Bi_{0.5})TiO_3$-$BaTiO_3$: Equilibrium structures and irreversible structural transformations driven by electric field and mechanical impact. *Phys. Rev. B* **88**, 014103, (2013).

50 Jo, W., Granzow, T., Aulbach, E., Rödel, J. & Damjanovic, D. Origin of the large strain response in $(K_{0.5}Na_{0.5})NbO_3$-modified $(Bi_{0.5}Na_{0.5})TiO_3–BaTiO_3$ lead-free piezoceramics. *J. Appl. Phys.* **105**, 094102, (2009).

51 Catalan, G. & Scott, J. F. Physics and applications of bismuth ferrite. *Adv. Mater.* **21**, 2463-2485, (2009).

52 Horikawa, T. *et al.* Dielectric properties of $(Ba,Sr)TiO_3$ thin films deposited by RF sputtering. *Jpn. J. Appl. Phys.* **32**, 4126, (1993).

53 Mikheev, E., Kajdos, A. P., Hauser, A. J. & Stemmer, S. Electric field-tunable $Ba_xSr_{1-x}TiO_3$ films with high figures of merit grown by molecular beam epitaxy. *Appl. Phys. Lett.* **101**, 252906, (2012).

54 Bethe, K. & Welz, F. Preparation and properties of $(Ba,Sr)TiO_3$ single crystals. *Mater. Res. Bull.* **6**, 209-217, (1971).

55 Ezhilvalavan, S. & Tseng, T.-Y. Progress in the developments of $(Ba,Sr)TiO_3$ (BST) thin films for Gigabit era DRAMs. *Mater. Chem. Phys.* **65**, 227-248, (2000).

56 Lei, C., Bokov, A. A. & Ye, Z.-G. Ferroelectric to relaxor crossover and dielectric phase diagram in the $BaTiO_3–BaSnO_3$ system. *J. Appl. Phys.* **101**, 084105, (2007).

57 Xue, D. *et al.* Large piezoelectric effect in Pb-free $Ba(Ti,Sn)O_3$-$x(Ba,Ca)TiO_3$ ceramics. *Appl. Phys. Lett.* **99**, 122901, (2011).

58 Yao, Y. *et al.* Large piezoelectricity and dielectric permittivity in $BaTiO_3$-$xBaSnO_3$ system: The role of phase coexisting. *Europhys. Lett.* **98**, 27008, (2012).

59 Maiti, T., Guo, R. & Bhalla, A. Electric field dependent dielectric properties and high tunability of $BaZr_xTi_{1-x}O_3$ relaxor ferroelectrics. *Appl. Phys. Lett.* **89**, 122909, (2006).

60 Yu, Z., Ang, C., Guo, R. & Bhalla, A. Ferroelectric-relaxor behavior of $Ba(Ti_{0.7}Zr_{0.3})O_3$ ceramics. *J. Appl. Phys.* **92**, 2655-2657, (2002).

61 Maiti, T., Guo, R. & Bhalla, A. Structure-property phase diagram of $BaZr_xTi_{1-x}O_3$ system. *J. Am. Ceram. Soc.* **91**, 1769-1780, (2008).

62 Li, M.-D. *et al.* Large Electrocaloric Effect in Lead-free $Ba(Hf_xTi_{1-x})O_3$ Ferroelectric Ceramics for Clean Energy Applications. *ACS Sustain. Chem. Eng.* **6**, 8920-8925, (2018).

63 Kalyani, A. K., Brajesh, K., Senyshyn, A. & Ranjan, R. Orthorhombic-tetragonal phase coexistence and enhanced piezo-response at room temperature in Zr, Sn, and Hf modified $BaTiO_3$. *Appl. Phys. Lett.* **104**, 252906, (2014).

64 Tian, H., Wang, Y., Miao, J., Chan, H. & Choy, C. Preparation and characterization of hafnium doped barium titanate ceramics. *J. Alloys Compd.* **431**, 197-202, (2007).

65 Kalyani, A. K., Krishnan, H., Sen, A., Senyshyn, A. & Ranjan, R. Polarization switching and high piezoelectric response in Sn-modified $BaTiO_3$. *Phys. Rev. B* **91**, 024101, (2015).

66 Alpay, S., Misirlioglu, I., Nagarajan, V. & Ramesh, R. Can interface dislocations degrade ferroelectric properties? *Appl. Phys. Lett.* **85**, 2044-2046, (2004).

67 Choi, K. J. *et al.* Enhancement of ferroelectricity in strained $BaTiO_3$ thin films. *Science* **306**, 1005-1009, (2004).

68 Haeni, J. H. *et al.* Room-temperature ferroelectricity in strained $SrTiO_3$. *Nature* **430**, 758-761, (2004).

69 Chu, Y. H. *et al.* Domain control in multiferroic $BiFeO_3$ through substrate vicinality. *Adv. Mater.* **19**, 2662-2666, (2007).

70 Chu, Y. H. *et al.* Nanoscale domain control in multiferroic $BiFeO_3$ thin films. *Adv. Mater.* **18**, 2307-2311, (2006).

71 Chu, Y.-H. *et al.* Nanoscale control of domain architectures in $BiFeO_3$ thin films. *Nano Lett.* **9**, 1726-1730, (2009).

72 Fong, D. *et al.* Stabilization of monodomain polarization in ultrathin $PbTiO_3$ films. *Phys. Rev. Lett.* **96**, 127601, (2006).

73 Baiutti, F., Christiani, G. & Logvenov, G. Towards precise defect control in layered oxide structures by using oxide molecular beam epitaxy. *Beilstein J. Nanotechnol.* **5**, 596-602, (2014).

74 Greene, J. E. Tracing the recorded history of thin-film sputter deposition: From the 1800s to 2017. *J. Vac. Sci. Technol. A* **35**, 05C204, (2017).

75 Grove, W. R. On the electro-chemical polarity of gases. *Philos. Trans. R. Soc. Lond.*, 87-101, (1852).

76 Faraday, M. Experimental relations of gold (and other metals) to light. *Philos. Trans. R. Soc. Lond.*, 145-181, (1857).

77 Smith, H. M. & Turner, A. Vacuum deposited thin films using a ruby laser. *Appl. Opt.* **4**, 147-148, (1965).

78 Ganguly, P. & Rao, C. Crystal chemistry and magnetic properties of layered metal oxides possessing the K_2NiF_4 or related structures. *J. Solid State Chem.* **53**, 193-216, (1984).

79 Bednorz, J. G. & Müller, K. A. Possible high T_c superconductivity in the Ba−La−Cu−O system. *Z. Phys. B* **64**, 189-193, (1986).

80 Dijkkamp, D. *et al.* Preparation of Y-Ba-Cu oxide superconductor thin films using pulsed laser evaporation from high T_c bulk material. *Appl. Phys. Lett.* **51**, 619-621, (1987).

81 Wu, M.-K. *et al.* Superconductivity at 93 K in a new mixed-phase Y-Ba-Cu-O compound system at ambient pressure. *Phys. Rev. Lett.* **58**, 908, (1987).

82 Arthur, J. R. Interaction of Ga and As_2 molecular beams with GaAs surfaces. *J. Appl. Phys.* **39**, 4032-4034, (1968).

83 Cho, A. Y. & Arthur, J. R. Molecular beam epitaxy. *Prog. Solid. State Ch.* **10**, 157-191, (1975).

84 McCray, W. P. MBE deserves a place in the history books. *Nat. Nanotechnol.* **2**, 259-261, (2007).

85 Michel, P. F. Coating by cathode disintegration. U.S. patent 2,146,025 (7 Feb. 1939).

86 Jalan, B., Engel-Herbert, R., Wright, N. J. & Stemmer, S. Growth of high-quality $SrTiO_3$ films using a hybrid molecular beam epitaxy approach. *J. Vac. Sci. Technol. A* **27**, 461-464, (2009).

87 Nunn, W. *et al.* Novel Synthesis Approach for "Stubborn" Metals and Metal Oxides. Unpublished manuscript, (2021).

88 Eom, C.-b. & Lee, J. Metal-organic pulsed laser deposition for stoichiometric complex oxide thin films. U. S. patent 10,796,907 (6 Oct. 2020).

89 Dingle, R., Störmer, H., Gossard, A. & Wiegmann, W. Electron mobilities in modulation-doped semiconductor heterojunction superlattices. *Appl. Phys. Lett.* **33**, 665-667, (1978).

90 Stormer, H. L. Nobel lecture: the fractional quantum Hall effect. *Rev. Mod. Phys.* **71**, 875, (1999).

91 Smith, D. L. & Pickhardt, V. Y. Molecular beam epitaxy of II-VI compounds. *J. Appl. Phys.* **46**, 2366-2374, (1975).

92 Yoshida, S. *et al.* Reactive molecular beam epitaxy of aluminium nitride. *J. Vac. Sci. Technol.* **16**, 990-993, (1979).

93 Koma, A., Sunouchi, K. & Miyajima, T. Fabrication and characterization of heterostructures with subnanometer thickness. *Microelectron. Eng.* **2**, 129-136, (1984).

94 Betts, R. & Pitt, C. Growth of thin-film lithium niobate by molecular beam epitaxy. *Electron. Lett.* **21**, 960-962, (1985).

95 Kwo, J. *et al.* Structural and superconducting properties of orientation-ordered $Y_1Ba_2Cu_3O_{7-x}$ films prepared by molecular-beam epitaxy. *Phys. Rev. B* **36**, 4039, (1987).

96 Webb, C. *et al.* Growth of high T_c superconducting thin films using molecular beam epitaxy techniques. *Appl. Phys. Lett.* **51**, 1191-1193, (1987).

97 Berkley, D. D. *et al.* In situ formation of superconducting $YBa_2Cu_3O_{7-x}$ thin films using pure ozone vapor oxidation. *Appl. Phys. Lett.* **53**, 1973-1975, (1988).

98 Schlom, D. G. *et al.* Molecular beam epitaxial growth of layered Bi-Sr-Ca-Cu-O compounds. *J. Cryst. Growth* **102**, 361-375, (1990).

99 Segawa, Y. *et al.* Growth of ZnO thin film by laser MBE: lasing of exciton at room temperature. *Phys. Status Solidi B* **202**, 669-672, (1997).

100 Johnson, M. *et al.* MBE growth and properties of ZnO on sapphire and SiC substrates. *J. Electron. Mater.* **25**, 855-862, (1996).

101 Falson, J. *et al.* MgZnO/ZnO heterostructures with electron mobility exceeding 1×10^6 cm^2/Vs. *Sci. Rep.* **6**, 1-8, (2016).

102 Migita, S., Kasai, Y., Ota, H. & Sakai, S. Self-limiting process for the bismuth content in molecular beam epitaxial growth of $Bi_2Sr_2CuO_y$ thin films. *Appl. Phys. Lett.* **71**, 3712-3714, (1997).

103 Theis, C. D., Yeh, J., Schlom, D. G., Hawley, M. & Brown, G. Adsorption-controlled growth of $PbTiO_3$ by reactive molecular beam epitaxy. *Thin Solid Films* **325**, 107-114, (1998).

104 Theis, C. D. *et al.* Adsorption-controlled growth of $Bi_4Ti_3O_{12}$ by reactive MBE. *Appl. Phys. Lett.* **72**, 2817-2819, (1998).

105 Zhang, G. *et al.* Quintuple-layer epitaxy of thin films of topological insulator Bi_2Se_3. *Appl. Phys. Lett.* **95**, 053114, (2009).

106 Mellnik, A. *et al.* Spin-transfer torque generated by a topological insulator. *Nature* **511**, 449-451, (2014).

107 Mundy, J. A. *et al.* Atomically engineered ferroic layers yield a room-temperature magnetoelectric multiferroic. *Nature* **537**, 523-527, (2016).

108 Paik, H. *et al.* Adsorption-controlled growth of La-doped $BaSnO_3$ by molecular-beam epitaxy. *APL Mater.* **5**, 116107, (2017).

109 Prakash, A. *et al.* Wide bandgap $BaSnO_3$ films with room temperature conductivity exceeding 10^4 S cm^{-1}. *Nat. Commun.* **8**, 1-9, (2017).

110 Matias, V. & Hammond, R. H. Ion beam induced crystalline texturing during thin film deposition. *Surf. Coat. Technol.* **264**, 1-8, (2015).

111 Ohnishi, T., Shibuya, K., Yamamoto, T. & Lippmaa, M. Defects and transport in complex oxide thin films. *J. Appl. Phys.* **103**, 103703, (2008).

112 Dobkin, D. M. & Zaraw, M. K. *Principles of Chemical Vapor Deposition*. (Springer, 2003).

113 Haeni, J. *et al.* Epitaxial growth of the first five members of the $Sr_{n+1}Ti_nO_{3n+1}$ Ruddlesden–Popper homologous series. *Appl. Phys. Lett.* **78**, 3292-3294, (2001).

114 Tian, W. *et al.* Epitaxial growth and magnetic properties of the first five members of the layered $Sr_{n+1}Ru_nO_{3n+1}$ oxide series. *Appl. Phys. Lett.* **90**, 022507, (2007).

115 Lee, C.-H. *et al.* Exploiting dimensionality and defect mitigation to create tunable microwave dielectrics. *Nature* **502**, 532-536, (2013).

116 Haislmaier, R. C., Stone, G., Alem, N. & Engel-Herbert, R. Creating Ruddlesden-Popper phases by hybrid molecular beam epitaxy. *Appl. Phys. Lett.* **109**, 043102, (2016).

117 Barone, M. R. *et al.* Improved control of atomic layering in perovskite-related homologous series. *APL Mater.* **9**, 021118, (2021).

118 Lee, C.-H. *et al.* Effect of reduced dimensionality on the optical band gap of $SrTiO_3$. *Appl. Phys. Lett.* **102**, 122901, (2013).

119 Nie, Y. F. *et al.* Atomically precise interfaces from non-stoichiometric deposition. *Nat. Commun.* **5**, 4530, (2014).

120 Poppe, U. *et al.* Direct production of crystalline superconducting thin films of $YBa_2Cu_3O_7$ by high-pressure oxygen sputtering. *Solid State Commun.* **66**, 661-665, (1988).

121 Guarino, A., Patimo, G., Vecchione, A., Di Luccio, T. & Nigro, A. Fabrication of superconducting $Nd_{2-x}Ce_xCuO_{4\pm\delta}$ films by automated DC sputtering technique. *Physica C: Superconductivity* **495**, 146-152, (2013).

122 Schmitz, M. *et al.* Strain and electric field control of magnetism in $La_{1-x}Sr_xMnO_3$ thin films on ferroelectric $BaTiO_3$ substrates. *New J. Phys.* **22**, 053018, (2020).

123 Rodríguez Contreras, J. *et al.* Improved $PbZr_{0.52}Ti_{0.48}O_3$ film quality on $SrRuO_3/SrTiO_3$ substrates. *J. Cryst. Growth* **277**, 210-217, (2005).

124 Feijoo, P. C., Pampillón, M. A., San Andrés, E. & Fierro, J. L. G. Nano-laminate vs. direct deposition of high permittivity gadolinium scandate on silicon by high pressure sputtering. *Thin Solid Films* **593**, 62-66, (2015).

125 Petraru, A. *et al.* Polarization and lattice strains in epitaxial $BaTiO_3$ films grown by high-pressure sputtering. *J. of Appl. Phys.* **101**, 114106, (2007).

126 Ambwani, P. *et al.* Defects, stoichiometry, and electronic transport in $SrTiO_{3-\delta}$ epilayers: A high pressure oxygen sputter deposition study. *J. Appl. Phys.* **120**, 055704, (2016).

127 Ganguly, K. *et al.* Structure and transport in high pressure oxygen sputter-deposited $BaSnO_{3-\delta}$. *APL Mater.* **3**, 062509, (2015).

128 Postiglione, W. M. *et al.* Structure-property relationships and mobility optimization in sputtered La-doped $BaSnO_3$ films: Toward 100 $cm^2V^{-1}s^{-1}$ mobility. *Phys. Rev. Mater.* **5**, 044604, (2021).

129 Zhang, R. *et al.* One-step epitaxy of high-mobility La-doped $BaSnO_3$ films by high-pressure magnetron sputtering. *APL Mater.* **9**, 061103, (2021).

130 Zheng, C. X. *et al.* Mapping the surface phase diagram of GaAs(001) using droplet epitaxy. *Phys. Rev. Mater.* **3**, 124603, (2019).

131 Watanabe, Y. *et al.* Portable ultrahigh-vacuum sample storage system for polarization-dependent total-reflection fluorescence x-ray absorption fine structure spectroscopy. *J. Vac. Sci. Technol. A* **34**, 023201, (2015).

132 Klausmeier-Brown, M., Eckstein, J., Bozovic, I. & Virshup, G. Accurate measurement of atomic beam flux by pseudo-double-beam atomic absorption spectroscopy for growth of thin-film oxide superconductors. *Appl. Phys. Lett.* **60**, 657-659, (1992).

133 Lu, C., Lightner, M. J. & Gogol, C. A. Rate controlling and composition analysis of alloy deposition processes by electron impact emission spectroscopy (EIES). *J. Vac. Sci. Technol.* **14**, 103-107, (1977).

134 Yamamoto, H., Aoki, K., Tsukada, A. & Naito, M. Growth of $Ba_{1-x}K_xBiO_3$ thin films by molecular beam epitaxy. *Physica C: Superconductivity* **412-414**, 192-195, (2004).

135 Lu, C., Blissett, C. D. & Diehl, G. An electron impact emission spectroscopy flux sensor for monitoring deposition rate at high background gas pressure with improved accuracy. *J. Vac. Sci. Technol. A* **26**, 956-960, (2008).

136 Haeni, J., Theis, C. D. & Schlom, D. G. RHEED intensity oscillations for the stoichiometric growth of $SrTiO_3$ thin films by reactive molecular beam epitaxy. *J. Electroceram.* **4**, 385-391, (2000).

137 Schlom, D. *et al.* Oxide nano-engineering using MBE. *Mater. Sci. Eng., B* **87**, 282-291, (2001).

138 Kubiak, R. A. *et al.* Improved flux control from the Sentinel III electron impact emission spectroscopy system. *J. Vac. Sci. Technol. A* **9**, 2423-2425, (1991).

139 Jalan, B., Moetakef, P. & Stemmer, S. Molecular beam epitaxy of $SrTiO_3$ with a growth window. *Appl. Phys. Lett.* **95**, 032906, (2009).

140 Theis, C. D. & Schlom, D. G. Epitaxial lead titanate grown by MBE. *J. Cryst. Growth* **174**, 473-479, (1997).

141 Theis, C. D. & Schlom, D. G. Cheap and stable titanium source for use in oxide molecular beam epitaxy systems. *J. Vac. Sci. Technol. A* **14**, 2677-2679, (1996).

142 Kim, Y. S., Bansal, N., Chaparro, C., Gross, H. & Oh, S. Sr flux stability against oxidation in oxide-molecular-beam-epitaxy environment: Flux, geometry, and pressure dependence. *J. Vac. Sci. Technol. A* **28**, 271-276, (2010).

143 Cain, T. A., Kajdos, A. P. & Stemmer, S. La-doped $SrTiO_3$ films with large cryogenic thermoelectric power factors. *Appl. Phys. Lett.* **102**, 182101, (2013).

144 Kozuka, Y., Hikita, Y., Bell, C. & Hwang, H. Dramatic mobility enhancements in doped $SrTiO_3$ thin films by defect management. *Appl. Phys. Lett.* **97**, 012107, (2010).

145 Matsubara, Y., Takahashi, K. S., Tokura, Y. & Kawasaki, M. Single-crystalline $BaTiO_3$ films grown by gas-source molecular beam epitaxy. *Appl. Phys. Express* **7**, 125502, (2014).

146 Moetakef, P., Zhang, J. Y., Raghavan, S., Kajdos, A. P. & Stemmer, S. Growth window and effect of substrate symmetry in hybrid molecular beam epitaxy of a Mott insulating rare earth titanate. *J. Vac. Sci. Technol. A* **31**, 041503, (2013).

147 Raghavan, S., Zhang, J. Y., Shoron, O. F. & Stemmer, S. Probing the metal-insulator transition in $BaTiO_3$ by electrostatic doping. *Phys. Rev. Lett.* **117**, 037602, (2016).

148 Moyer, J. A., Eaton, C. & Engel-Herbert, R. Highly conductive $SrVO_3$ as a bottom electrode for functional perovskite oxides. *Adv. Mater.* **25**, 3578-3582, (2013).

149 Prakash, A. *et al.* Hybrid molecular beam epitaxy for the growth of stoichiometric $BaSnO_3$. *J. Vac. Sci. Technol. A* **33**, 060608, (2015).

150 Wang, T. *et al.* Defect-driven localization crossovers in MBE-grown La-doped $SrSnO_3$ films. *Phys. Rev. Mater.* **1**, 061601, (2017).

151 Prakash, A. *et al.* Adsorption-controlled growth and the influence of stoichiometry on electronic transport in hybrid molecular beam epitaxy-grown $BaSnO_3$ films. *J. Mater. Chem. C* **5**, 5730-5736, (2017).

152 Braun, W. *et al. In situ* thermal preparation of oxide surfaces. *APL Mater.* **8**, 071112, (2020).

153 Rumble, J. R. *CRC handbook of chemistry and physics*. Vol. 101 (CRC Press/Taylor & Francis Group, 2020).

154 Tufte, O. & Chapman, P. Electron mobility in semiconducting strontium titanate. *Phys. Rev.* **155**, 796, (1967).

155 Muller, D. A., Nakagawa, N., Ohtomo, A., Grazul, J. L. & Hwang, H. Y. Atomic-scale imaging of nanoengineered oxygen vacancy profiles in $SrTiO_3$. *Nature* **430**, 657-661, (2004).

156 Yang, H., Wang, Y., Wang, H. & Jia, Q. Oxygen concentration and its effect on the leakage current in $BiFeO_3$ thin films. *Appl. Phys. Lett.* **96**, 012909, (2010).

157 Raghavan, S. *et al.* High-mobility $BaSnO_3$ grown by oxide molecular beam epitaxy. *APL Mater.* **4**, 016106, (2016).

158 Ganguly, K., Prakash, A., Jalan, B. & Leighton, C. Mobility-electron density relation probed via controlled oxygen vacancy doping in epitaxial $BaSnO_3$. *APL Mater.* **5**, 056102, (2017).

159 Schlom, D. G. & Harris, J. S. in *Molecular Beam Epitaxy - Applications to Key Materials* (ed R. F. C. Farrow) Ch. 6, 505-622 (Noyes, Park Ridge, 1995).

160 Schlom, D. *et al.* Molecular beam epitaxy of layered Dy-Ba-Cu-O compounds. *Appl. Phys. Lett.* **53**, 1660-1662, (1988).

161 Locquet, J. P. & Mächler, E. Characterization of a radio frequency plasma source for molecular beam epitaxial growth of high-T_c superconductor films. *J. Vac. Sci. Technol. A* **10**, 3100-3103, (1992).

162 Chambers, S. A. Epitaxial growth and properties of thin film oxides. *Surf. Sci. Rep.* **39**, 105-180, (2000).

163 Gao, Y. & Chambers, S. A. Heteroepitaxial growth of α-Fe_2O_3, γ-Fe_2O_3 and Fe_3O_4 thin films by oxygen-plasma-assisted molecular beam epitaxy. *J. Cryst. Growth* **174**, 446-454, (1997).

164 Lind, D., Berry, S., Chern, G., Mathias, H. & Testardi, L. Growth and structural characterization of Fe_3O_4 and NiO thin films and superlattices grown by oxygen-plasma-assisted molecular-beam epitaxy. *Phys. Rev. B* **45**, 1838, (1992).

165 Materer, N., Goodman, R. S. & Leone, S. R. Comparison of electron cyclotron resonance and radio-frequency inductively coupled plasmas of Ar and N_2: Neutral kinetic energies and source gas cracking. *J. Appl. Phys.* **83**, 1917-1923, (1998).

166 Sakurai, K., Iwata, D., Fujita, S. & Fujita, S. Growth of ZnO by Molecular Beam Epitaxy Using NO_2 as Oxygen Source. *Jpn. J. Appl. Phys.* **38**, 2606-2608, (1999).

167 Izyumskaya, N. *et al.* Molecular beam epitaxy of high-quality ZnO using hydrogen peroxide as an oxidant. *J. Cryst. Growth* **269**, 356-361, (2004).

168 Schumann, T., Raghavan, S., Ahadi, K., Kim, H. & Stemmer, S. Structure and optical band gaps of (Ba,Sr)SnO_3 films grown by molecular beam epitaxy. *J. Vac. Sci. Technol. A.* **34**, 050601, (2016).

169 Zhang, L. & Engel-Herbert, R. Growth of $SrTiO_3$ on Si (001) by hybrid molecular beam epitaxy. *Phys. Status Solidi RRL* **8**, 917-923, (2014).

170 Truttmann, T., Prakash, A., Yue, J., Mates, T. E. & Jalan, B. Dopant solubility and charge compensation in La-doped $SrSnO_3$ films. *Appl. Phys. Lett.* **115**, 152103, (2019).

171 Truttmann, T. K., Liu, F., Garcia-Barriocanal, J., James, R. D. & Jalan, B. Strain Relaxation via Phase Transformation in High-Mobility $SrSnO_3$ Films. *ACS Appl. Electron. Mater.* **3**, 1127-1132, (2021).

172 Wang, T. *et al.* Engineering $SrSnO_3$ phases and electron mobility at room temperature using epitaxial strain. *ACS Appl. Mater. Interfaces* **10**, 43802-43808, (2018).

173 Hellman, E. S. & Hartford, E. H. Effects of oxygen on the sublimation of alkaline earths from effusion cells. *J. Vac. Sci. Technol. B* **12**, 1178-1180, (1994).

174 Kim, Y.-S., Bansal, N. & Oh, S. Simple self-gettering differential-pump for minimizing source oxidation in oxide-MBE environment. *J. Vac. Sci. Technol. A* **29**, 041505, (2011).

175 Kim, Y.-S., Bansal, N. & Oh, S. Crucible aperture: An effective way to reduce source oxidation in oxide molecular beam epitaxy process. *J. Vac. Sci. Technol. A* **28**, 600-602, (2010).

176 Fujita, S. Wide-bandgap semiconductor materials: For their full bloom. *Jpn. J. Appl. Phys.* **54**, 030101, (2015).

177 Braun, W. & Mannhart, J. Film deposition by thermal laser evaporation. *AIP Adv.* **9**, 085310, (2019).

178 Sadeghi, I., Ye, K., Xu, M., LeBeau, J. M. & Jaramillo, R. Making $BaZrS_3$ chalcogenide perovskite thin films by molecular beam epitaxy. arXiv:2105.10258 (2021). <https://ui.adsabs.harvard.edu/abs/2021arXiv210510258S>.

179 Brahlek, M. *et al.* Growth of metallic delafossite $PdCoO_2$ by molecular beam epitaxy. *Phys. Rev. Mater.* **3**, 093401, (2019).

180 Nie, Y. F. *et al.* Interplay of spin-orbit interactions, dimensionality, and octahedral rotations in semimetallic $SrIrO_3$. *Phys. Rev. Lett.* **114**, 016401, (2015).

181 Nair, H. P. *et al.* Synthesis science of $SrRuO_3$ and $CaRuO_3$ epitaxial films with high residual resistivity ratios. *APL Mater.* **6**, 046101, (2018).

182 Sonoda, T. *et al.* Ultra-high throughput of GaAs and (AlGa)As layers grown by MBE with a specially designed MBE system. *J. Cryst. Growth* **95**, 317-321, (1989).

183 Kushi, K. *et al.* High speed growth of device quality GaN and InGaN by RF-MBE. *Mater. Sci. Eng., B* **59**, 65-68, (1999).

184 Vogt, P. *et al.* Adsorption-controlled growth of Ga_2O_3 by suboxide molecular-beam epitaxy. *APL Mater.* **9**, 031101, (2021).

185 Lapano, J. *et al.* Scaling growth rates for perovskite oxide virtual substrates on silicon. *Nature Commun.* **10**, 1-7, (2019).

186 Nono Tchiomo, A. P. *et al.* High-temperature-grown buffer layer boosts electron mobility in epitaxial La-doped $BaSnO_3/SrZrO_3$ heterostructures. *APL Mater.* **7**, 041119, (2019).

187 Wei, M. *et al.* High electrical conducting deep-ultraviolet-transparent oxide semiconductor La-doped $SrSnO_3$ exceeding ~3000 S cm^{-1}. *Appl. Phys. Lett.* **116**, 022103, (2020).

188 Hasegawa, S. Reflection high-energy electron diffraction. *Mater. Charact.*, 1-14, (2002).

189 Mazet, L., Yang, S. M., Kalinin, S. V., Schamm-Chardon, S. & Dubourdieu, C. A review of molecular beam epitaxy of ferroelectric $BaTiO_3$ films on Si, Ge and GaAs substrates and their applications. *Sci. Technol. Adv. Mater.*, (2015).

190 Yoneda, Y. *et al.* Structural characterization of $BaTiO_3$ thin films grown by molecular beam epitaxy. *J. Appl. Phys.* **83**, 2458-2461, (1998).

191 Cheng, J. *et al.* High-current perovskite oxide $BaTiO_3/BaSnO_3$ heterostructure field effect transistors. *IEEE Electron Device Lett.* **41**, 621-624, (2020).

192 LeBeau, J. M., D'Alfonso, A. J., Wright, N. J., Allen, L. J. & Stemmer, S. Determining ferroelectric polarity at the nanoscale. *Appl. Phys. Lett.* **98**, 052904, (2011).

193 Shoron, O. F., Raghavan, S., Freeze, C. R. & Stemmer, S. $BaTiO_3/SrTiO_3$ heterostructures for ferroelectric field effect transistors. *Appl. Phys. Lett.* **110**, 232902, (2017).

194 Sang, X. H. & LeBeau, J. M. Revolving scanning transmission electron microscopy: Correcting sample drift distortion without prior knowledge. *Ultramicroscopy* **138**, 28-35, (2014).

195 Niu, G. *et al.* Molecular beam epitaxy growth of $BaTiO_3$ thin films and crucial impact of oxygen content conditions on the electrical characteristics. *Thin Solid Films* **520**, 4595-4599, (2012).

196 Bechmann, R. Elastic, piezoelectric, and dielectric constants of polarized barium titanate ceramics and some applications of the piezoelectric equations. *J. Acoust. Soc. Am.* **28**, 347-350, (1956).

197 Vaithyanathan, V. *et al.* c-axis oriented epitaxial $BaTiO_3$ films on (001) Si. *J. Appl. Phys.* **100**, 024108, (2006).

198 Kazaoui, S., Ravez, J., Elissalde, C. & Maglione, M. High frequency dielectric relaxation in $BaTiO_3$ derived materials. *Ferroelectrics* **135**, 85-99, (1992).

199 Merz, W. J. The Electric and Optical Behavior of $BaTiO_3$ Single-Domain Crystals. *Phys. Rev.* **76**, 1221, (1949).

200 Li, Y., Hu, S., Liu, Z. & Chen, L. Effect of electrical boundary conditions on ferroelectric domain structures in thin films. *Appl. Phys. Lett.* **81**, 427-429, (2002).

201 Wang, T., Ganguly, K., Marshall, P., Xu, P. & Jalan, B. Critical thickness and strain relaxation in molecular beam epitaxy-grown $SrTiO_3$ films. *Appl. Phys. Lett.* **103**, 212904, (2013).

202 Beigi, S. I., Walker, F. J., Cheong, S. W., Rabe, K. M. & Ahn, C. H. Alkaline earth stannates: The next silicon? *APL Mater.* **3**, 062510, (2015).

203 Kim, H. J. *et al.* High mobility in a stable transparent perovskite oxide. *Appl. Phys. Express* **5**, 061102, (2012).

204 Kim, H. J. *et al.* Physical properties of transparent perovskite oxides $(Ba,La)SnO_3$ with high electrical mobility at room temperature. *Phys. Rev. B* **86**, 165205, (2012).

205 Luo, X. *et al.* High carrier mobility in transparent $Ba_{1-x}La_xSnO_3$ crystals with a wide band gap. *Appl. Phys. Lett.* **100**, 172112, (2012).

206 Sanchela, A. V., Onozato, T., Feng, B., Ikuhara, Y. & Ohta, H. Thermopower modulation clarification of the intrinsic effective mass in transparent oxide semiconductor $BaSnO_3$. *Phys. Rev. Mater.* **1**, 034603, (2017).

207 Krishnaswamy, K. *et al.* $BaSnO_3$ as a channel material in perovskite oxide heterostructures. *Appl. Phys. Lett.* **108**, 083501, (2016).

208 Chambers, S. A., Kaspar, T. C., Prakash, A., Haugstad, G. & Jalan, B. Band alignment at epitaxial $BaSnO_3/SrTiO_3$ (001) and $BaSnO_3/LaAlO_3$ (001) heterojunctions. *Appl. Phys. Lett.* **108**, 152104, (2016).

209 Park, C. *et al.* High mobility field effect transistor based on $BaSnO_3$ with Al_2O_3 gate oxide. *Appl. Phys. Lett.* **105**, 203503, (2014).

210 Singh, P. *et al.* Electronic structure, electrical and dielectric properties of $BaSnO_3$ below 300 K. *Jap. J. Appl. Phys.* **47**, 3540, (2008).

211 Upadhyay, S., Parkash, O. & Kumar, D. Preparation and characterization of barium stannate $BaSnO_3$. *J. Mater. Sci. Lett.* **16**, 1330, (1997).

212 Upadhyay, S. High temperature impedance spectroscopy of barium stannate, $BaSnO_3$. *Bull. Mater. Sci.* **36**, 1019, (2013).

213 Bévillon, É., Chesnaud, A., Wang, Y., Dezanneau, G. & Geneste, G. Theoretical and experimental study of the structural, dynamical and dielectric properties of perovskite $BaSnO_3$. *J. Phys.: Cond. Matt.* **20**, 145217, (2008).

214 Mun, H. *et al.* Large effects of dislocations on high mobility of epitaxial perovskite $Ba_{0.96}La_{0.04}SnO_3$ films. *Appl. Phys. Lett* **102**, 252105, (2013).

215 Wang, W. Y. *et al.* Atomic mapping of Ruddlesden- Popper faults in transparent conducting $BaSnO_3$-based thin films. *Sci. Rep.* **5**, 16097, (2015).

216 Hwang, C. S. Thickness-dependent dielectric constants of $(Ba,Sr)TiO_3$ thin films with Pt or conducting oxide electrodes. *J. Appl. Phys.* **92**, 432, (2002).

217 Yamamichi, S., Yabuta, H., Sakuma, T. & Miyasaka, Y. (Ba+ Sr)/Ti ratio dependence of the dielectric properties for $(Ba_{0.5}Sr_{0.5})TiO_3$ thin films prepared by ion beam sputtering. *Appl. Phys. Lett.* **64**, 1644, (1994).

218 Horikawa, T. *et al.* Dielectric properties of $(Ba, Sr)TiO_3$ thin films deposited by RF sputtering. *Jap. J Appl. Phys.* **32**, 4126, (1993).

219 Parker, C. B., Maria, J.-P. & Kingon, A. I. Temperature and thickness dependent permittivity of $(Ba,Sr)TiO_3$ thin films. *Appl. Phys. Lett.* **81**, 340, (2002).

220 Natori, K., Otani, D. & Sano, N. Thickness dependence of the effective dielectric constant in a thin film capacitor. *Appl. Phys. Lett.* **73**, 632, (1998).

221 Tsai, M. S. & Tseng, T. Y. Effect of bottom electrodes on dielectric relaxation and defect analysis of $(Ba_{0.47}Sr_{0.53})TiO_3$ thin film capacitors. *Mater. Chem. Phys.* **57**, 47, (1998).

222 Li, H.-C., Si, W., West, A. D. & Xi, X. Thickness dependence of dielectric loss in $SrTiO_3$ thin films. *Appl. Phys. Lett.* **73**, 464, (1998).

223 Laguta, V. V. *et al.* Paramagnetic dipole centers in $KTaO_3$: Electron-spin-resonance and dielectric spectroscopy study. *Phys. Rev. B* **61**, 3897, (2000).

224 Yu, Z., Ang, C. & Cross, L. Oxygen-vacancy-related dielectric anomalies in La: $SrTiO_3$. *Appl. Phys. Lett.* **74**, 3044, (1999).

225 Scott, J. Applications of modern ferroelectrics. *Science* **315**, 954-959, (2007).

226 Haertling, G. H. Ferroelectric ceramics: history and technology. *J. Am. Ceram. Soc.* **82**, 797-818, (1999).

227 Uchino, K. *Ferroelectric devices*. (CRC press, 2018).

228 Song, S. *et al.* Enhanced electric field tunable dielectric properties of $Ba(Sn_{0.15}Ti_{0.85})O_3$ thin films. *J. Appl. Phys.* **104**, 096107, (2008).

229 Mascot, M., Fasquelle, D. & Carru, J.-C. Very high tunability of $BaSn_xTi_{1-x}O_3$ ferroelectric thin films deposited by sol-gel. *Funct. Mater. Lett.* **4**, 49-52, (2011).

230 Huang, H.-H., Wang, M.-C., Chen, C.-Y., Wu, N.-C. & Lin, H.-J. Effect of deposition parameters on the growth rate and dielectric properties of the $Ba(Sn_xTi_{1-x})\ O_3$ thin films prepared by radio frequency magnetron sputtering. *J. Eur. Ceram.* **26**, 3211-3219, (2006).

231 Cheng, H., Hida, H., Ouyang, J. & Kanno, I. Electromechanical properties of $BaTiO_3$-x$BaSnO_3$ thin films prepared via combinatorial sputtering. *Ceram. Int.* **43**, 1597-1601, (2017).

232 Tumarkin, A. *et al.* High tunable $BaSn_xTi_{1-x}O_3$ thin films for microwave applications. *Integr. Ferroelectr.* **173**, 140-146, (2016).

233 Zhu, G., Yan, D., Xu, H. & Yu, A. Structural and electric properties of $BaSn_{0.15}Ti_{0.85}O_3$ films on ITO/glass substrate by RF sputtering from powder target. *Mater. Lett.* **140**, 155-157, (2015).

234 Gao, Q., Li, K., Zhang, K., Zhang, J. & Liu, Q. Structure and bandgap nonlinearity in $BaSn_{1-x}Ti_xO_3$ epitaxial films. *Appl. Phys. Lett.* **114**, 081901, (2019).

235 Wang, S., Lai, M. & Lu, L. Temperature-and electrode-dependent leakage current behaviour of pulsed laser deposited $Ba(Ti_{0.85}Sn_{0.15})O_3$ thin films. *J. Phys. D Appl. Phys.* **43**, 305401, (2010).

236 Denton, A. R. & Ashcroft, N. W. Vegard's law. *Phys. Rev. A* **43**, 3161, (1991).

237 Denev, S. A., Lummen, T. T., Barnes, E., Kumar, A. & Gopalan, V. Probing ferroelectrics using optical second harmonic generation. *J. Am. Ceram. Soc.* **94**, 2699-2727, (2011).

238 Xu, G., Wen, J., Stock, C. & Gehring, P. Phase instability induced by polar nanoregions in a relaxor ferroelectric system. *Nat. Mater.* **7**, 562-566, (2008).

239 Samarth, N. Quantum materials discovery from a synthesis perspective. *Nat. Mater.* **16**, 1068, (2017).

240 Gozar, A. *et al.* High-temperature interface superconductivity between metallic and insulating copper oxides. *Nature* **455**, 782-785, (2008).

241 Ohtomo, A. & Hwang, H. Y. A high-mobility electron gas at the $LaAlO_3/SrTiO_3$ heterointerface. *Nature* **427**, 423-426, (2004).

242 Thiel, S., Hammerl, G., Schmehl, A., Schneider, C. W. & Mannhart, J. Tunable quasi-two-dimensional electron gases in oxide heterostructures. *Science* **313**, 1942-1945, (2006).

243 Umansky, V. *et al.* MBE growth of ultra-low disorder 2DEG with mobility exceeding 35 x 10^6 cm^2/V s. *J. Cryst. Growth* **311**, 1658-1661, (2009).

244 Son, J. *et al.* Epitaxial $SrTiO_3$ films with electron mobilities exceeding 30,000 cm^2/Vs. *Nat. Mater.* **9**, 482, (2010).

245 Ruf, J. P. *et al.* Strain-stabilized superconductivity. *Nature Commun.* **12**, 1-8, (2021).

246 Ahadi, K. *et al.* Enhancing superconductivity in $SrTiO_3$ films with strain. *Sci Adv* **5**, eaaw0120, (2019).

247 Schlom, D. G. & Pfeiffer, L. N. "Oxide electronics: Upward mobility rocks!". *Nat. Mat.* **9**, 881, (2010).

248 Macdonald, F. & Lide, D. R. CRC handbook of chemistry and physics: From paper to web. *Abstr Pap Am Chem S* **225**, U552-U552, (2003).

249 Hiskes, R. *et al.* Single source metalorganic chemical vapor-deposition of low microwave surface-resistance $YBa_2Cu_3O_7$. *Appl. Phys. Lett.* **59**, 606-607, (1991).

250 Lu, Z. *et al.* Solid source MOCVD for the epitaxial-growth of thin oxide-films. *J. Cryst. Growth* **128**, 788-792, (1993).

251 Sagasta, E. *et al.* Tuning the spin Hall effect of Pt from the moderately dirty to the superclean regime. *Phys. Rev. B* **94**, 060412, (2016).

252 Hu, C. C., Chang, K. H., Lin, M. C. & Wu, Y. T. Design and tailoring of the nanotubular arrayed architecture of hydrous RuO_2 for next generation supercapacitors. *Nano Lett.* **6**, 2690-2695, (2006).

253 Rossmeisl, J., Qu, Z. W., Zhu, H., Kroes, G. J. & Norskov, J. K. Electrolysis of water on oxide surfaces. *J. Electroanal. Chem.* **607**, 83-89, (2007).

254 Koster, G. *et al.* Structure, physical properties, and applications of $SrRuO_3$ thin films. *Rev. Mod. Phys.* **84**, 253-298, (2012).

255 Morozova, N. B. *et al.* Vapor pressure of precursors for CVD on the base of platinum group metals. *J. phys., IV* **11**, 609-616, (2001).

256 Flanagan, S. *et al.* A design-of-experiments approach to modeling activity coefficients in solvent mixtures: a case study using platinum(II) acetylacetonate in mixtures of acetone, cyclohexanol, 1,2,3,4-tetrahydronaphthalene and propylene carbonate. *Green Chem.* **7**, 333-338, (2005).

257 Wang, W. & Zhang, L. Hydrogen transfer hydrogenation of nitrobenzene to aniline with $Ru(acac)_3$ as the catalyst. *Res. Chem. Intermed.* **40**, 3109-3118, (2014).

258 Hecq, M. & Hecq, A. Oxygen induced preferred orientation of dc sputtered platinum. *J. Vac. Sci. Technol.* **18**, 219-222, (1981).

259 Kahsay, A. *et al.* Growth of epitaxial Pt thin films on (001) $SrTiO_3$ by rf magnetron sputtering. *Appl. Surf. Sci.* **306**, 23-26, (2014).

260 Son, J., Cagnon, J. & Stemmer, S. Strain relaxation in epitaxial Pt films on (001) $SrTiO_3$. *J. Appl. Phys.* **106**, 043525, (2009).

261 Kasai, M. & Dohi, H. Surface structure and electrochemical properties of platinum films grown on $SrTiO_3$(100) substrates. *Surf. Sci.* **666**, 14-22, (2017).

262 van der Pauw, L. J. A method of measuring the resistivity and Hall coefficient on lamellae of arbitrary shape. *Philips Techn. Rev.* **20**, 220-224, (1958).

263 Poker, D. B. & Klabunde, C. E. Temperature-Dependence of Electrical-Resistivity of Vanadium, Platinum, and Copper. *Phys. Rev. B* **26**, 7012-7014, (1982).

264 Berg, W. T. Low temperature heat capacity of platinum. *J. Phys. Chem. Solids* **30**, 69-72, (1969).

265 Uchida, M., Nomoto, T., Musashi, M., Arita, R. & Kawasaki, M. Superconductivity in Uniquely Strained RuO_2 Films. *Phys. Rev. Lett.* **125**, 147001, (2020).

266 Gao, R. *et al.* Interfacial Octahedral Rotation Mismatch Control of the Symmetry and Properties of $SrRuO_3$. *ACS Appl. Mater. Interfaces* **8**, 14871-14878, (2016).

267 Chu, F. *et al.* Microstructures and electrical properties of $SrRuO_3$ thin films on $LaAlO_3$ substrates. *J. Electron. Mater.* **25**, 1754-1759, (1996).

268 Gan, Q., Rao, R., Eom, C., Garrett, J. & Lee, M. Direct measurement of strain effects on magnetic and electrical properties of epitaxial $SrRuO_3$ thin films. *Appl. Phys. Lett.* **72**, 978-980, (1998).

269 Nair, H. P. *et al.* Synthesis science of $SrRuO_3$ and $CaRuO_3$ epitaxial films with high residual resistivity ratios. *APL Mater.* **6**, 046101, (2018).

270 Kikugawa, N. *et al.* Single-crystal growth of a perovskite ruthenate $SrRuO_3$ by the floating-zone method. *Cryst. Growth Des.* **15**, 5573-5577, (2015).

271 Meyer, S. *et al.* Temperature dependent spin transport properties of platinum inferred from spin Hall magnetoresistance measurements. *Appl. Phys. Lett.* **104**, 242411, (2014).

272 Vassen, R. & Jung, P. Interstitial migration of hydrogen and helium in platinum. *Phys. Rev. B* **37**, 2911-2917, (1988).

273 Zhu, L. J., Zhu, L. J., Sui, M. L., Ralph, D. C. & Buhrman, R. A. Variation of the giant intrinsic spin Hall conductivity of Pt with carrier lifetime. *Sci Adv* **5**, eaav8025, (2019).

274 Kockert, M., Mitdank, R., Zykov, A., Kowarik, S. & Fischer, S. F. Absolute Seebeck coefficient of thin platinum films. *J. Appl. Phys.* **126**, 105106, (2019).

275 Lu, Y. M. *et al.* Pt magnetic polarization on $Y_3Fe_5O_{12}$ and magnetotransport characteristics. *Phys. Rev. Lett.* **110**, 147207, (2013).

276 Zhou, H., Wochner, P., Schops, A. & Wagner, T. Investigation of platinum films grown on sapphire (0001) by molecular beam epitaxy. *J. Cryst. Growth* **234**, 561-568, (2002).

277 Watanabe, M., Morishita, M. & Ootuka, Y. Magnetoresistance of RuO_2-based resistance thermometers below 0.3 K. *Cryogenics* **41**, 143-148, (2001).

278 Jia, Q., Shi, Z., Jiao, K., Anderson, W. & Collins, F. Reactively sputtered RuO_2 thin film resistor with near zero temperature coefficient of resistance. *Thin Solid Films* **196**, 29-34, (1991).

279 L. Wang, C. C., K. Yang, E. Radue, M. T. Simons, I. Novikova, and R. A. Lukaszew. Bulk and surface plasmon polariton excitation in RuO_2 for low-loss plasmonic applications in NIR. *Optics Express* **20**, 8618, (2012).

280 Wang, F. *et al.* Electrode materials for aqueous asymmetric supercapacitors. *RSC Adv.* **3**, 13059-13084, (2013).

281 Stoerzinger, K. A., Qiao, L., Biegalski, M. D. & Shao-Horn, Y. Orientation-dependent oxygen evolution activities of rutile IrO_2 and RuO_2. *J. Phys. Chem. Lett.* **5**, 1636-1641, (2014).

282 Music, D., Kremer, O., Pernot, G. & Schneider, J. M. Designing low thermal conductivity of RuO_2 for thermoelectric applications. *Appl. Phys. Lett.* **106**, 063906, (2015).

283 Music, D. *et al.* Multifold Seebeck increase in RuO_2 films by quantum-guided lanthanide dilute alloying. *Appl. Phys. Lett.* **104**, 053903, (2014).

284 Berlijn, T. *et al.* Itinerant antiferromagnetism in RuO_2. *Phys. Rev. Lett.* **118**, 077201, (2017).

285 Green, M., Gross, M., Papa, L., Schnoes, K. & Brasen, D. Chemical vapor deposition of ruthenium and ruthenium dioxide films. *J. Electrochem. Soc.* **132**, 2677, (1985).

286 Maiwa, H., Ichinose, N. & Okazaki, K. Preparation and properties of Ru and RuO_2 thin film electrodes for ferroelectric thin films. *Jpn. J. Appl. Phys.* **33**, 5223, (1994).

287 Bernstein, S., Wong, T., Kisler, Y. & Tustison, R. Fatigue of ferroelectric $PbZr_xTi_yO_3$ capacitors with Ru and RuO_x electrodes. *J. Mater. Res.* **8**, 12-13, (1993).

288 Krusin-Elbaum, L., Wittmer, M. & Yee, D. Characterization of reactively sputtered ruthenium dioxide for very large scale integrated metallization. *Appl. Phys. Lett.* **50**, 1879-1881, (1987).

289 Kolawa, E. *et al.* Reactive sputtering of RuO_2 films. *Thin Solid Films* **173**, 217-224, (1989).

290 Gao, Y., Bai, G., Liang, Y., Dunham, G. & Chambers, S. Structure and surface morphology of highly conductive RuO_2 films grown on MgO by oxygen-plasma-assisted molecular beam epitaxy. *J. Mater. Res.* **12**, 1844-1849, (1997).

291 Kuo, D.-Y. *et al.* Chlorine evolution reaction electrocatalysis on RuO_2 (110) and IrO_2 (110) grown using molecular-beam epitaxy. *J. Chem. Phys.* **150**, 041726, (2019).

292 Kim, Y. J., Gao, Y. & Chambers, S. A. Core-level X-ray photoelectron spectra and X-ray photoelectron diffraction of RuO_2 (110) grown by molecular beam epitaxy on TiO_2 (110). *Appl. Surf. Sci.* **120**, 250-260, (1997).

293 Wang, Q., Gladfelter, W. L., Fennell Evans, D., Fan, Y. & Franciosi, A. Reactive-sputter deposition and structure of RuO_2 films on sapphire and strontium titanate. *J. Vac. Sci. Technol. A* **14**, 747-752, (1996).

294 Miao, G., Gupta, A., Xiao, G. & Anguelouch, A. Epitaxial growth of ruthenium dioxide films by chemical vapor deposition and its comparison with similarly grown chromium dioxide films. *Thin Solid Films* **478**, 159-163, (2005).

295 Jia, Q. *et al.* Heteroepitaxial growth of highly conductive metal oxide RuO_2 thin films by pulsed laser deposition. *Appl. Phys. Lett.* **67**, 1677-1679, (1995).

296 Jia, Q. *et al.* Epitaxial growth of highly conductive RuO_2 thin films on (100) Si. *Appl. Phys. Lett.* **68**, 1069-1071, (1996).

297 Jalan, B., Engel-Herbert, R., Cagnon, J. & Stemmer, S. Growth modes in metal-organic molecular beam epitaxy of TiO_2 on *r*-plane sapphire. *J. Vac. Sci. Technol. A* **27**, 230-233, (2009).

298 Scherrer, P. in *Kolloidchemie Ein Lehrbuch* 387-409 (Springer, 1912).

299 Taylor, C. J. *et al.* Does chemistry really matter in the chemical vapor deposition of titanium dioxide? Precursor and kinetic effects on the microstructure of polycrystalline films. *J. Am. Chem. Soc.* **121**, 5220-5229, (1999).

300 Wang, T., Prakash, A., Warner, E., Gladfelter, W. L. & Jalan, B. Molecular beam epitaxy growth of SnO_2 using a tin chemical precursor. *J. Vac. Sci. Technol. A* **33**, 020606, (2015).

301 A. Prakash, T. W., R. Choudhary, G. Haugstad, W. L. Gladfelter, and B. Jalan. Precursor selection in hybrid molecular beam epitaxy of alkaline-earth stannates. *J. Vac. Sci. Technol. A* **38**, 063410, ((2020)).

302 Ryden, W., Lawson, A. & Sartain, C. C. Electrical Transport Properties of IrO_2 and RuO_2. *Phys. Rev. B* **1**, 1494, (1970).